Thesis

Monitoring strain in rolling element bearings using fiber Bragg grating sensors

V. van den Bercken

Technical University Delft

TU Delft

Thesis

Monitoring strain in rolling element bearings using fiber Bragg grating sensors

by

V. van den Bercken

to obtain the degree of Master of Science
at the Delft University of Technology,
to be defended publicly on Thursday October 26, 2017 at 02:00 PM.

Student number:	4098862	
Project duration:	January 16, 2017 – October 16, 2017	
Thesis committee:	Dr. R. M. Groves	TU Delft, chair
	Dr. S. J. Garcia (Santiago)	TU Delft, external
	M. Sc. S. Van Eesbeek	SKF Group, supervisor
	M. Sc. H. van Genuchten	SKF Group

SKF

TU Delft

Summary

This report describes the research into possible causes of observed measurement differences in a rolling element bearing equipped with fiber Bragg grating (FBG) sensors. The rolling element bearing was equipped with multiple FBG sensors that were positioned in a groove on the outside of the outer ring of the bearing in close proximity to each other. Every sensor measured the strain in the outer ring. The strain distribution of a single rolling element passing the sensor, showed unexpected differences from sensor to sensor.

From the literature study, conducted prior to this research project, various causes were found that could possibly have an influence on the obtained strain readout of a FBG sensor. From the literature study a possible non-uniform strain over the sensors and bonding performance differences were selected to be investigated as possible causes of the measurement differences. This resulted in further evaluating the temperature behavior of the sensors, the peak detection method used by the interrogator, the Full Width at Half Maximum (FWHM) values of the sensors during the measurements and combinations of the previously mentioned cases.

Two test cases were proposed and executed. The first test focused on the thermal behavior of the sensors, no load was applied during this test. The second test phase assessed the sensor behavior when loaded. Both tests were performed with an interrogator capable of scanning the reflective spectra at a resolution 25 times higher compared to the interrogator used in the original measurements, performed with a SmartScan SBI interrogator. This gave better insights into what was happening between the sensor readouts (reflective spectra) and the obtained strains per sensor.

During the first test phase it was found that the induced strain on the sensors due to thermal expansion was uniform, the strain distribution over the sensors did not change with an increase in temperature. It was also found that there were differences in sensor response between the opposite sides of the bearing. Furthermore, it was found that in the operating temperature range of the bearing (20 to 100 degrees Celsius), sensors in the same group did not respond similar to temperature differences. This would translate in an offset in the strain distribution read out of the sensors, with differences up to 80 micro-strain between sensors. The second test phase showed that some sensors were subject to highly non-uniform strain during the measurements. This resulted in an increase in FWHM (up to 3.5 %) of the sensors in the loaded area. It was also shown that for a single load cases, the amount of strain measured by the sensors in the area near the strain peak, were affected by the peak detection method and FWHM of the sensors. It was shown that, an increase in FWHM resulted in different peak wavelengths from sensor to sensor when the SBI interrogator was used. This was simulated by reducing the amount of points in the peak detection algorithm of the SBI interrogator for single load cases. It was shown that sensors with a larger FWHM were less affected by the reduction of the number of points in the peak detection algorithm (by peak widening). Sensors closest to the connector showed a smaller FHWM compared to the sensors furthest away from the connector, hence the peak detection method will be different between sensors closest and furthest away form the connector. It is likely that this is due to the fact that the shape of the peak in the reflective spectra is not taken into account in the current peak detection method. In a single load case, this will lead to a strain offset (depending on the peak shape, positive, negative or no offset) from sensor to sensor, which is in particular visible in areas of low strain.

During the temperature test one group of sensors did not reach the targeted oven temperature, the results was a dispersed readout of the sensors. Because there was only one thermo-couple per group attached to the bearing during these measurements, it was impossible to create a temperature distribution estimate over the sensors. The bearing itself is also equipped with a single temperature FBG per sensor group, it is recommended to use at least two temperature FBGs per group in order to obtain a better estimate of the temperature over the sensors (other methods could be used as well). The loaded

test showed that there is a need of a peak detection method that can cope with the highly dynamic and non-uniform strain over the sensors. The peak detection used by the SmartScan SBI interrogator is not sufficient for this application. Additional research is needed to better evaluate sensor performance over the strain distribution of a rolling element, especially in the regions of low strain. For the creation of a more consistent peak detection method, a peak shape analysis could be performed on all obtained reflective spectra during this project, taking into account the positions of the sensors in the strain profile.

Preface

This graduate thesis report is written as part of a Master program in Aerospace Structures & Materials at the Aerospace-engineering faculty of the Technical University Delft. This report will be the concluding report of my Master program and (most likely) forms the end my time as a student at the Aerospace faculty. Writing this report would not have been possible with the help of a number of people, who I would like to thank.

First of all, I would like to thank Willemijn Remmerswaal and Charlotte Blankensteijn at Integrand Delft for bringing me into contact with SKF Group in Nieuwegein, that provided me with a challenging thesis subject. Furthermore, I would like to thank Eric van Genuchten and Stijn van Eesbeek at SKF for making this thesis project possible and for guiding me through the project, as well as their valuable expertise, input and feedback during the project. I would also like to thank Roger Groves at the TU Delft, for supervising the project and his valuable expertise, insights, look at the project from a different perspective and feedback during the project meetings. Next, I would like to thank Aydin Rajabzadeh and Andrei Anisimov for helping me getting familiar with the NI PXIe-4844 Interrogator and making the interrogator available for me during the experiments I conducted for this project. I would also like to thank Tom Vrancken for helping me with my second experiment, providing me with the needed equipment and his testing expertise.

Thanks to all my friends and family that supported me during my thesis and helped me relax during the times I was not busy with the project. A special thanks to my parents, for providing me the opportunity to come this far, for keeping me motivated and for supporting me during my time as a student. Last but not least, I would like to thank a very special person who I have met during the course of this project, my girlfriend, Rianne Laan. She supported me during the writing of this report and kept me motivated during the last few crucial months of the project.

V. van den Bercken
Nieuwegein, October 2017

Contents

List of Figures

List of Tables

Nomenclature

CCD	Charge-Coupled Device
CDM	Code Division Multiplexing
COTS	Commercial off-the-Shelf
CW	Clockwise
DBR	Distributed Bragg Reflector
DFB	Distributed Feedback
EMI	Electromagnetic Interference
DGD	Differential Group Delay
FBD	Free Body Diagram
FBG	Fiber Bragg Grating
FE	Finite Element
FFPI	Fiber Fabry-Pérot Interferometer
FPF	Fabry-Pérot Filter
FWHM	Full Width at Half Maximum
GF	Gauge Factor
LabVIEW	Laboratory Virtual Instrument Engineering Workbench
LPG	Long Period Grating
NI	National Instruments
PDL	Polarization Dependent Loss
PDM	Polarization Division Multiplexing
PZT	Piezoelectric Transducer
RMSE	Root Mean Squared Error
TDM	Time-Division Multiplexing
TSV	Tab-Separated Values
SDM	Spatial Division Multiplexing
SHM	Structural Health Monitoring
SKF	Svenska Kullagerfabriken (Swedish ball bearing factory)
SSE	Sum of Squared Errors
TFBG	Tilted Fiber Bragg Grating
VI	Virtual Instrument
WDM	Wavelength Division Multiplexing

α_Λ	Thermal Expansion Coefficient	[-]
α_n	Thermo-Optic Coefficient	[-]
α_{st}	Thermal Expansion Coefficient Steel	[-]
ϵ	Strain	[-]
Λ	Grating Period	[nm]
λ	Wavelength	[nm]
λ_B	Bragg Wavelength	[nm]
λ_{broad}	Broadband Source Input Wavelength	[nm]
$\lambda^{(m)}$	Mode Coupling Wavelength (m = 1,2,3 ..)	[nm]
ϕ	Radial Position Index	[rad]
μ	Mean	[-]
σ	Standard Deviation of the Gauss Curve	[-]
σ_s	Sensing Interferometer Path Length Difference	[m]

a	Arbitrary Constant	[-]
a_0	Amplitude	[-]

b	Arbitrary Constant	[-]
c	Arbitrary Constant	[-]
d	Distance	[m]
f	Frequency	[Hz]
i	General Index (1,2,3,..)	[-]
k	Spring Constant	[N/m]
k_e	Elasticity	[N/m^2]
$\bar{n}$	Mean Effective Refractive Index	[-]
$n_{cl,m}$	Effective Refractive Index Cladding	[-]
$\mathrm{n_{eff}}$	Effective Refractive Index Guided	[-]
p	Life Equation Exponent (L_{10})	[-]
p_e	Strain-Optic Coefficient	[-]
q	Force Element Applied by Rolling Element	[N]
w	Weighing Elements	[-]
x	Axis in Length Direction	[-]
x_B	Central Wavelength	[nm]
x_i	Central Wavelength of Element I	[nm]
C	Basic Dynamic Load Rating	[N]
D	Shear Force	[N]
D_n	Detector (n = 1,2,3 ..)	[-]
D_{or}	Diameter Outer Ring	[m]
E	Young's Modulus	[Pa]
F_r	Radial Force	[N]
FBG_n	FBG Number n	[-]
G_{nR}	Filter FBG (n = 1,2,3 ..)	[-]
G_{nS}	Measuring FBG (n = 1,2,3 ..)	[-]
I	Moment of Inertia	[m^4]
I_i	Light Intensity of Element i	[Wm^{-2}]
I_{fit}	Approximated Light Intensity	[Wm^{-2}]
$I(x)$	Light Intensity (Function of x)	[Wm^{-2}]
L	FBG Length	[m]
L_{10}	Bearing Lifetime according to L_{10} Method	[rev]
L_r	Characteristic Length of Rail	[-]
L_s	Fabry-Pérot Cavity Length	[m]
M	Moment	[Nm]
N	Number of Input Elements	[-]
O	Origin	[-]
P	Equivalent Dynamic Bearing Load	[N]
Q	Load Applied by Rolling Element	[N]
R	Electrical Resistance	[Ω]
R_R	Remainder	[-]
T	Temperature	[K]
W	Displacement	[m]
X	Axis in Radial Direction	[-]
Z	Axis in Length Direction	[-]

1 Introduction

The company SKF Group was founded in Gothenburg, Sweden in 1907 and manufactures and supplies bearings, seals, lubricants and lubrication systems, maintenance products, mechatronics products, power transmission products and condition monitoring systems. SKF stands for Svenska Kullagerfabriken which means Swedish ball bearing factory. The company is currently in the process of developing a load sensing bearing, using optical sensing methods. A bearing is an element in a machine that constrains relative motion to only the desired motion, and aims to do this with the least amount of friction. There is a generous amount of bearing types available on the market today, but this study will restrict itself to a single row ball bearing. However, the measurement methods presented here could potentially be applied to other types of bearings as well. The life expectancy and maintenance intervals of bearings are currently obtained empirically, this usually results in early maintenance or unexpected failure of the bearing. By actively monitoring the bearing's health, maintenance needs can be predicted, reducing wear of the bearing due to ineffective maintenance, increasing the overall lifetime and increasing the accuracy of the life expectancy prediction of the bearing, by using intermediate inputs from the sensors. This is done by measuring the strain in the outer ring of the bearing. The strain is then related to the load in the bearing, which is an important input parameter for the life expectancy prediction. Even more importantly, locally measuring the strain in the bearing could help to improve the running conditions of the bearing, making it possible to produce even more efficient bearings in the future.

A novel way to monitor bearings, is by using Fiber Bragg Grating (FBG) sensors. These sensors will measure the strain in the outer ring of the bearing. FBG sensors are highly suitable for this application due their capability of local strain measurements, relatively small size, high sensitivity, inertness to electric or magnetic interference and multiplexing capability [77]. However, in the current setup the measured strains show differences from sensor to sensor. In order to assess the observed differences in the measurements, additional testing of the bearing will be done. These tests will focus on phenomena that influence the reflective spectra of the FBGs and how the reflective spectra is translated to strain values. This research project was initiated by the company SKF. The company would like to obtain a better understanding of the obtained results from FBG sensors and, possibly, a solution on how to eliminate the observed differences. This forms the research objective for this project.

The objective of the master thesis is to give recommendations to SKF on how to explain the fluctuations observed in the reflective spectra of the FBG sensors integrated in the rolling element bearing by performing a diagnostic gap analysis in which simplified/controlled FBG measurements will be compared to the results obtained by the existing test setup, which consist of an actual rolling element bearing equipped with multiple FBG sensors. From this research objective the following research question was formulated for the master thesis.

"What causes the observed differences in the strain distribution from sensor to sensor in the rolling element bearing equipped with Fiber Bragg Gratings sensors?"

Prior to writing this thesis, a literature study was conducted that reviewed the most influential parameters that induce measurement differences in FBGs. From this study a possible non-uniform strain over

the sensors and bonding performance differences were selected to be investigated as possible causes of the measurement differences observed by SKF.

The structure of this report is as follows: Chapter 2 will start with the most relevant findings of the literature study performed prior to this project, it will describe the general working principles of a rolling element bearing and key elements of the FBG based measurement setups. Chapter 3 will give the problem statement, Chapter 4 describes the problem analysis, including the possible test objects and test methods, Chapter 5 will give the results and Chapter 6 will conclude with the discussion, including the recommendations and suggestions for future research.

2

Literature Review

This chapter will give an overview of the different bearing types available and giving a better understanding of what the sensors will be measuring. Section 2.1 starts with a general overview of the different bearings and Section 2.2 will focus on the rolling element bearings, the type of bearing that has been used in order to obtain the FBG measurements of interest for this project. A bearing is a machine element that will constrain a moving element in the desired direction only. This can be a linear motion or a rotary motion, performed at a low speed up to very high speeds. Next this chapter will elaborate on the different types of FBGs and the components needed in order to measure with FBG sensors in Section 2.3.

2.1. Bearing Type Overview

As stated in the introduction of this chapter, a wide variety of bearings are available. Choosing the right one depends on the type of motion, the frequency of the motion, the load that has to be carried, the required lifetime, the required precision, etc. This section will not discuss on how to select the right bearing for the application, instead it will briefly discuss the available bearings types. In general there are two types of bearings, contact and non-contact bearings. Contact bearings include the sliding, rolling and flexural bearings. These bearings have a mechanical contact between stationary and moving parts, meaning high stiffness, hence are able to carry higher loads. A downside however, because of the mechanical contact, wear or fatigue can limit their life. Non-contact bearings are less prone to wear or fatigue, assuming the bearing is properly maintained and used within its specifications. This is because no mechanical contact is made between elements inside the bearing, this is for example achieved by magnetic forces, hence a Magnetic bearing, or fluids. Figure 2.1 gives the cost versus performance of different types of bearings. As can be seen the sliding contact bearings are relatively low cost and low performance, while the non-contact bearings are fairly high cost and high performance and are less susceptible to wear or fatigue damage. In the middle there is the rolling element bearing type, this type of bearing is susceptible to wear and fatigue damage and their relatively high cost justifies the extra monitoring costs in order to increase their service lifetimes. The list below gives a list of common types of bearings. The next section will give more information on the rolling element bearing, the type of bearing that will be monitored by FBG sensors in this project.

- Sliding Contact
- Rolling Element
- Hydrodynamic
- Hydrostatic
- Aerostatic
- Magnetic
- Flexural

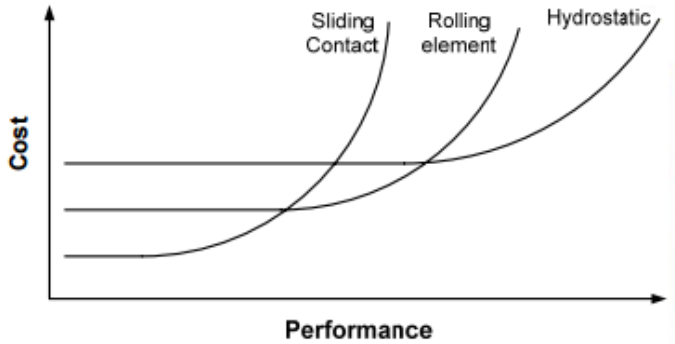

Figure 2.1: Cost vs. Performance for different types of bearings [72]

2.2. Rolling Element Bearings

Rolling element bearings use ball or cylinder shaped rolling elements in order to generate a low friction connection between the stationary outer ring and moving inner ring of the bearing (or vica versa). The contact surfaces between the outer ring and rolling elements and the inner ring and rolling elements are called raceways. Figure 2.2 shows a deep groove (Conrad) ball bearing, the most common form of ball bearings [45]. This type of bearing is intended for radial load transfer (forces that act perpendicular to the supporting axis), but can also take limited axial loads in all directions. Figure 2.3 shows a thruster ball bearing, this type of bearing is specifically designed to carry axial loads.

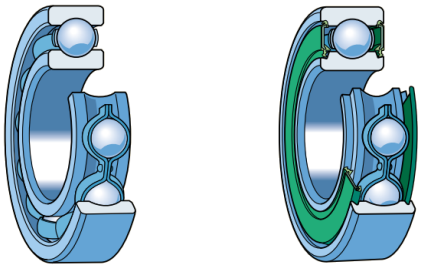

Figure 2.2: Deep Groove Ball Bearing [71]

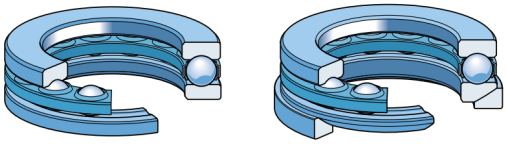

Figure 2.3: Thruster Ball Bearing [71]

There are different setups of bearings available that are capable of carrying a combination of axial and radial loads, as well as moment loads and that are able to cope with axis misalignments; however this study focuses on single row rolling element bearings that support a rotary motion and are supposed to be subjected to a radial load only. The rolling elements in the bearing are separated by a cage, the cage keeps the rolling elements (evenly) spaced inside the bearing, making sure the inner ring remains concentric with the outer ring and keeping the rolling elements from rubbing against each other. Different cages are available for different applications, for instance for high speeds or high accuracy. The bearing on the right in Figure 2.2 is equipped with a shield(green), the shield makes sure lubricants stay in and contaminants stay out of the bearing. Again different shields and seals are available for bearings, as well as different lubrication methods, selection of the right shield or seal is again depended on the application.
The causes of failure for rolling element bearings as described in [45] are listed below:

- Fatigue flaking or cracking of the raceways or rolling elements. Micro-structure discontinuities, like non-metallic inclusions in the steel, or grinding marks are the main sources of crack nucleation. Fatigue flaking is the main fracture mode for bearings that have excellent lubrication and shielding against foreign particles. This failure mode is usually observed after a long operation time.
- Formation of dimples and hollows in the raceways or rolling elements as a consequence of local plastic deformations due to excess vibrational loads, impact loads or considerable dead loads. This failure mode will result in reduced efficiency, higher noise levels and higher vibrations.

- Abrasion of the bearing due to shield/seal damage, this failure mode usually occurs in highly contaminated environments like construction sites and engines.
- Cage fracture due to the action of centrifugal forces and load cycles of the rolling elements on the cage. This failure mode usually occurs in high-speed bearings and results in efficiency loss and increased operation noise rather than complete failure.
- Raceway fracture due to raceway warping or impact overloads. This failure mode is usually the result of improper assembly and operation.

The basic design life of rolling element bearings is based on experimental data and several theories. The design life is usually expressed in millions of revolutions by the L_{10} method. At L_{10} lifetime, 90% of the bearings will not have developed fatigue flaking or cracking of the raceway. The L_{10} is given by the expression shown in Equation 2.1.

$$L_{10} = \left(\frac{C}{P}\right)^{p} \tag{2.1}$$

With C the basic dynamic load rating, P the equivalent dynamic bearing load and p the exponent for the life equation. The exponent for the life equation is usually 3 for ball bearings and 10/3 for roller bearings [70]. Sometimes the lifetime is also given in operating hours at a given speed. Several studies show that there is still a need to improve service life predictions of rolling element bearings, as described in [51, 55, 64]. Moreover, practical experience shows that bearing failure due to fatigue of the raceways or rolling elements, at which the L_{10} method is based, is rare. Most failures occur due to abrasive wear, corrosion, incorrect mounting or incorrect usage [71]. By actively monitoring the health of the bearing one could possibly prevent failures due to ineffective maintenance, incorrect mounting or usage and other factors. Moreover, one could use the obtained health data in order to give a better prediction of the remaining service life of the bearing.

In order to obtain a better understanding of what will be measured by the sensors, a short description is given here about bearing loads. In literature a lot of models are described regarding bearing loads. For example the study performed in [63], presents a model which is able to describe rolling element bearing loads both for perfectly intact bearings and rolling element bearings with defects. The model presented here is based on work presented in [67, 68]. Knowing there are models developed and available, is for now sufficient in order to continue with this research project. From a simpler point of view, when a bearing is radially loaded, the load distribution over ω is usually as shown in Figure 2.4.

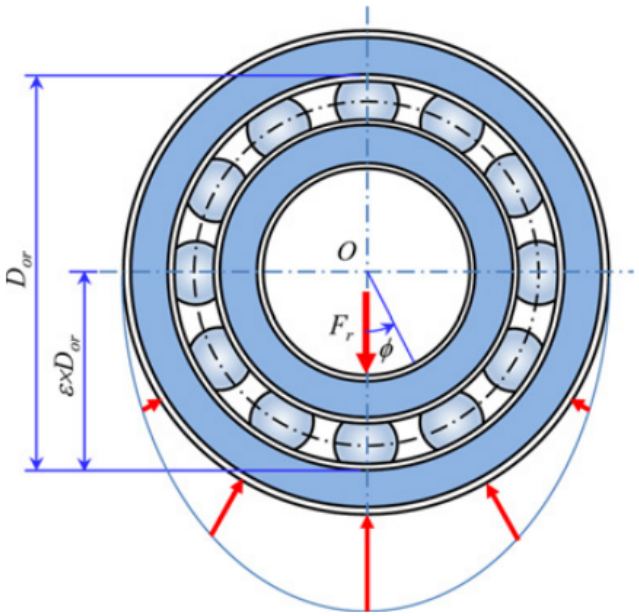

Figure 2.4: Typical load distribution of a rolling element bearing. Where D_{or} is the diameter of the outer raceway, ϵ = 0.5 and F_r the applied radial load [25]

When the outer ring is stationary and the inner ring is rotating, a sensor placed on the outer ring of the rolling element bearing will over time measure the rolling elements passing. The expected measured strain by the sensor could be approximated by a rolling element passing over a continuous elastically supported rail. This simplified model is proposed in [18] and based on the model developed by Zimmerman [82], a schematic overview of the problem is given in Figure 2.5. Here $w(x)$ is the displacement function of the rail and as can be seen it is only dependent in the lengthwise direction, x-direction.

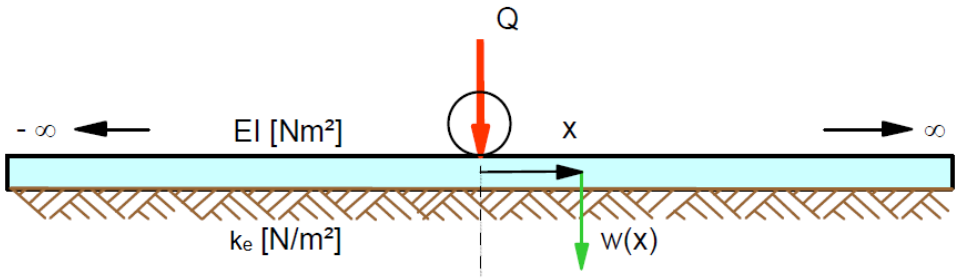

Figure 2.5: Rolling element over continuous elastically supported rail, with Q the load applied by the rolling element, EI the stiffness of the rail, k_e the elasticity of the support and w(x) the displacement as a function of x [18]

The free body diagram (FBD) of a single element is given in Figure 2.6, from this the equilibrium equations can be obtained, as shown in Equation 2.2 and 2.3. The reference further gives the constitutive equation and boundary conditions and solves the differential equation, these steps are not shown here as only the shape of the deflection is of interest. Therefore, only the obtained shape functions are shown in the expressions shown in Equation 2.4 and 2.5, giving the bending moment and deflection shape lines respectively, here L_r is the characteristic length of the rail in meters, given by Equation 2.6.

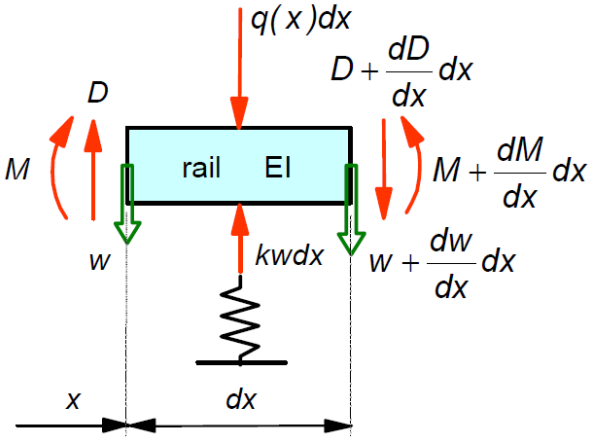

Figure 2.6: Free Body Diagram of a single element, with M the applied moment, D the applied shear force (Dwarskracht in Dutch), q the force element applied by the rolling element, w the displacement and k the spring coefficient [18]

$$qdx + \frac{dD}{dx}dx = kwdx \tag{2.2}$$

$$Ddx = \frac{dM}{dx}dx \tag{2.3}$$

$$\eta(x) = e^{-x/L}\left[\cos\frac{x}{L} + \sin\frac{x}{L}\right] \qquad x \geqslant 0 \tag{2.4}$$

$$\mu(x) = e^{-x/L}\left[\cos\frac{x}{L} - \sin\frac{x}{L}\right] \qquad x \geqslant 0 \tag{2.5}$$

$$L_r = \sqrt[4]{\frac{4EI}{k}} \tag{2.6}$$

A plot of the shape functions of the relative displacement and the relative bending moment are given in Figure 2.7. From the FBG sensor data, relative displacements will be obtained, further discussion about strains obtained form the FBG sensors is given in Section 3.2. The negative section of the shapes given in Figure 2.7 are obtained due to symmetry. This is only the case if there is negligible friction between the rolling element and the rail and when there is no slipping of the rolling element over the rail. This may not be the case in a rolling element bearing, when slipping occurs or excessive friction is present, the side-lobes of the peak are no longer symmetrical.

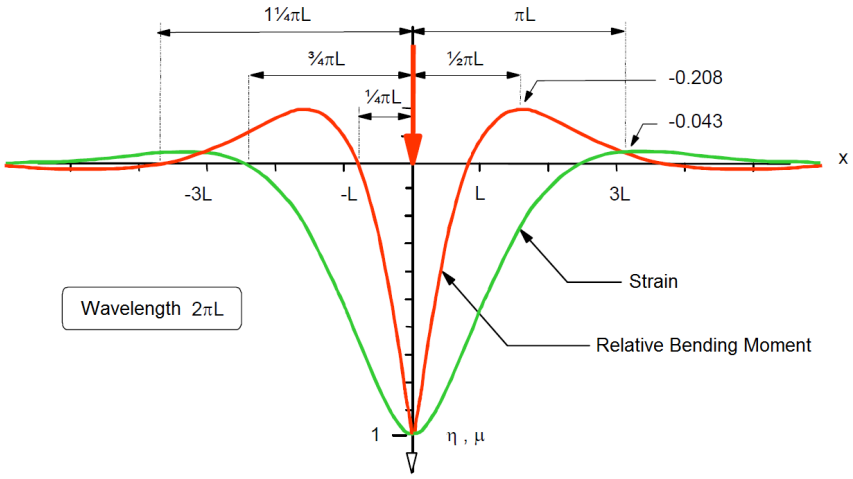

Figure 2.7: Deflection and bending moment due to the rolling element [18]

2.3. FBG Based Measurement Setups

In 1978, Ken O. Hill found the effect of photo sensitivity for germanium doped fibers. It was shown that exposure of the germanium doped fibers to ultraviolet light induces a permanent change to the refractive index of the fiber [22]. Next, in the same year, a very narrowband Bragg grating filter was formed over 1-m of fiber [32]. This led to the start of numerous research projects into the nonlinear properties of Germanium doped silica fibers. These studies evolved the principle to the current state, where FBGs are used to measure strain and many other parameters. Figure 2.8 shows the working principle of the FBG, the Bragg wavelength is the wavelength peak that is reflected by the FBG. The Bragg wavelength (λ_B) is given by Equation 2.7. Here n_{eff} is the effective refractive index of the fiber, Λ_B is the period of the gratings and I(x) is the light intensity as a function of x.

$$\lambda_B = 2n_{eff}\Lambda \tag{2.7}$$

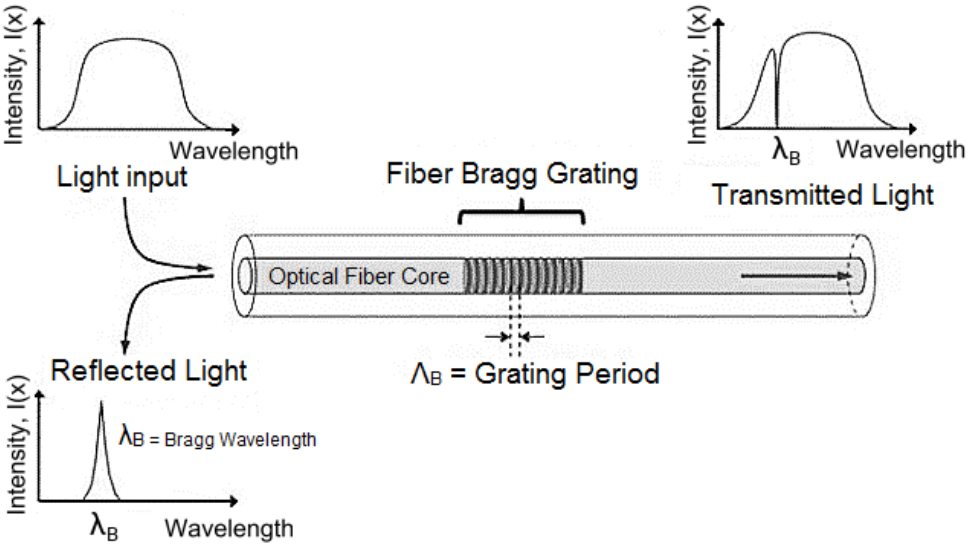

Figure 2.8: FBG Working principle [15]

As the FBG is strained, the period of the gratings will change and so will the reflective Bragg wavelength. When one is able to measure the shift in reflective wavelength, one can relate this to the strain in the FBG. However, when only the stress in the host material is of interest, one has to account for temperature changes. The temperature changes will induce strains into the host material and fiber, independently of the applied stress, by thermal expansion/contraction. The relation between the shift in Bragg wavelength and temperature and strain is given by the expression shown in Equation 2.8.

$$\frac{\Delta\lambda_{\mathrm{B}}}{\lambda_{\mathrm{B}}} = (1 - p_e)\epsilon + (\alpha_\Lambda + \alpha_n)\Delta T \tag{2.8}$$

Here $\Delta\lambda_{\mathrm{B}}$ is the wavelength shift, p_e is the strain-optic coefficient, describing the change in refractive index due to strain, α_Λ the thermal expansion coefficient, which describes the expansion/contraction of the grating due to temperature and α_n the thermo-optic coefficient, which describes the change in refractive index due to temperature. As can be seen, normally a FBG would respond to both temperature and strain, which is undesiriable for this particular case, as the main interest is the applied load independently of the temperature. A typical strain sensitivity for a FBG, $\frac{\Delta\lambda_{\mathrm{B}}}{\Delta\epsilon}$, is 1.2 pm/$\mu\epsilon$ and a typical temperature sensitivity, $\frac{\Delta\lambda_{\mathrm{B}}}{\Delta T}$, is 13 pm/°C (also dependent on the type of fiber used) [62]. Literature mentions several solutions for this problem. The most common solution is the use of a second FBG that is subjected to the same temperatures as the first FBG, but located in a strain free location [34]. This is not always possible, so sometimes it is necessary to encapsulate the secondary FBG sensor in a suitable capillary [53], as can be seen in Figure 2.9. Numerous other methods are mentioned in literature in order to overcome the temperate influence on the strain measurement by the FBG sensors. These methods are outside the scope of this review.

In the case for the rolling element bearing, the most interesting is the strain differences between minimum strain and maximum strain, this cycle occurs by a single rolling element passing the sensor. From this strain difference, the applied load could be calculated and possible fluctuations in the strain could tell something about the running conditions of the bearing. Because the bearing is running at a considerable speed and the rolling elements are small, the period is short (approximately 0.05 s), therefore the temperature change during the load cycle is neglected. The sensors are attached to the rolling element bearing in a groove on the outside of the outer ring. This way the performance of the bearing is least affected and the bearing is interchangeable with non sensorized bearings of the same type.

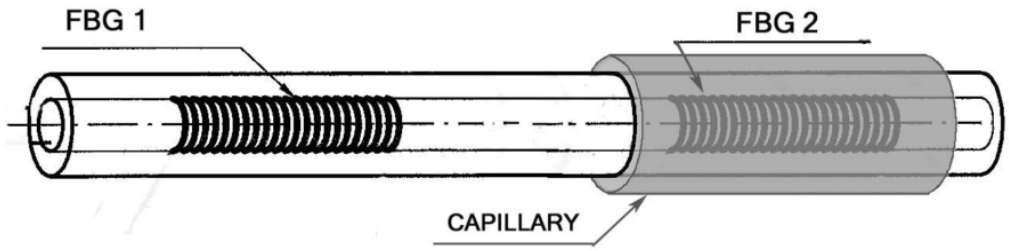

Figure 2.9: FBG 1 is subjected to strain and temperature changes, FBG 2 is only subjected to temperature changes [53]

This section will further elaborate on the different elements in the FBG measurement setup as shown in Figure 2.10. The figure gives a general overview of the elements present in a typical FBG measurement setup, it is essential for answering the research question to understand the working principles, to have an overview of the available techniques in FBG measurement setups and to have a good understanding of the benefits and drawbacks of certain techniques. This section will focus on the theoretical part of the mentioned elements. This section will start with the FBG sensors, explaining the different grating structures that are mentioned in literature in Subsection 2.3.1, next Subsection 2.3.2 describes common interrogator designs, including interrogator elements like sources, detectors, multiplexing techniques and peak detection methods and will end with a list of common commercial off-the-shelf interrogators, lastly Subsection 2.3.3 will give examples of FBG applications.

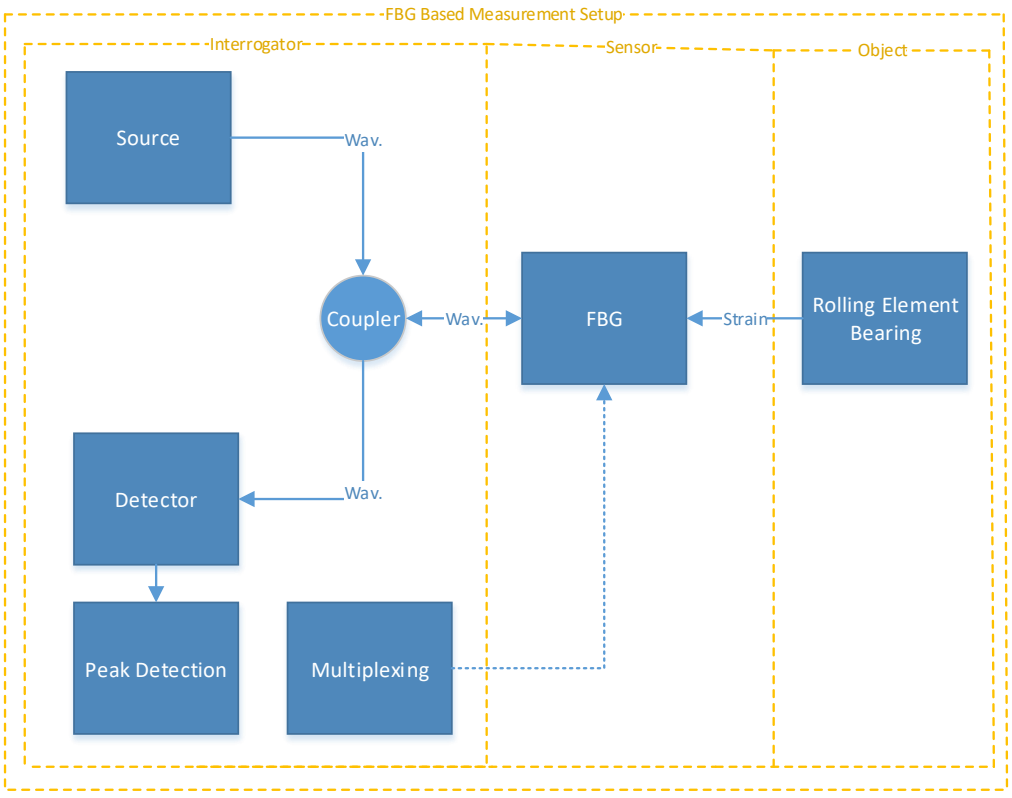

Figure 2.10: FBG measurement elements overview

2.3.1. Grating Structures

Several different gratings structures are mentioned in literature. The standard FBG uses a gratings with constant period written perpendicular to the fiber axis (uniform gratings). This makes the FBG symmetric radially and axially. The FBG makes use of the change in wavelength in order to measure

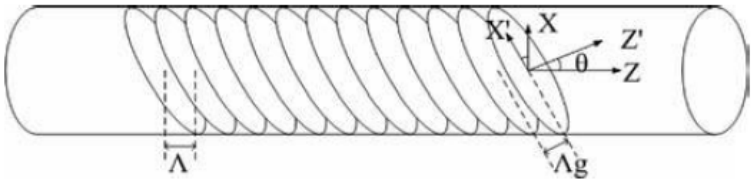

Figure 2.11: Schematic overview of a titlted FBG, with Λ_g the period of the tilted grating planes, ZX the axis system of the fiber and Z'X' the rotated axis system over θ of the tilted gratings. [65]

the strain or temperature, therefore this type of FBG is not affected by losses in the cables, connectors or any other sources of losses (to a certain extent). The tilted, chirped and apodized and long period grating structures are shortly described below.

In a tilted FBG (TFBG) the gratings are not perpendicular to the fiber cross-section, as in a standard FBG, instead they have a certain angle with respect to the length of the fiber (optical axis or fiber axis), see Figure 2.11. Due to the tilt angle of the gratings, part of the forward propagating core mode light will be coupled into the counter-propagating cladding mode, for finite fiber cladding geometry. If the cladding diameter is assumed infinite, the propagating core mode will also be coupled into radiation modes, as described in [16]. The largest advantage of a TFBG over a normal FBG is its ability to discriminate between strain and temperature changes. This can be done by comparing the core mode resonance and the cladding mode resonance so the effect of temperature can be canceled out. However, the demodulation of the cladding modes and core mode in the transmission spectrum is difficult [65].

The gratings in a Chirped FBG do not have a constant period. For instance, the period of the gratings may vary linearly, changing the refractive index over the FBG (See Figure 2.12). Due to the change in the grating period, the reflective wavelengths will also change, broadening the total reflective spectrum of the FBG. Next to a linearly changing grating period, many other chirped gratings exist, symmetric, asymmetric, non-linear, etc., each having its own practicalities. The type that is interesting for measuring strain is the linearly changing grating period, making it possible to distinguish local strain on the sensor. The shape of the broadened reflective spectra corresponds to the position in the sensor, this is the largest advantage of the chirped FBG over a normal FBG [78].

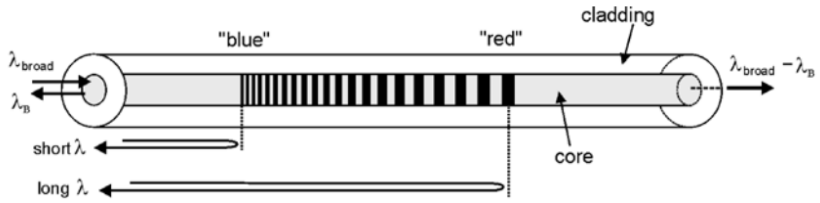

Figure 2.12: Schematic overview of a chirped FBG [61]

An Apodized FBG will have reduced side lobes in the reflective spectra, as shown in [21, 56]. This is achieved by gradually increasing the coupling coefficient at the start of the FBG and generally decreasing the coupling coefficient near the end of the FBG, while making sure the average refractive index of the gratings remains constant. Figure 2.13 gives the refractive index of an uniform FBG and Figure 2.14 gives the refractive index of an apodized FBG. The refractive index can be changed by different profiles, for example the sine function shown in the figure. Figure 2.15 gives the reflective spectra of apodized FBGs with different apodization profiles. The profiles are described in [2], most important here is the comparison to a uniform grating. As can be seen, the sidelobes of an apodized FBG are very small compared to an uniform FBG. Apodization can be applied to normal FBGs as well as to FBG with a special grating structure. As described in [19], using apodization may be beneficial for multiplexing. Because, the reduced side lobes will have little effect on the adjacent sensors, making it possible to use smaller channel spacing.

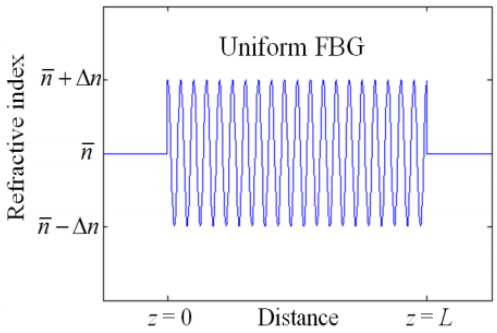

Figure 2.13: Refrective index change along uniform FBG [2]

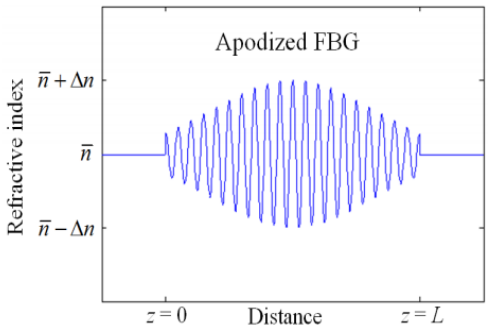

Figure 2.14: Refrective index change along apodized FBG [2]

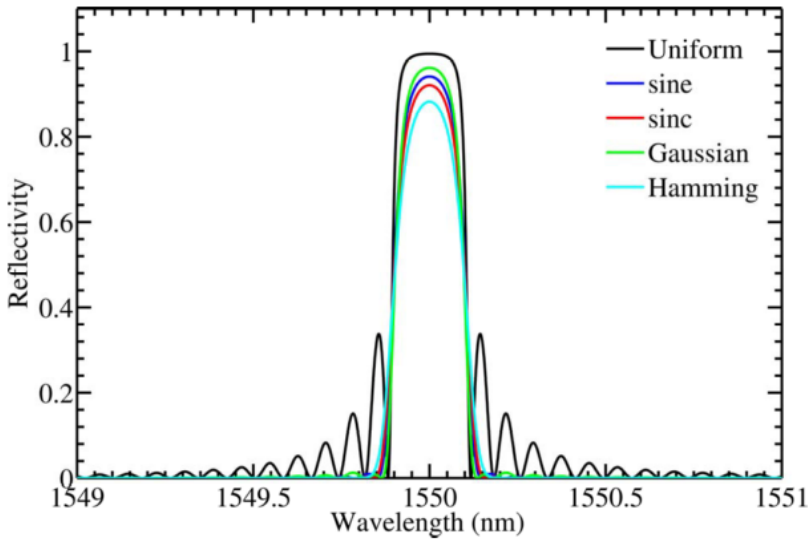

Figure 2.15: Reflective spectra of apodized FBGs [2]

A Long Period Grating (LPG) does not rely on its reflective spectrum, but instead on its transmission spectrum. See Figure 2.16 for a schematic representation of the working principle of an LPG. The light that propagates through the fiber is deflected by the grating into cladding modes. These modes attenuate rapidly while propagating through the fiber due to bends in the fiber and absorption due to the cladding. This will result in no reflection and a loss of certain wavelengths in the transmission spectrum. The cladding modes will be influenced by the grating properties, but more importantly, also by strain, temperature, bend radius and to the refractive index of the medium surrounding the fiber [5]. This property can be exploited in order to measure the strain in the sensor. A long-period grating with periodicity Λ, will be subject to mode coupling at wavelength $\lambda^{(m)}$ through the relation given in Equation 2.9. With n_{eff} the effective refractive index of the core and $n_{cl,m}$ the effective reflective index of the cladding.

$$\lambda^{(m)} = (n_{eff} - n_{cl,m})\Lambda \tag{2.9}$$

The sensitivity of a long-period grating to axial strain ϵ can be obtained by expanding Equation 2.9 and rearranging to yield the expression in Equation 2.10. This expression contains two components on the right hand side, the first one being the material contribution and the second the wave-guide contribution. The two contributions can have either polarity, depending on the grating period and the order of the cladding mode. It is also possible that both contributions are of the same magnitude but opposite polarity, this would be a strain insensitive grating which could be used as a pure temperature sensor [5, 29]. Long period gratings can achieve higher strain sensitivity when choosing a LPG period

less than 100 μm. Also, applying transverse loads on a LPG has shown increased strain sensitivity compared to normal FBGs [50, 80].

$$\frac{d\lambda}{d\epsilon} = \frac{d\lambda}{d(\delta \mathrm{n}_{\mathrm{eff}})}\left(\frac{d\mathrm{n}_{\mathrm{eff}}}{d\epsilon} - \frac{dn_{cl}}{d\epsilon}\right) + \Lambda\frac{d\lambda}{d\Lambda} \tag{2.10}$$

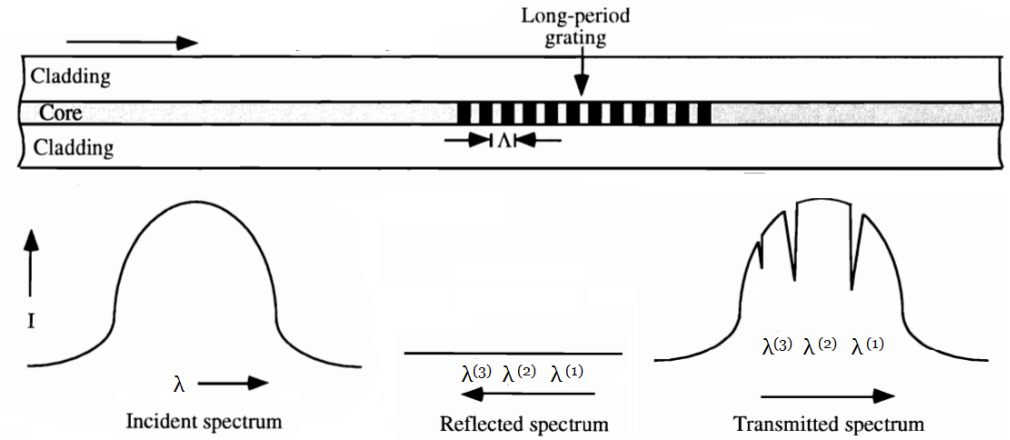

Figure 2.16: Schematic overview of a chirped LPG [4]

2.3.2. Interrogator Designs

Interrogator units provide the light source (in most cases) and measure the reflective or transmitted spectrum of the FBG. Thus one can say, the interrogator unit is an essential part in the measurement setup in order to measure the wavelength shifts accurately. The most commonly used wavelengths in FBG sensors are wavelengths ranging from 1500 nm to 1600 nm. Important parameters of an interrogator unit for FBG sensors are the wavelength range, spacing/resolution and scan frequency. The wavelength range is the range the interrogator is able to scan, an interrogator with a large wavelength range is therefore beneficial for multiplexing. However, a large wavelength range usually comes with reduced wavelength spacing/resolution. In the case of the rolling element bearing, the strain is constantly varying over time, as the rolling element bearing is rotating. This makes the scan frequency an important parameter as well. There are two major design parameters in an interrogator unit namely, the source and the detector. This subsection will discuss the different sources available in interrogators and the possible detection methods for obtaining the transmitted or reflected spectra of the FBGs. It will also describe common multiplexing and peak detection techniques used for FBG measurements. This subsection will end with a list of interrogators, together with their specifications, that are currently available off-the-shelf, obtaining a better overview of the possibilities and current performance of interrogators.

Sources

There are different interrogator sources mentioned in literature, two main groups are mentioned, namely the continuous, or broadband, sources and sweeping sources. A commonly used sweeping source is the wavelength-swept laser, these lasers can have different working principles. Working principles mentioned in literature are the wavelength-swept thermo-optic laser [43], Fourier/Active domain mode-locked wavelength-swept laser [40, 42] and the wavelength-swept laser with a polygon-scanner-based wavelength filter [37]. The most important parameter of a swept source is the scanning speed and resolution. The Fourier domain mode-locked wavelength-swept laser has been reported with a scanning speed over 30 kHz, together with a possible solution to improve it to over 100 kHz and a spectral resolution of 13 pm [30]. When a swept source is used, simple photo-detectors could be sufficient in order to obtain the wavelength intensities, by linking the measured intensities to the (laser) sweep timing. Another option is to use a continuous or broadband light source, these type of sources are do not require any elaboration in this study. Using a broadband source however, means the detector has to filter the light somehow in order to detect the different wavelengths.

Detectors
Also for the detector working principle, different techniques are mentioned in literature. As already stated in the previous section regarding sources, when using a swept source, having photo-detectors is suffcient in order to capture the Bragg wavelengths. When using a broadband light source, the simplest way to measure the reflective wavelength of a FBG is to make use of a linear wavelength-dependent optical filter (Edge Filter). This method was one of the first proposed for wavelength change interrogation systems of FBGs [57]. The filter is placed in front of the detector and is linearly dependent on the wavelength, as is shown in Figure 2.17. In the figure, the dashed line is the Bragg wavelength of the FBG. When the wavelength shifts, the interrogator will detect a change in transmittance intensity level, which it can correlate to a change in Bragg wavelength. The filter can be adjusted to have different slopes, changing the measurement range and sensitivity of the interrogator. The largest advantage of using this technique is the simplicity of the design. This type of interrogator is however susceptible to source intensity fluctuations or losses in cables and hence does not make use of the key advantage of the FBG namely, the measurand is stored in the reflective wavelength and not in the intensity. In order to obtain an accurate transmittance intensity level, the interrogator often splits the light into two fibers, one containing a filtered detector and the other one an unfiltered detector. This will cancel out any source intensity fluctuations or losses in the cables. Other filter based interrogators mentioned in literature are wavelength division multiplexing couplers [12, 57] and matched grating filters [28]. Above mentioned interrogators are also called passive detection scheme interrogators, as they do not use any electrical, mechanical or optical active components.

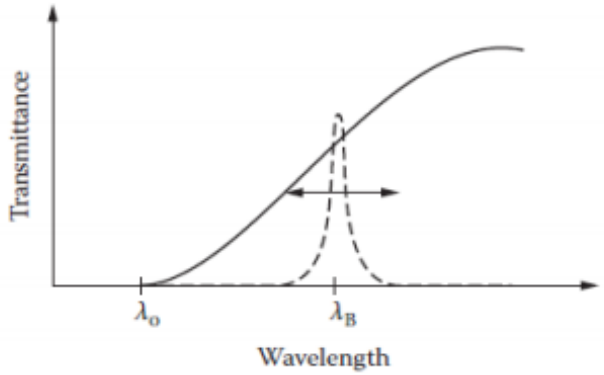

Figure 2.17: Transmittance of the linearly wavelength-dependent optical filter interrogator [79]

Active interrogator schemes are more complex compared to passive interrogators however, active schemes do show better resolution. Again several active techniques are mentioned in literature, but only the most relevant are shortly discussed here. The first one being the Bragg grating scanning filter [28], which is shown in parallel in Figure 2.18. It uses piezoelectric transducers (PZT) in order to match the matching filter FBGs (G_{1R} to G_{4R}) to the measuring FBGs (G_{1S} to G_{4S}). Once both FBGs are matched, light will pass downstream to the detectors (D_1 to D_4). Because the wavelength shifts of the FBGs are limited, there is a matching FBG needed in the interrogator for every sensor FBG attached to it together with a coupler and photodetector. This type of interrogator is also reported configured in series [6], in this case the filter FBGs each have their own PZT which will change the wavelength at a unique frequency, this way only a single coupler and photodetector are needed in the interrogator.

Another common interrogation method is based on a tuneable band-pass filter. Tuneable Fabry-Pérot Filter (FPF) interrogators [33] are frequently mentioned in literature. The working principle of this interrogator relies on a Fabry-Pérot cavity, whereby the mirror spacing is controlled by a PZT, somewhat similar to the Bragg grating scanning filter shown in Figure 2.18. The change in mirror distance will result in a change of the filter passband. When only a single FBG is attached to the interrogator, the filter could track the Bragg Wavelength shifts of the FBG. When multiple FBGs are used, all having their own Bragg Wavelengths, the interrogator could scan through the wavelength range in order to assess all FBGs.

Next to filter based interrogators there is also a parallel detection of the total wavelength mentioned.

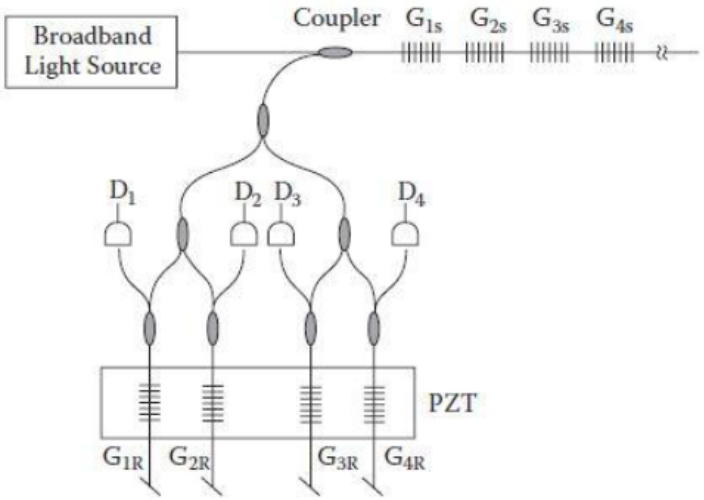

Figure 2.18: Matched FBG Pair Interrogator in parallel [28]

This method is based on a charge-coupled device (CCD) detector, in some studies this type of interrogator is also called a passive interrogator. The light is diffracted by a diffraction grating over a series of detector pixels, as is schematically shown in Figure 2.19. The resolution of this method depends on the amount of pixels in the CCD array and the peak detection algorithm. Multiplexing is already possible with this method, as long as the wavelength range of the CCD is sufficient. One could also use multiple fibers and a 2-dimensional CCD array, making it possible to further increase the number of sensors that could be interrogated. CCD based interrogators evolved to high performance interrogators however, the prices of components tend to be higher compared to filtering interrogator components.

The last detection method worth mentioning is the interferometry class. This type of interrogator uses the wavelength shift of the sensor and a Mach-Zehnder or Michelson interferometer in order to monitor the phase change of the signal. A common interrogator type based on this is the Fiber Fourier Transform Spectrometer Interrogator [13]. The cited interrogation technique makes use of the Michelson interferometer. Another Fiber Fourier Transform Spectrometer, based on the Mach-Zehnder interferomter, was reported more recently and is described in [44]. The resolution of this method can be extremely high, as well as the scanning frequency. Nonetheless, a recent study showed that the CCD based interrogator has evolved to a performance level equivalent to that of an interferometry based interrogator [11].

Multiplexing Techniques

Next to the different sources and detectors, several techniques for multiplexing are mentioned in literature. Multiplexing is usually referring to the ability of using multiple sensors on the same fiber, but sometimes also to the ability of using a single interrogator to scan through multiple FBG sensors over multiple channels. Common multiplexing techniques mentioned in literature are: Time-Division Multiplexing (TDM), Wavelength Division Multiplexing (WDM), Polarization Division Multiplexing (PDM) and Code Division Multiplexing (CDM). These techniques could also be combined in order to improve performance.

The TDM technique uses low reflective FBGs with the same Bragg wavelength. The low reflectivity is needed in order to let part of the signal pass (lower intensity rather than blocking the signal completely) for the FBGs downstream. The interrogator will differentiate between the FBGs by comparing the time delay of the return signal to a reference. This way the FBG interrogation is relatively low cost, very robust and can be performed at high sampling speeds. The major drawback of the system is the signal to noise level, as the reflectivity of the FBGs is rather low. Next to that, due to the time delay differentiation, the sensors must be placed far enough apart in order for the detector to differentiate between them [60]. Lastly, the maximum distance between the interrogator and the 'last' sensor is limited, as

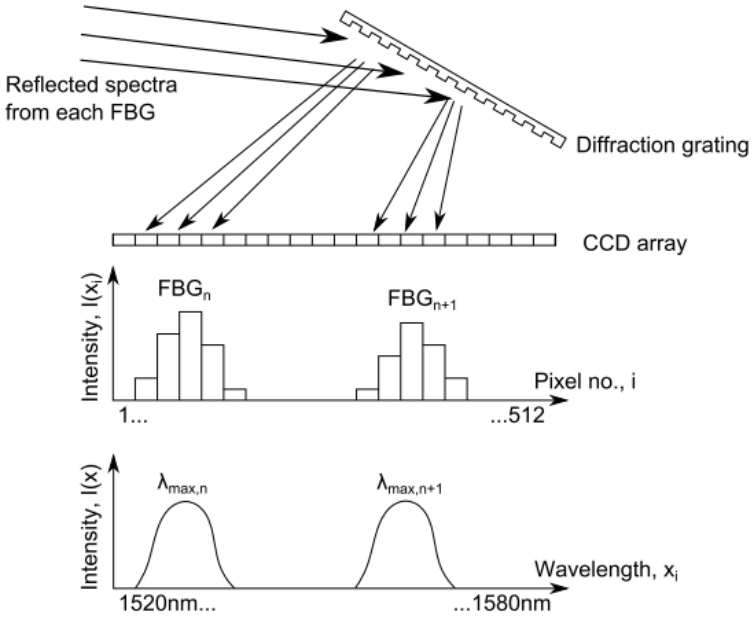

Figure 2.19: Principle of operation of a CCD based interrogator (Top), Signal intensity received per pixel (Middle), Signal intensity interpolated and converted to wavelength (Bottom) [31]

the pulse time delay would drastically reduce the scanning speed. Due to the minimal needed spacing between the sensors, TDM interrogators are not suitable for bearing sensing, as the spacing between the sensors is in millimeter range.

The WDM technique uses (highly reflective) FBGs with different Bragg wavelengths. By spacing the Bragg wavelengths sufficiently, no spectral overlap occurs during operation and the interrogator is able to differentiate between the different FBGs by spectral analysis. As can be observed, the maximum allowed number of sensors is limited by the wavelength range and resolution of the interrogator (and wavelength shift of the FBGs). As with the TDM technique the number of sensors was limited by the wavelength reflectivity of the FBGs. As one can see directly, combining the two multiplexing technique is also possible, making incorporating a large amount of FBGs in a single fiber possible [9, 66]. The major drawback of such a combined technique system is the limited scanning frequency and the required spacing between sensors. The WDM technique on its own allows for very high resolution scanning however, the sampling speeds are lower compared to the TDM technique. Several high performance WDM, TDM and combined interrogator techniques are described and evaluated in [10]. For example, the interrogator shown in Figure 2.18 makes use of the WDM technique in order to distinguish the different sensors. One could combine this system with TDM, by adding an additional fiber with sensors and pulse the light source, still using the same detectors in order to measure with a multitude of sensors. One can directly see that by adding additional fibers/channels, the sampling speed goes down.

The CDM technique is essentially an extended version of the TDM technique. Instead of sending a single pulse to the sensor and wait for it to return, a unique set of pulses (a code) is send to each sensor. By predetermining the expected time delay, the unique code can be received again from the intended sensor. The major advantage of this technique over the TDM method is the speed, the code pulses can be send continuously, the interrogator does not have to wait for every sensor's return signal before sending a new pulse [41].

The PDM technique uses polarized FBG sensors with a known angle of polarization. The reflected wavelengths from the different sensors which are aligned to the unique angle of polarization to propagate through the fiber with the minimum interference and crosstalk. With the help of a polarization rotator and attenuator, one can seperate the reflected wavelengths for each sensor [69].

Peak Detection
Once the reflected or transmitted spectrum is received, the interrogator has to detect the wavelength shift in order to obtain the strain. This is done by peak detection and literature mentions several methods for this, they will be briefly described here. The first one is the centroid detection algorithm mentioned in [3]. It is given by the expression in Equation 2.11.

$$x_B = \frac{\sum_{i=1}^{N} x_i I_i}{\sum_{i=1}^{N} I_i} \tag{2.11}$$

Here x_i is the central wavelength of the i^{th} pixel and I_i the corresponding light intensity of that pixel. This expression can be interpreted as the geometric center of the reflective wavelength. Another common technique for peak detection mentioned is the quadratic fit algorithm. Here the expression given in Equation 2.12 should be minimized, with I_{fit} the approximated solution given in Equation 2.13 (a, b and c are constants) and w_i weighting elements [31].

$$\frac{1}{N}\sum_{i=1}^{N} w_i (I_{fit}(x_i) - I(x_i))^2 \tag{2.12}$$

$$I_{fit}(x_i) = ax_i^2 + bx_i + c \tag{2.13}$$

A peak detection similar to the quadratic fit algorithm is the Gaussian fit algorithm. The only difference is a different form of solution for I_{fit}, instead of the expression given in Equation 2.13, the solution is given in the form given by the expression in Equation 2.14. Here a_0 is the amplitude, μ the mean and σ the standard deviation of the Gauss curve [31].

$$I_{fit}x_i = a_0 \cdot \exp\left(-\frac{x-\mu}{2\sigma^2}\right) \tag{2.14}$$

Research has shown [31] that the fit algorithms are better performing than the centroid detection algorithm. However, when multiplexing a lot of sensors, doing high frequency sampling at a high resolution, the computational power needed for the fit algorithms may become problematic and no longer justifiable. Again there is a trade off between speed and accuracy.

Commercial off-the-Shelf Interrogators
Table 2.1 shows a list of interrogators together with their specifications. The interrogator listed in bold is used for the measurements performed on the prototype bearing. More information regarding the SmartScan SBI scanner is given in Section 3.1.3. As can be seen in the table, the used scanner has a rather low resolution, resulting in only 5-10 measurement points per FBG. This means the actual shape of the reflective wavelength is approximated and (important) details may be lost. This table shows that there are possibilities to use other interrogators with higher resolutions and comparable scanning frequencies, Commercial off-the-Shelf (COTS).

2.3.3. FBG Applications
Strain and temperature measurements are the most common sensing applications for FBGs however, other parameters could also be measured with the help of FBG sensors. Table 2.2 gives a set of examples of applications for FBG sensors, as described in [52]. Next to temperature and strain measurements, FBG sensors are also used for pressure sensing, vibration sensing, measurement of inclinations and magnetic field measurements, as described in [47]. As FBG sensors are small and immune to EMI, these sensors are also frequently used in medical instruments and applications, like described in [14, 17, 27]. Knowing that FBG sensors are used in a variety of applications gives confidence in their working principle and moreover, literature of FBGs in other applications may highlight common pitfalls when using these kind of sensors.

Table 2.1: Interrogator specifications as described in product data sheets from manufacturers

	Wav. [nm]	Rep. [pm]	Freq. [KHz]	Res. [nm]	Op. Temp. [°C]
Bayspec FBGA-IRS Series	1510 - 1590	2	5	0.001	-5 to 70
FAZT I4	1529 - 1568	<0.05	1	0.001	0 to 55
FAZT V4	1528 - 1568	0.01	1	0.001	0 to 55
FiberPro FI3200	1532 - 1558	<3	100	0.001	-5 to 50
HBM FS22	1500 - 1600	1	0.001	0.001	10 to 40
I-MON 256 HS	1525 - 1570	3	35	<0.0005	0 to 50
Micron Optics si255	1500 - 1580	2	5	0.002	-20 to 60
Micron Optics FFP-TF2*	1520 - 1570	?	8	0.026	-20 to 80
National Instruments PXIe 4844	1510 - 1590	1	0.01	0.001	0 to 55
Peekel Instruments SPK 155	1525 - 1570	3	15	0.01	0 to 50
Redondo FBGT-500/1200**	1520 - 1570	5	0.1	0.005	?
SmartScan SBI	**1528 - 1568**	**<1**	**25**	**0.1**	**-20 to 75**
Technobis CasGator HR	1538 - 1562	0.25	19.2	?	-20 to 55
Technobis Deminsys	830 - 870	2	20	?	-15 to 55

* This interrogator is manufactured to customer specifications

** Specifications for FBGT-2008-1040 are not available however, FBGT-500 and FBGT-1200 are assumed to have similar specifications. (Major differences are in number of sensor channels and maximum sampling frequency, which is only relevant at lower resolution scans)

General note: Not all manufacturers give maximum sampling speeds at maximum resolution, some sampling speeds in the table may therefore only be reached for low resolution scans.

Table 2.2: Examples of Bragg grating applications [52]

Area	**Examples**
Civil	Structural Health Monitoring (SHM) during construction, load tests and service life Smart reinforcement of structures
Energy	Temperature monitoring of overhead power lines Temperature mapping in high power generators Hot spot monitoring in high voltage power transformers Vibration monitoring in high power generators Integral blade monitoring system for wind generators
Oil & Gas	Monitoring of Pressure and Temperature Down-Hole Detection of low levels of methane Surveillance of pipeline integrity with sensor array
Aerospace	SHM in aircraft fuel tanks or other structures Monitoring of in-flight refueling system Temperature monitoring in telecom satellites SHM in composite structures (embedded)[54]
Transportation	Automatic weighing and characterization of trains SHM of ship hulls
Telecommunication	Production of cables Filters

3

Problem Statement and Analysis

This chapter will discuss the problem statement and analysis. It will start with describing the used test setup by SKF for measuring the Gusto bearing in Section 3.1, Section 3.2 will describe the differences observed by SKF during these prototype measurements, next Section 3.3 will describe possible causes for these observed differences and lastly Section 3.4 will discuss what data, test setups and equipment are available at SKF for this project.

3.1. Test Setup

This section will give a description of the bearing used during the prototype measurements, it will also describe what FBG sensors are attached to the bearing and how they were manufactured and bonded to the bearing, lastly it will discuss the used interrogator by SKF during the prototype measurements.

3.1.1. Gusto Bearing

The bearing used by SKF during the prototype measurements was a 6022 SKF bearing (See Appendix A for the data-sheet of the 6022 bearing) equipped with 32 FBG sensors. This particular prototype bearing was named the Gusto bearing. A drawing of the Gusto bearing is shown in Figure 3.1, the figure indicates a '45 (deg)' in the lower right, it is known that the precise location of the FBG sensors in the bearing are unknown. Fortunately, the spacing of the FBGs and wavelength characteristics are known. The uncertainty of the location will therefore only have an impact on the strain peaks, as the load applied may not exactly align with the FBGs in the actual prototype. For the purpose of this research project the peaks are not the main point of interest, it is the strain minima that are interesting here. The overall pattern of the strain minima are not affected by this uncertainty. The arrow in white represents the direction of the applied load, for this research project, only the sensors indicated by the purple line(in the loaded area), in Figure 3.1, are of interest. The purple line (and yellow line) represents two fibers, each containing eight FBG sensors. The sensors are spaced as shown in Figure 3.2. If the Gusto bearing is loaded in the direction of the FBGs in the yellow line, only the sensors in the yellow line are of interest. The rolling element bearing was tested in a gearbox of a jacking system, see Figures 3.3 and 3.4.

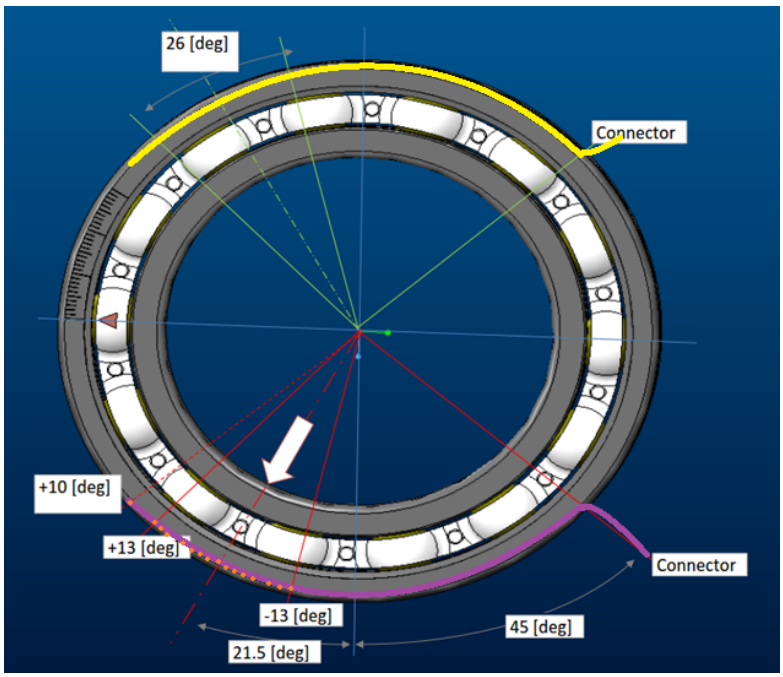

Figure 3.1: Bearing equipped with FBG sensors in the outer ring, used to obtain the measurement data

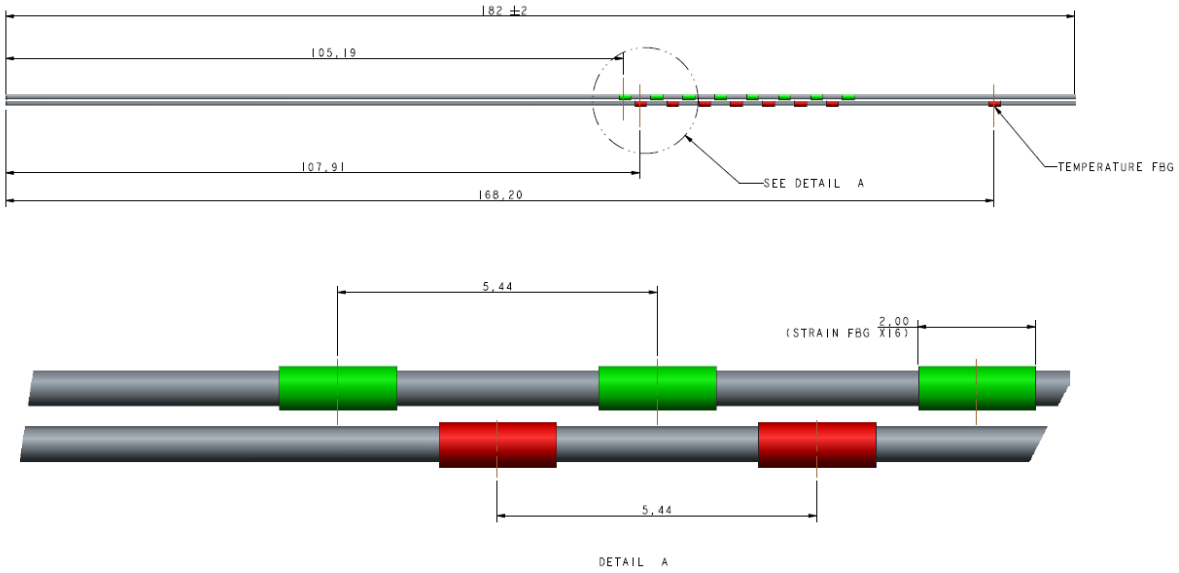

Figure 3.2: FBG Sensor layout, all dimensions in mm

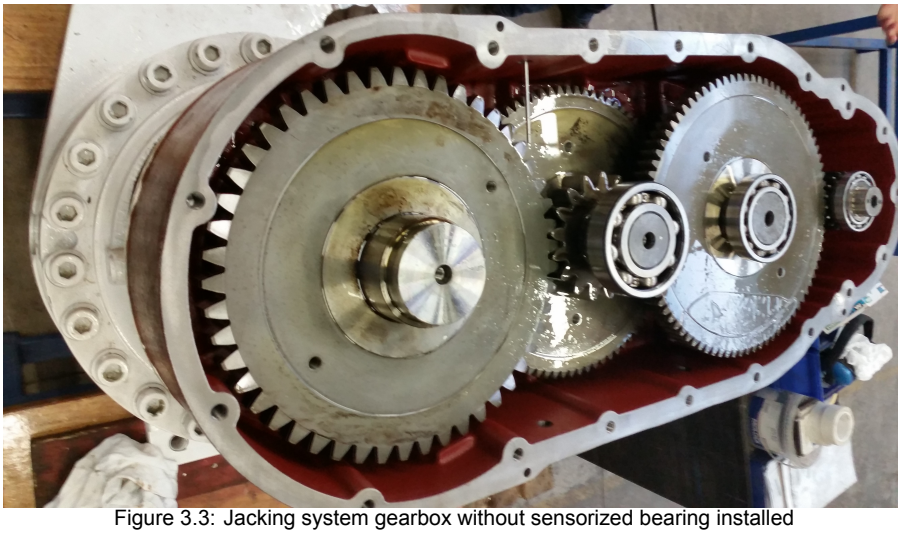

Figure 3.3: Jacking system gearbox without sensorized bearing installed

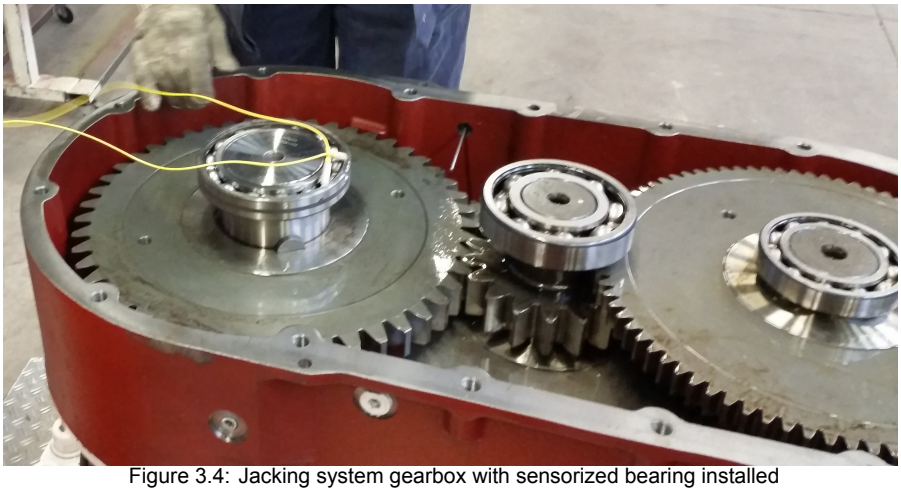

Figure 3.4: Jacking system gearbox with sensorized bearing installed

3.1.2. FBG Sensors

In order to get a better understanding of the observed reflective spectra, it is important to know what types of FBG sensors were used in the test setup and how they were attached to the bearing. This subsection will discuss the manufacturing technique used for the sensors in this particular case and the benefits and drawbacks for using that technique. Next it describe how the sensors were attached to the bearing surface.

Manufacturing Technique

The manufacturing method used for the FBG sensors used is the so called phase mask method, which was first described by [1, 23]. The illustration in Figure 3.5 gives an overview of the technique. It uses an ultraviolet laser beam that is diffracted by the phase mask. The phase mask is made from silica glass which is transparent to ultraviolet light. On one side of the mask a one dimensional periodic surface relief structure is etched using photolithograpic techniques [24]. The optical fiber is placed directly underneath the etched surface and the ultraviolet light is diffracted periodically over the fiber, inscribing the gratings that cause the reflection of the Bragg wavelength. The phase mask technique greatly simplifies the manufacturing process of the FBG compared to the old techniques, internal writing [22] and the holographic technique [58]. However, the gratings are still high performance and the phase mask technique allows for easy alignment of the fiber, making the manufacturing process more consistent. The used FBGs have a full width at half maximum (FWHM) of 1.2 nm. Several studies were performed on performance issues of FBGs manufactured with the phase mask technique however, this

is outside the scope of this review. For this project it is assumed the FBG sensors are manufactured to the specifications claimed.

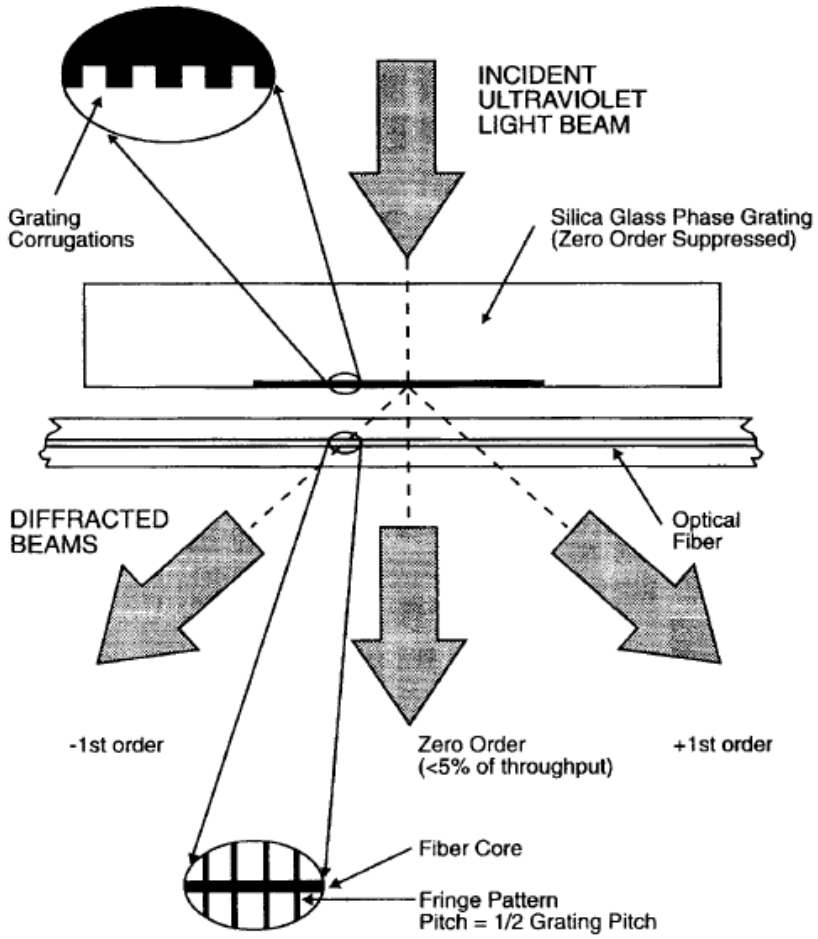

Figure 3.5: Schematic overview of the phase mask manufacturing technique for FBG sensors [24]

Bonding Method

The sensors in a single group are split over two fibers, which are both located in a groove in the outer ring of the bearing. Figure 3.6 illustrates the groove in the outer ring of a bearing, note that the this figure shows a bearing with multiple grooves. As the splitting of the sensors over two fibers was a late adjustment to the design, both fibers are located in a single groove for this case. The fibers are (uniformly) pre-strained by attaching the fibers to the steel with a small amount of glue at the end. Next, the placement of the fibers in the groove was completed by adding P-adhesive between the fibers and steel and with the help of the clamping device shown in Figure 3.7, the fibers were clamped to the steel. The P-Adhesive is capable of elongation under strain together with the host material and FBG, plus has a wide operating temperature range (Approximately from -260 to 360 °C). The fibers are coated with a polyamide based epoxy, this will create a smooth finish of the bearing outer ring and will protect the fibers.

Figure 3.6: Illustration of the outer ring groove including fibers

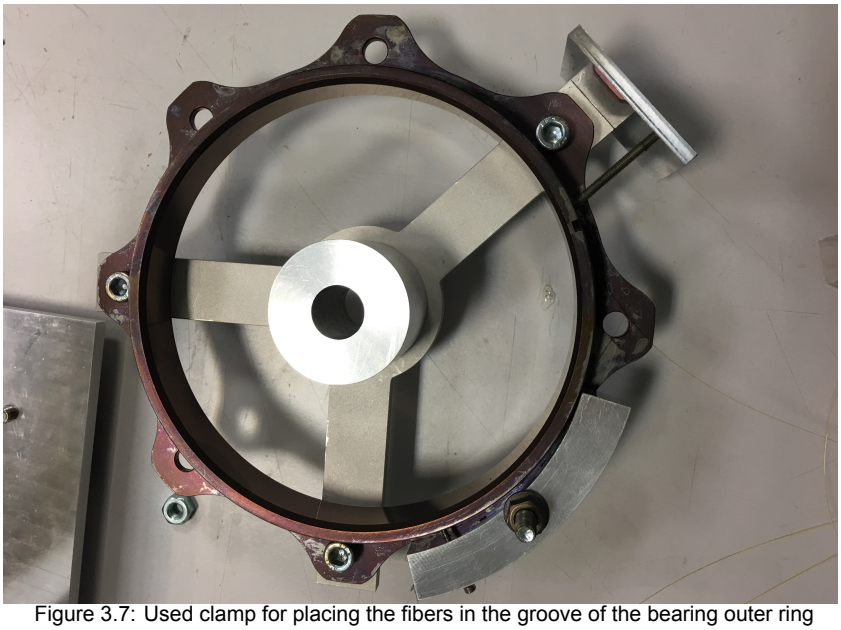

Figure 3.7: Used clamp for placing the fibers in the groove of the bearing outer ring

3.1.3. Interrogator System

The used interrogator in the test setup is the SmartScan SBI Interrogator unit, shown in Figure 3.8. The specifications of the interrogator are shown in Table 3.1. The interrogator unit supports 16 sensors per channel, however for this particular case the sensors' spectral responses would overlap as their spacing on the fiber would be very small. Therefore, the 16 sensors are split over two channels, increasing their (wavelength) spacing. The used interrogator has a resolution of around 0.1 nm (the wavelength range of the SmartScan is divided up into 400 channels, meaning for a 40 nm SmartScan these are spaced 0.1 nm and for a 35 nm SmartScan at about 0.088 nm [35]) meaning around 6 to 12 points per Bragg wavelength peak can be obtained. This will result in a low resolution of the actual reflective peak, meaning that secondary peaks and the general shape of the peak is lost. The interrogator is however able to scan at a very high frequency, meaning every rolling element is detected by the FBG sensors, even when the bearing is running at a considerable speed (1000 rpm and higher).

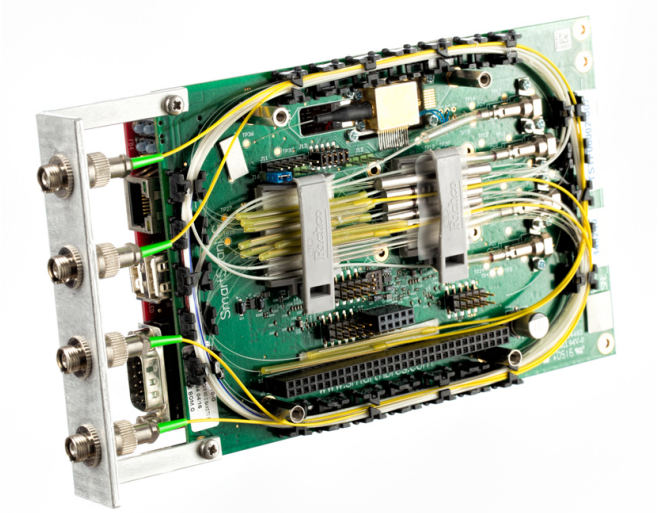

Figure 3.8: SmartScan SBI Interrogator unit used in the test setup

Table 3.1: SmartScan SBI Specifications [73]

Measurement and Processing	SmartScan SBI	SmartScan SBI Lite
Wavelength Range	40 nm (1528 – 1568 nm or 1568 – 1608 nm)	
Number of Optical Channels	1, 2, 3, 4	
Maximum Number of Sensors / Channel	16	
Scan Frequency (all sensors simultaneously)	2.5 kHz	250 Hz
Scan Frequency (per each sensor in turn)	25 kHz	-
Repeatability,	<1 pm	
Wavelength Stability	<5 pm over operating temperature range, +/- 20 pm over 25 years	
Dynamic Range	27 dB	
Suitable FBG profile (FWHM)	Minimum >0.2 nm, >0.5 nm recommended	

3.2. Observed Differences in the Reflective Spectra

The company SKF is developing a bearing equipped with Fiber Bragg Grating sensors. An initial prototype showed measurement differences between multiple sensors on a single rolling element bearing. A selection of the measurements performed by SKF is presented in Figure 3.9, this figure shows the strain over time of a single sensor. The strain is calculated from the wavelength shifts observed by the interrogator. Every peak in the graph represents a rolling element in which is passing the sensor, between two elements passing the sensor, the strain is at a minimum. Figure 3.10 shows again the strain measurement of a single sensor. However, here all peaks of a rolling element passing the sensor are superimposed. This is done for 60+ passes of a rolling element in the bearing. As can be seen the overall strain measured by the sensor is roughly the same for all elements and remains similar for a second passing of an element, the loading remained constant over the time of the measurement. Figure 3.11 shows a comparable graph as the one shown in Figure 3.10 however, here multiple sensors are plotted next to each other.

The sensors have a length of 2.0 mm and have a spacing of 5.44 mm, in theory all sensors should measure the same strain distribution. The radial load in the direction of the FBG sensors, slight differences in peak strain are expected (See Figure 2.4, the small spacing between the FBGs means all sensors are approximately subjected to the same force). The strain patterns in between two rolling elements passing however, are expected to be similar. As can be seen in the figure, the side lobes of the peaks are not consistent and not always symmetric. Possible causes for these phenomena are discussed in

the next section.

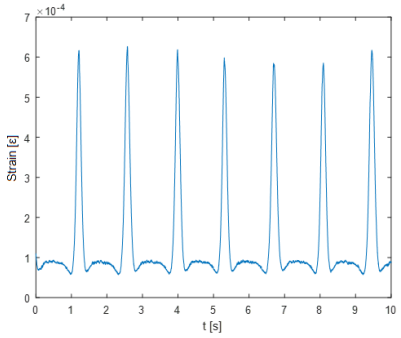

Figure 3.9: Strain signal over time of a single FBG sensor, calculated from the wavelength shift measured by the interrogator [74]

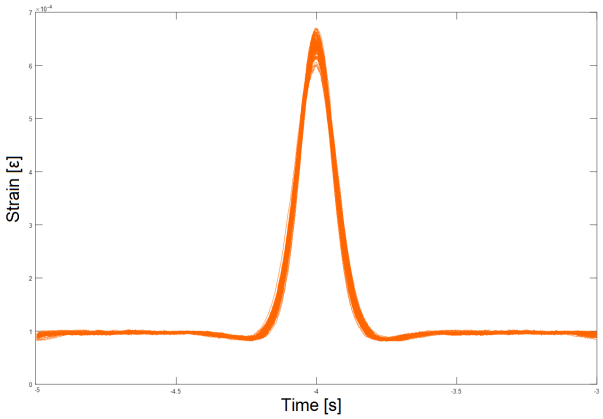

Figure 3.10: Superimposed strain signal of 60+ rolling elements of a single FBG sensor [74]

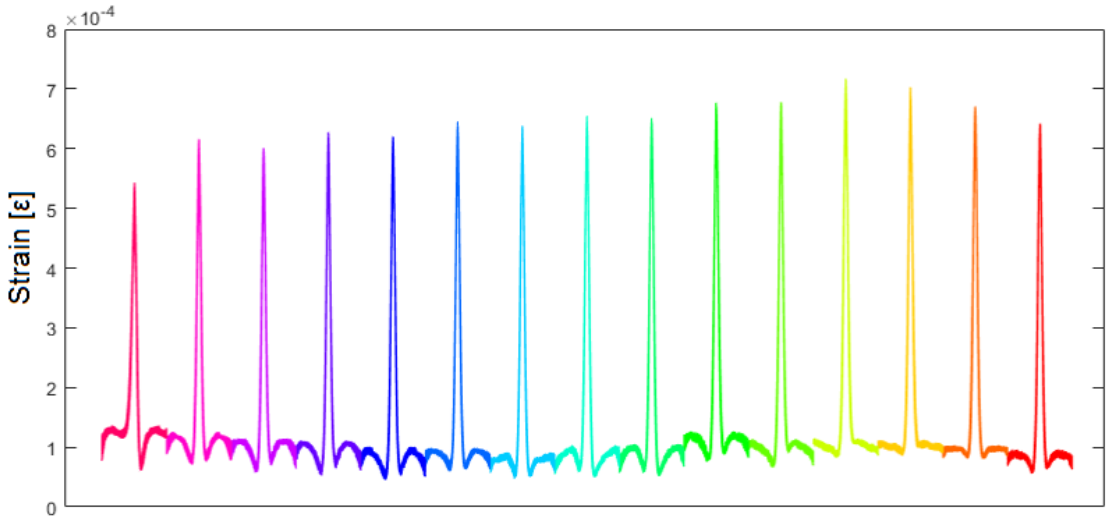

Figure 3.11: Superimposed strain signal of 60+ rolling elements of multiple FBG sensors in close proximity of each other [74]

3.3. Possible Causes

This section will describe the possible causes for the observed differences. From the literature study, several causes for the strain differences were found, these are listed in this section from Subsection 3.3.1 to 3.3.3.

3.3.1. Strain Transfer Model

The FBG sensors used for the measurements are not in direct contact with the host material and certainly not in direct contact with the to be measured part of the bearing. The sensor is covered in a cladding and protective outer shell. Furthermore, it is bonded to the groove in the outer ring of the rolling element bearing with a certain bonding material. See Figure 3.12 for a visual representation.

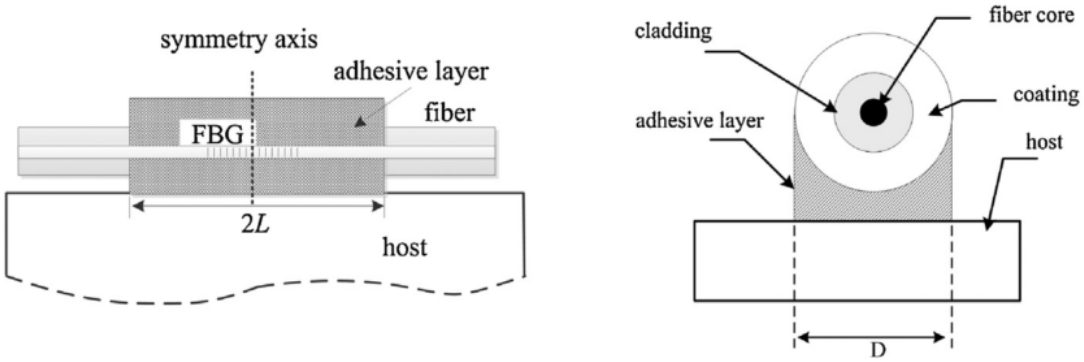

Figure 3.12: Surface bonded FBG structure (left) and cross-section view (right) [46]

Next to these layers, the groove in the outer ring of the bearing will also be subjected to different strains compared to the outer raceway of the bearing. The material between the outer raceway and the groove on the outer ring may have an influence on the direction and magnitude of the strain measured by the sensor.

This difference is described by the strain transfer model, not using such a model may cause measurements inconsistencies. Studies performed on the strain transfer model, for example [20, 75, 76], do show certain influences of the different layers on the measured strain. The most dominant difference is however, the magnitude of the strain. The overall distribution of the strain is only influenced in some cases. Nevertheless, not using a strain transfer model at all or using a model with possible errors or simplifications may have a contribution to the differences observed. One may think of different bonding characteristics between two sensors and misalignment between sensors, these factors could be included in the strain transfer model as well. Next to the strain transfer between the different layers present, the two fibers are placed next to each other in the same groove in the outer ring of the bearing, they may have an influence on each other. The exact spacing between the two fibers is not known, however the presence of the second fiber may be added to the strain transfer model and evaluated for different spacing.

3.3.2. Non-uniform Strain

Non-uniform strain in the axial direction of the FBG can lead to chirping of the FBG [49], the chirped grating structure is described in Subsection 2.3.1. Several studies show [7, 81] that the reflective spectra of FBGs under non uniform axial strain differ from reflective spectra of FBGs under uniform strain. The study in [26], shows that when a FBG is subjected to a linear strain gradient, the reflective spectra will show multiple peaks and the width of the reflective spectra will increase with increasing strain. In the same study, the FBG was subjected to a quadratic strain field, this resulted in reflective spectra that showed little shift in the Bragg wavelength, increased width of the reflective spectra for increasing strain and additional peaks in the reflective spectra.

The used interrogator by SKF in the initial test, described in Section 3.1.3, was not able to distinguish multiple peaks in the reflective spectra, as the scan resolution of the interrogator was not high enough. It could be possible that the FBGs in the rolling element bearing are subjected to non-uniform strain, as the contact point between the rolling element and the raceway is very small. When this results in spectra peak deformations, this could lead to incorrect peak detection by the interrogator, giving incorrect strain values. It is advised to use an interrogator that is capable of measuring more points in the reflective spectra of the FBGs, in order to obtain a more detailed view of the reflective spectra.

The study in [48] describes that the shape of the non-uniform strain on a FBG will also have an influence on the strain transfer efficiency between the host material and the fiber. This phenomena has to be incorporated in the strain transfer model in order to get the most accurate strain distribution in the rolling element bearing. Next to non-uniform axial strain, the FBGs may also be subjected to transverse strain. The study in [8] describes that this may lead to birefringence, this will result in polarization dependent loss (PDL) and differential group delay (DGD). These effects on the reflective spectra could be used

in order to retrieve any transverse forces the FBG is subjected to, again a high resolution reflective spectrum is needed in order for this to work. In the study in [39], the ability to measure both axial and radial strain with a single FBG is investigated. For this project it is assumed that the transverse strains in the rolling element bearing are very small and therefore neglected in this case.

3.3.3. Bearing Defects

Rolling element bearings are manufactured with high precision and care however, defects may always occur. Also damage propagation in the rolling element bearing during service may occur. Even small defects in the bearing raceway or rolling elements may cause unexpected strain returns from the sensors. As described in Section 2.2, various models exist that are able to predict loads in bearings that have defects. Common defects could be modeled and the calculated loads could be compared to the strain patterns observed by SKF. A better understanding of the influence of defects on the strain pattern is essential in order to understand the measurement data. Next to defects, the influence of small miss-alignments and clearances in the bearing on the reflective spectra could be investigated.

The study performed in [36] describes the displacements of the outer raceway of a rolling element bearing related to the number of revolutions. As can be seen in Figure 3.13 the displacements differ over the service lifetime of the bearing, this is explained in the study by raceway deformations and damage propagation in the raceway. The higher frequency displacements, after 10k revolutions, are explained as secondary damage in the quenched layer of the bearing raceway. In the study, sensors based on the eddy current principle were used. In order to reduce the bearing lifetime for testing purposes, the maximum load applied was 2.7 times the maximum load carrying capacity of the rolling element bearing, the estimated lifetime with this load applied was 26k revolutions. The above described phenomena should also be considered by SKF when measuring bearing loads with optical sensors over a longer period of time.

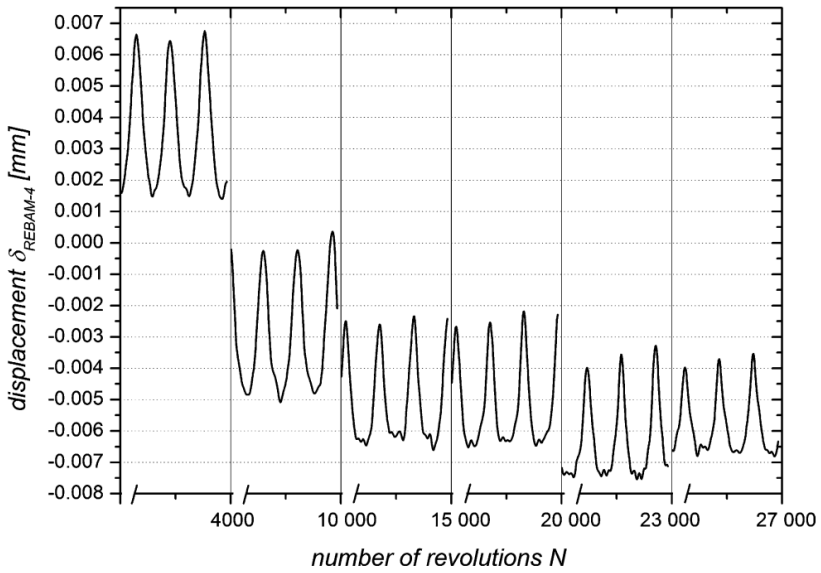

Figure 3.13: Outer ring displacements in relation to the number of bearing revolutions [36]

3.4. Available Equipment and Data

In order to give a complete overview of the available data, all bearings equipped with FBGs, available at SKF will be described shortly in this section. Furthermore, it will be indicated whether test data is already available for the bearings mentioned.

3.4.1. Wartsila

This test setup contained several bearings equipped with FBG sensors. It contained two Spherical Roller Bearings (SRBs), shown in Figure 3.14, both equipped with two fibers, both containing six strain FBGs and one temperature FBG. Both fibers where placed in the loaded zone in a groove in the outer

ring, the loaded zones are shown by the red arrows in Figure 3.15. The test setup was also equipped with one Spherical Roller Thrust Bearing (SRTB), equipped with four strain FBGs and one temperature FBG. All FBGs in this test setup have a length of 2 mm. Because the reflective spectra output requires more data points, the frequency is lower compared to the peak data output. The reflective peak points from these tests were sampled at a frequency of 2.5 kHz and the complete reflective spectra at 10 Hz.

Figure 3.14: Spherical Roller Bearing [71]

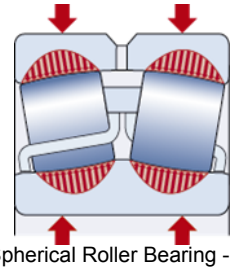

Figure 3.15: Spherical Roller Bearing - Rolling Element Load Distribution [71]

3.4.2. FuPro

FuPro is a test setup consisting out of four SRTBs. This is a new test setup and no test data is available from this test setup yet. Not all bearings will be delivered within the time slot of this project, most likely only one bearing will be available for testing for this project. All bearings will be equipped with 3x14 strain FBGs with a sensor length of 5 mm. The sensors are divided over 3 grooves. The differences between the four bearings is in the locations of the grooves in the outer ring and the depth of the grooves.

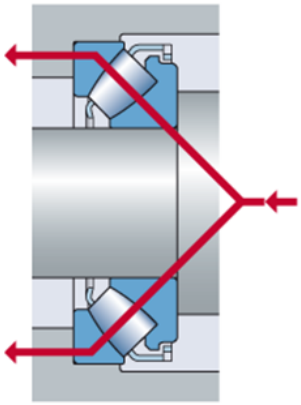

Figure 3.16: Spherical Roller Thrust Bearing [71]

3.4.3. Demonstrator

The Demonstrator bearing (Single Row Deep Groove) is equipped with 4 FBGs however, only 2 FBGs are loaded in this setup. The demonstrator bearing is equipped with FBGs with a length of 2mm. Exact locations of the FBG sensors in the bearing are unknown, so exact load determination could be a problem. However, this setup could be used in order to obtain a better understanding of the different phenomena seen in the reflective spectra of the FBGs while attached to the bearing.

3.4.4. Gusto

The Gusto bearing is, just like the demonstrator bearing, a Single Row Deep Groove ball bearing, for detailed dimensions and additional data see Appendix A. The strain readings from this particular bearing gave the initial reason for this research project. The differences between the strain readings from the FBG sensors attached to the bearing cannot be explained. The Bearing was tested in a gearbox of a jacking system. It was running at low speeds, 0.5 to 2 rpm. Only reflective peak data is available from these tests, no reflective spectra data. Because of the way the gearbox was loaded, the load vector changed with changing rotation direction of the gearbox, hence only one rotation direction measurement is available per set of sensors.

3.4.5. Test Object

The Wartsila bearings are not available for further testing. The FuPro bearings add extra complexity to the problem because of the way they are loaded, they are therefore not considered for this project. The Demonstrator bearing only has two FBGs that are loaded and that are not in close proximity to each other. The Gusto bearing is available for testing and has sensors in close proximity of each other. This was also the bearing that showed differences in the strain peaks from sensors to sensor. This bearing is therefore selected for further testing. Testing will be done with the use of the NI PXIe 4844 interrogator, which is capable of scanning the reflective spectra at a resolution 25 times higher compared to the prototype testing done by SKF, making use of the SmartFibers SBI interrogator..

4

Methods and Materials

In order to evaluate the reflective spectra of the FBGs, it has been chosen to perform additional tests on the Gusto bearing, making use of the NI PXIe 4844 interrogator. This interrogator is able to scan the reflective spectra with a resolution 25 times higher compared to the prototype measurements performed by SKF. These tests have been separated into two phases, phase one will only consider temperature as a variable, while the second phase will focus on loading the bearing. This chapter will describe the two test phases. The first test phase is described in Section 4.1 and the second test phase is described in Section 4.2. Both proposed test will make use of the NI PXIe 4844 interrogator, Section 4.3 will describe how the interrogator was used and what data was obtained from the interrogator.

4.1. Test Phase I

In order to gain a better insight in the reflective spectra of the bearing, the bearing is first measured without any load applied to it. This section will describe the goal, method and hypothesis of these measurements.

4.1.1. Goal I

The goal of this test is to answer the following questions,

- *"Are all FBG sensors attached to the Gusto bearing giving a symmetrical spectra in the operating temperature range of the bearing?"*
- *"Are the FWHMs of all FBG sensors attached to the Gusto bearing constant in the operating temperature range of the bearing?"*
- *"Do the peak shapes of all FBG sensors attached to the Gusto bearing stay the same in the operating temperature range of the bearing?"*
- *"Is the peak displacement due to thermal expansion the same for every sensor?"*
- *"Is the peak detection algorithm used by the interrogator in the prototype test valid for all the obtained reflective spectra?"*

4.1.2. Method I

This initial set of measurements will focus on the bonding characteristics between the FBGs and the bearing. It will be investigated whether the bonding material caused unwanted strains on the FBGs. This will be checked for the most typical temperatures the bearing reaches during operation, this has been set to 20°C to 100°C. The bearing is equipped with two temperature FBGs, however as these may also subject to possible pre-strains; two thermocouples will be attached to the outer ring of the bearing at the location of the strain FBGs, in order to read out the temperature of the bearing during the test. The used interrogator for the prototype tests performed by SKF was only capable of measuring the reflective spectra at a resolution of 0.1 nm. For this set of measurements the National Instruments PXIe-4844

interrogator will be used, which is able to scan the reflective spectra at resolution of 4 pm. The NI interrogator is however only capable of scanning at a frequency of 10 Hz, which is slow compared to the 2.5 kHz scanning frequency in the previous tests. However, the test proposed here will be a static test, high scanning frequency of the interrogator is therefore not required. During these measurements the temperature is the only variable, the bearing and fibers will be kept stationary during the course of the measurements (Due to birefringence effects in the optical fibers). The list below summaries the needed equipment for the temperature test.

- Heraeus 0914 oven
- 6022 SKF Bearing equipped with 32 FBG sensors over 4 channels
- 2 Thermocouples with accompanying read out equipment
- National Instruments PXIe 4844 Interrogator
- National Instruments PXI Express Chassis
- PC with PXI controller and Labview
- Rig for placing all equipment near oven

For this set of measurements, the Heraeus oven was used at the TU Delft, This oven is also shown in Figure 4.1. The thermocouple outputs were processed by a separate pc (left pc). The provided software with this pc was not able give UTC time stamps to every measurement, therefore the start time of the thermocouple measurements was noted in order to synchronize them with the UTC time stamped FBG measurement data. This method will be verified by analyzing the FBG and thermocouple data at the time of oven shutdown. At oven shutdown a sharp drop is expected in the temperature read out of the thermocouple and a shift of the FBG peak locations in the reflective spectra. The thermocouple data will be received every five seconds due to hardware limitations, small time differences between the two data sets are therefore expected. The pc in the right of Figure 4.1 receives the FBG reflective spectra data from the NI interrogator (bottom right), showing the control panel from the LabVIEW VI, including the real time reflective spectra graph of the FBGs.

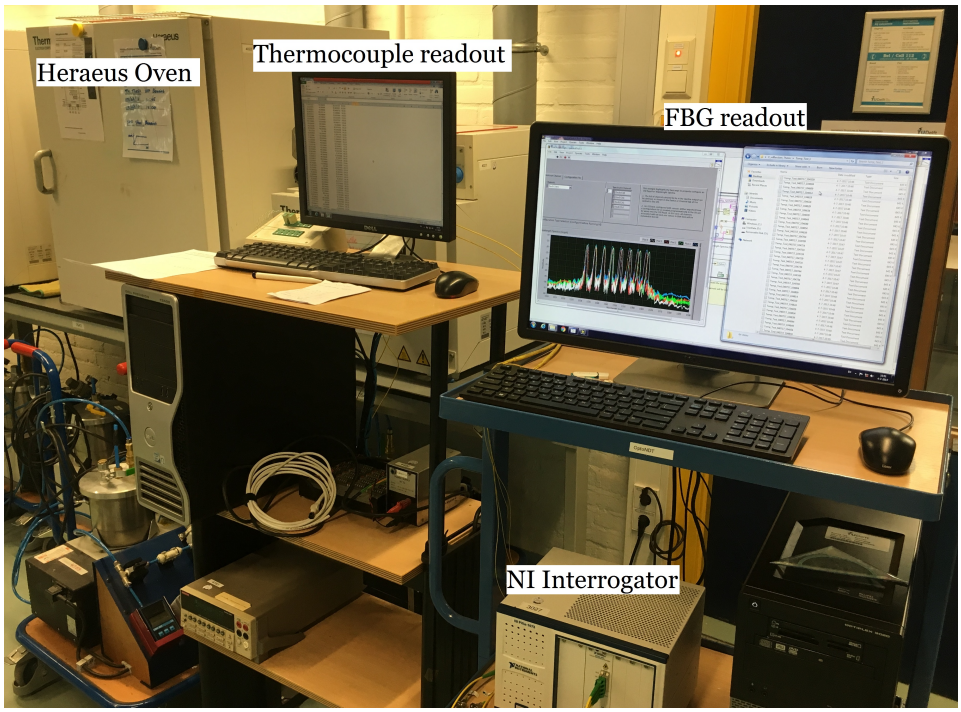

Figure 4.1: Test setup for phase I test

4.1.3. Hypothesis I

For the first phase, no load is applied to the bearing. If the bonding is uniform, the reflective spectra should be symmetric, as shown in Figure 4.2. This will also be the case if the FBGs are pre-strained. It could also be the case that the bonding is not completely uniform and a certain pre-strain is applied to the sensors. This strain can be influenced by temperature as well, therefore the measurements are performed at different temperature levels. When an applied pre-strain to the FBGs is not uniform, the peaks in the reflective spectra of the affected FBGs could be splitted, as shown in Figure 4.3, or asymmetric, as shown in Figure 4.4, or both. When the reflective spectra are no longer uniform and a peak detection algorithm is used that does not account for this, the resulting strain readings may be incorrect. Next to the possible changes in shape of the reflective peaks with temperature shifts, the peaks in the reflective spectra are expected to move due to the temperature influence. The movement of the peaks in the reflective spectra should be the same for every sensor, as temperature is the only variable in this test and is assumed to be uniform over the bearing. If the shifts of the peaks are different per sensor, than this could also indicate bonding inconsistencies.

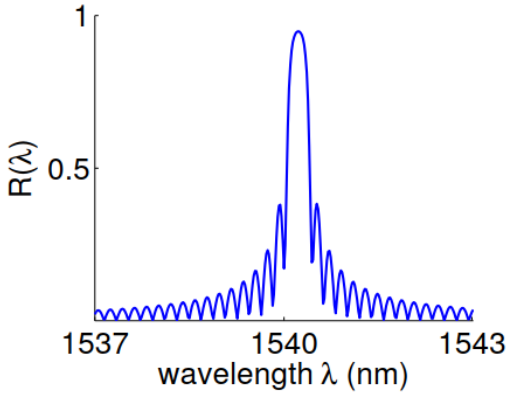

Figure 4.2: Reflective Spectra FBG - Symmetric [38]

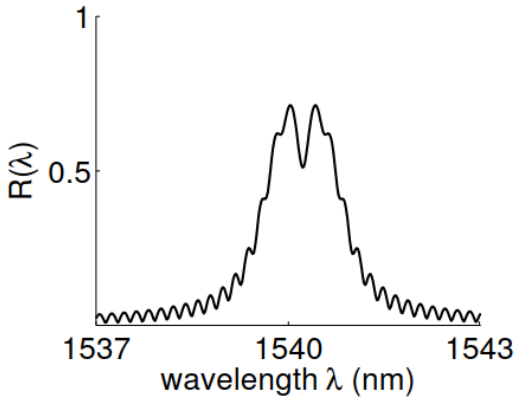

Figure 4.3: Reflective Spectra FBG - Peak Splitting [38]

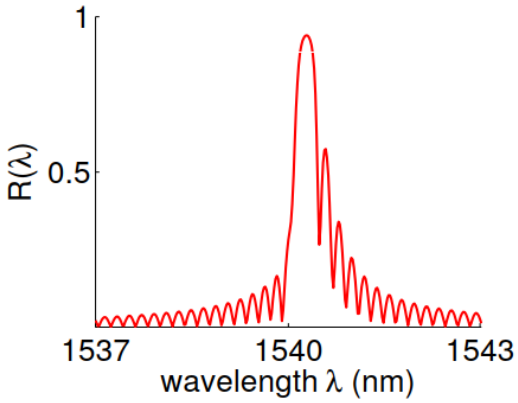

Figure 4.4: Reflective Spectra FBG - Asymmetric [38]

4.2. Test Phase II

This section will describe the goal, method and hypothesis of the second test phase. This test will consist of actually loading the bearing in order to gain a better insight in the reflective spectra when load is applied to the outer ring by the rolling elements.

4.2.1. Goal II

The goal of this test is to answer the following questions,

- *"Is the assumption, the sensor with the lowest Bragg wavelength is located closest to the connector, correct?"*

- *"Are all sensors giving the same spectral response for the given load cases (peak load and distributed load)?"*
- *"Are all reflective spectra symmetric under loads for different rolling element positions w.r.t. the FBG sensors?"*
- *"Are changes in FWHM for each sensor for different load cases smaller than 5%?"*
- *"Is the spectra peak detection algorithm used by the interrogator in the prototype test valid for all the obtained reflective spectra?"*

4.2.2. Method II

The prototype tests by SKF were performed with the bearing installed in a gearbox, as shown in Section 3.1. For this setup the load applied to the bearing itself was theoretically determined, by monitoring the load inputs on both ends of the gearbox. By theoretically determining the load, some assumptions were made, for instance the links between the different gears were assumed to be ideal. This introduced some uncertainties about the exact load applied to the bearing. This set of test will apply load to the bearing directly, eliminating the previously mentioned uncertainties. It will give better insight in whether the sensors give similar response for similar load cases. In particular the sensors next to the contact point of the loaded rolling element with the outer raceway. Possible non-uniform strain present in this area may cause special cases in the reflective spectra of the spectra, as described in Section 4.1.

The proposed loaded test will use a short solid shaft which is of a smaller diameter than the inner/bore diameter of the Gusto bearing, except for 2 cm in the middle of the shaft, which will have the same diameter as the inner diameter of the Gusto bearing. By only having a small part of the shaft at the correct diameter, the bearing can be placed quickly over the shaft with only minimal amount of pressing. The bearing will be placed in a housing firmly attached to a base plate, see Figures 4.5 and 4.6.

Figure 4.5: Test Phase II - Test setup (1)

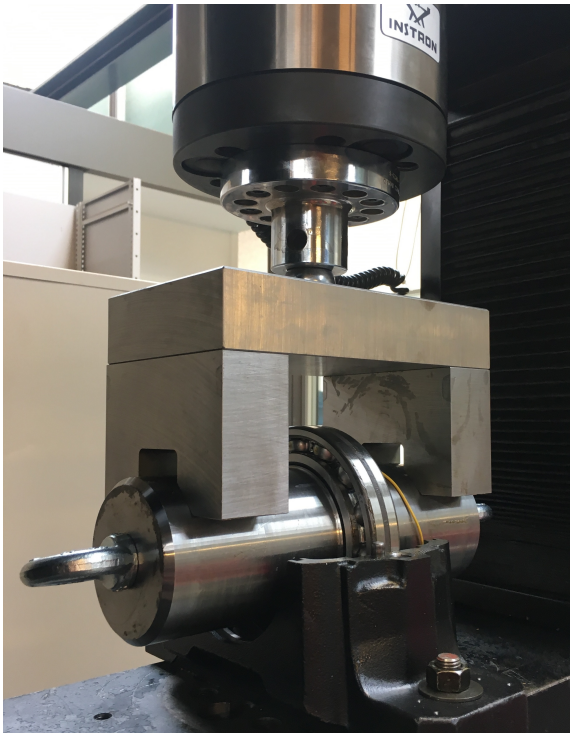

Figure 4.6: Test Phase II - Test setup (2)

The housing will make sure the bearing is in a fixed position during the measurements. A single bracket will be placed over the bearing and housing, making contact with the shaft on both sides of the housing.

Load input will be above the housing, exactly in the middle of the shaft by a ball joint. All measurements will be performed statically, the bearing will not be rotating during the measurements. The load can only be applied in one direction, by unloading and rotating the bearing in its housing, different sensors can be loaded. Also by unloading and rotating the shaft, different rolling element positions w.r.t. the sensors can be measured.

Before measuring the Gusto bearing under load, it is checked whether the assumption stating that the sensor with the lowest Bragg wavelength is closest to the connector, is correct. This is done by applying a small load to the shaft, small enough to still be able to rotate the shaft by hand, and rotate the bearing in clock wise direction. While doing this, the real time reflective spectra monitor is checked for peak shifts, depending which group of sensors is loaded, the direction of peak shifts over the monitor makes clear which sensor is located closest to the connector. Figure 4.7 shows the particular sensors of interest for the given load case, these sensors are likely to be subjected to a non-uniform strain (sensors in the area near the strain peak). Note that here the sensors are drawn on a single fiber, in the prototype design the sensors are divided over two fibers. The highlighted sensors are expected to be in an area of increasing or decreasing strain. The illustration gives a single test case, the load direction will be changed over the range of sensors, so all sensors will be subject to the possible change in strain distribution.

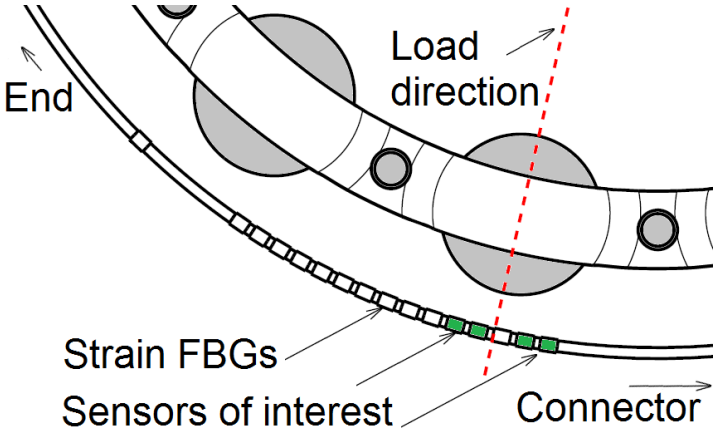

Figure 4.7: Gusto Bearing - Sensors of interest (green) for shown load condition (red)

The list below summaries the needed equipment for the loaded test.

- Load cell (100 kN)
- 6022 SKF Bearing equipped with 32 FBG sensors over 4 channels
- National Instruments PXIe 4844 Interrogator
- National Instruments PXI Express Chassis
- PC with PXI controller and LabView
- Bearing housing
- Load bracket
- Base plate
- Bearing shaft

4.2.3. Hypothesis II

For this test also non uniform strain is expected for sensors close to the applied load. These cases are also described in Subsection 4.1.3, shown in Figures 4.2, 4.3 and 4.4. This test will check whether the applied load over the sensors is non-uniform to an extent it will generate non-uniform reflective spectra from the sensors. Next to this it is assessed how the peak detection of the SBI interrogator differs compared to the NI interrogator, assuming the NI interrogater as baseline. Even when the peak detection is correct in both cases, if the distribution of the applied strain over the sensors changes, this may result in a change in the FWHM, as is explained in Figure 4.8. In this figure the applied strain is not uniform over the sensor, resulting in different reflective Bragg wavelengths per region of the sensor. Depending on the resolution of the interrogator, this may result in a wider reflective peak of the complete sensor [59], hence increasing the FWHM compared to a uniform strain distribution over the sensor. This test will investigate whether the FWHM changes by more than 5% for the different load cases.

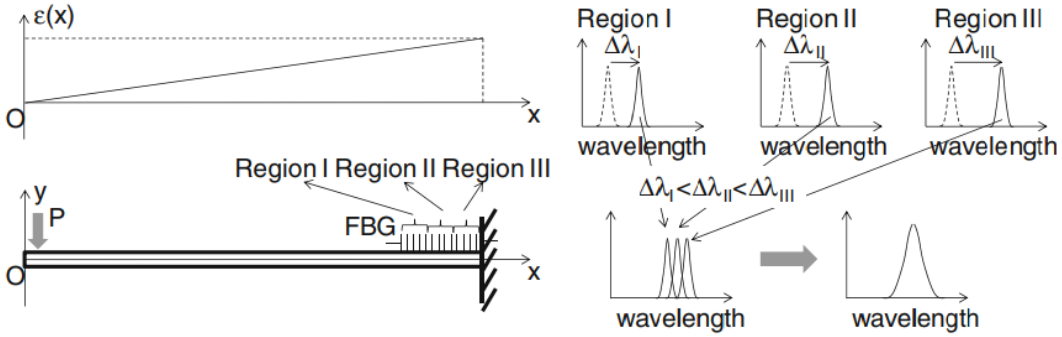

Figure 4.8: Reflective spectra of FBG subject to non-uniform strain [59]

In order to simulate peak widening in the reflective spectra, the amount of points in the peak detection are reduced. It is checked whether this has an impact on the detected peak for different sensors. This will show whether the peak detection method is valid for all load cases.

4.3. NI PXIe 4844 Interrogator Setup

Both proposed tests will make use of the NI PXIe 4844 interrogator. The NI interrogator comes with a Laboratory Virtual Instrument Engineering Workbench (LabVIEW), which is a system-design platform and development environment for a visual programming language from NI. The programs/routines LabVIEW runs are so called Virtual Instruments (VIs), NI provided an example VI for the PXIe-4844 interrogator. This VI is able to continuously plot the reflective spectra of all channels at 10 Hz. It is also able to take manual snapshots of the data and export them to a text file. This VI, shown in Figure 4.9, was used as a base file. In order to make the VI usable for this project, two extra functions were added, the first one being the ability to automatically and continuously write the data to tab-separated values (TSV) files and the second one being the ability to change the frequency of writing files.

Table 4.1: Data size NI PXIe-4844 Interrogator

VI Write Description	File Size (Mb)	Frequency (Hz)	Data/Hour (Gb)
Amplitude + Wavelength	1.348	10	47.39
Amplitude + Wavelength	1.348	1	4.74
Amplitude + Wavelength	1.348	0.2	0.95
Amplitude only	0.644	10	22.64
Amplitude only	0.644	1	2.26
Amplitude only	0.644	0.2	0.45

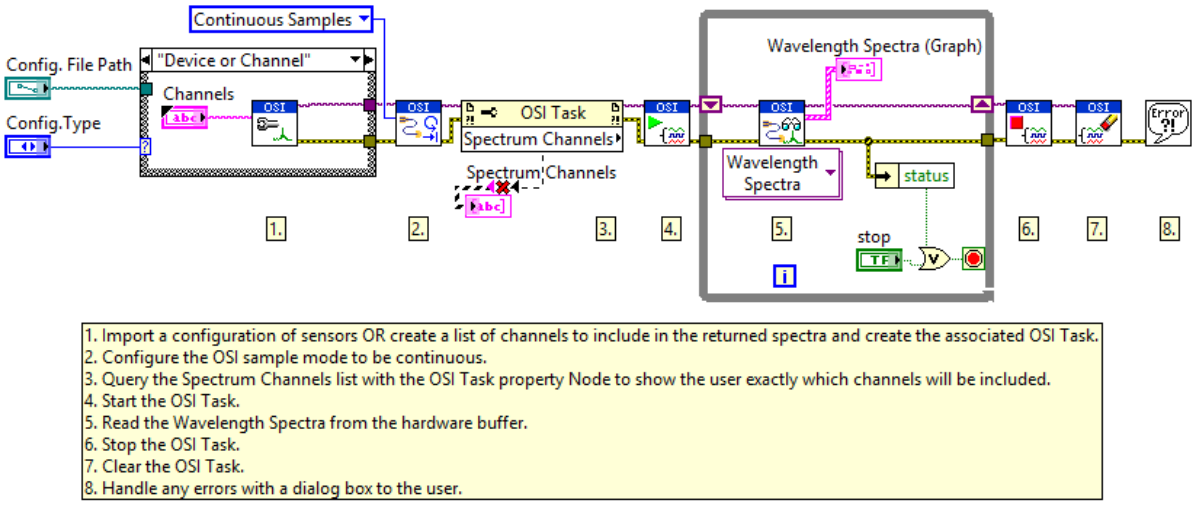

Figure 4.9: Example VI provided by NI for reading spectra (Modified layout for improved readability in report)

4.3.1. Writing Data to TSV Files

The example VI exported the wavelengths with the accompanying amplitudes to a text file, this generated files with a size of 1.35 Mb. However, the start wavelength and delta wavelength remains the same over the course of the measurements, it was therefore chosen to only extract the amplitudes from the OSI read block. This reduced the size of the data by more than 50 percent, as can be seen in Table 4.1. It was chosen to write every measurement in a separate text file with a time stamp in the file name, this made time stamps inside the files obsolete. Table 4.1 also gives the expected data per hour for different frequency settings. The data generation at 10 Hz is considered too high for this set of measurements. As temperature is the only variable in this test, the writing frequency will be set to 0.2 Hz, also keeping the generated data manageable.

4.3.2. Selecting Write Frequency

The provided VI was able to read the data from the interrogator at a frequency of 10 Hz, this was done by displaying the data in a plot file with a refresh rate of 10 Hz. It was found that if this loop was delayed, the hardware buffer was accessed, otherwise data was lost. The hardware buffer was however very limited and it was not desired to write the data at 10 Hz for this set of measurements. In order to write data at a lower frequency, without accessing the buffer, an IF statement was placed inside the read loop (Loop indicated by 5 in Figure 4.9. The plotting function was kept in the read loop in order to have a visual conformation of the system reading the FBG spectra and for keeping the loop counter running at 10 Hz. The IF statement was executed when the quotient remainder block of LabVIEW, with inputs the read loop counter and a frequency setting, was equal to zero. The output of the quotient remainder block is shown in Expression 4.1.

$$R_R = i - 50 \cdot \text{floor}(i/50) \tag{4.1}$$

As can be seen in Figure 4.10, the frequency setting was set to 50, meaning the program will write every 50th i; knowing that the interrogator is scanning at 10 Hz, gives that the program writes data

every 5 seconds without accessing the hardware buffer. The IF statement also contains a for loop for reading the amplitudes from all clusters from the OSI Read block. Every cluster contains the initial wavelength, the delta wavelength and the amplitudes of a single channel. The output is send to a text writing block. The remaining blocks provide the time stamped file names and main file path.

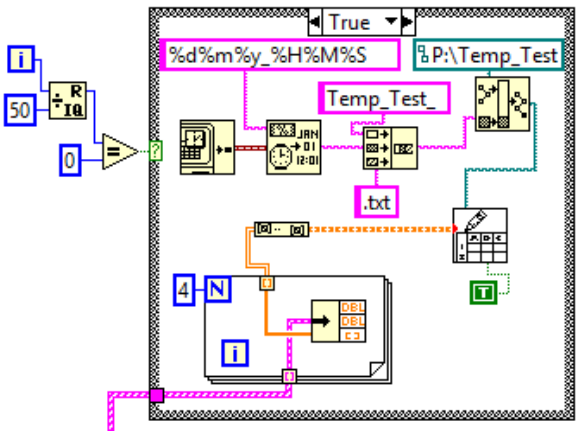

Figure 4.10: Added IF statement inside the read loop in the example VI provided by NI

Because of the limited availability of LabVIEW, it was chosen to only extract the raw measurements files from LabVIEW, further signal processing is done in Matlab.

4.3.3. Peak Detection Method

In order to obtain a rough estimate of the peak location, the findpeaks function in Matlab was used. This algorithm gave the maximum value and location of a peak, with a minimum set distance between two peaks of 750 points (3 nm) and a minimum peak height of -20 dB. From this algorithm, eight rough peak locations were obtained per channel per measurement. With the rough locations of the peaks known, the reflective amplitudes of a 1 nm radius around the rough estimate were collected. In order to assess every peak in the reflective spectra equal, a threshold of 0.05 reflectivity was taken. When the amplitude falls below the threshold, it is set to zero. The remaining amplitudes were used in Equation 4.2 in order to find the centroid peak location (Expression repeated below for convenience).

$$x_B = \frac{\sum_{i=1}^{N} x_i I_i}{\sum_{i=1}^{N} I_i} \tag{4.2}$$

The reason for choosing the Centroid peak detection is due to the fact that the interrogator used in the prototype testing by SKF uses the same peak detection method (note without threshold). This makes it easier to compare results. Other peak detection methods are described in Subsection 2.3.2 under Peak Detection.

5

Results

This chapter will discuss the initial measurement results in Section 5.1, Section 5.2 will describe the results of the thermal focused measurements in test phase I and Section 5.3 shows the results of the loaded test in test phase II.

5.1. Initial Measurements

Before doing any actual measurements with the Gusto bearing, trial measurements were performed with the bearing attached to the NI PXIe-4844 Interrogator. During these trial measurements the FBG channels of the bearing were attached to the interrogator as described in Table 5.1. For convenience this channel layout will not change for the remainder of this project.

Table 5.1: Channel number description

Channel Number	Description
0	B1L - 140072
1	B1L - 140078
2	B1R - 140075
3	B1R - 140077

5.1.1. Initial Data

This subsection will describe general observations made on the data produced during the initial measurements. For these graphs only raw data was used. Figure 5.1 shows the reflective spectra of all channels for a single moment in time, measured during the initial measurements. As can be observed in Figure 5.1, all sensors attached to the Gusto bearing show a distinctive peak in the reflective spectra. The peaks and accompanying amplitudes are similar for the different channels. Figure 5.2 shows the reflective spectra of channel 0 only.

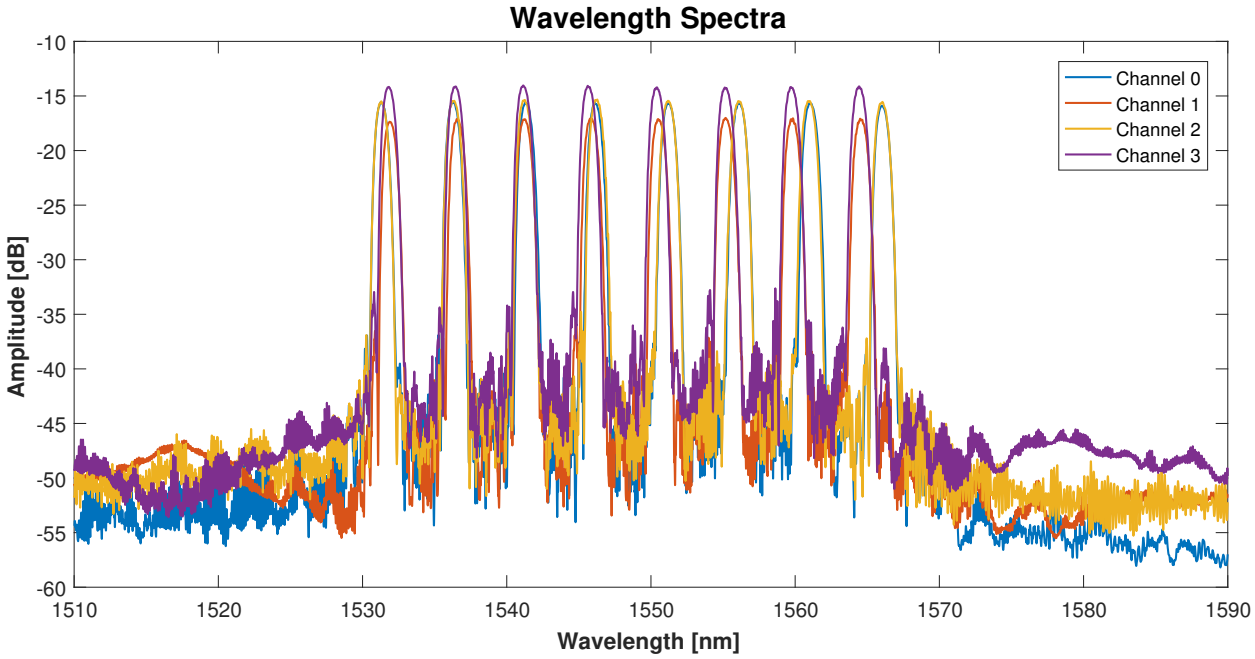

Figure 5.1: Wavelength spectra Gusto Bearing all channels at initial measurements

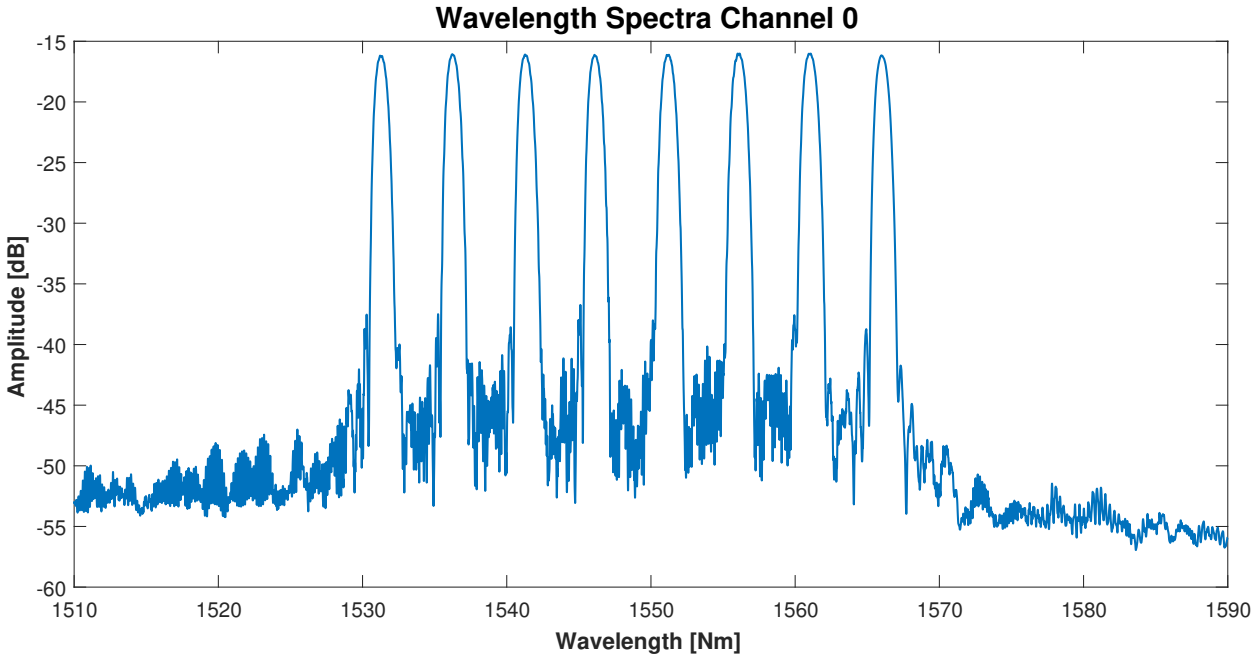

Figure 5.2: Wavelength spectra Gusto Bearing channel 0 at initial measurements

Figure 5.3 shows the reflective spectra of channel 1, the main observation here are the side peaks to the left of the peaks for the first four sensors. The last four sensors (four sensors to the right) show a more symmetrical response/less distinct side peaks. The signal received from channel 1 also seems to contain less noise compared to channel 0, this may be due to contaminated connectors/different quality connector converters (Gusto bearing connectors did not match NI interrogator connectors). Figure 5.3 is however plotted in dB scale, therefore the side peaks are relatively large compared to the main peaks. Figures 5.4 and 5.5 show a closeup of the first peak of channel 1, comparing the dB scale and reflectivity scale. The dashed red line gives the peak location obtained by a centroid peak detection method, this method was explained in Subsection 4.3.3. As can be seen the peak wavelength is slightly

to the right of the maximum reflectivity, this is due to the fact that the slope of the peak on the left side of the peak is steeper compared to the slope to the right of the peak.

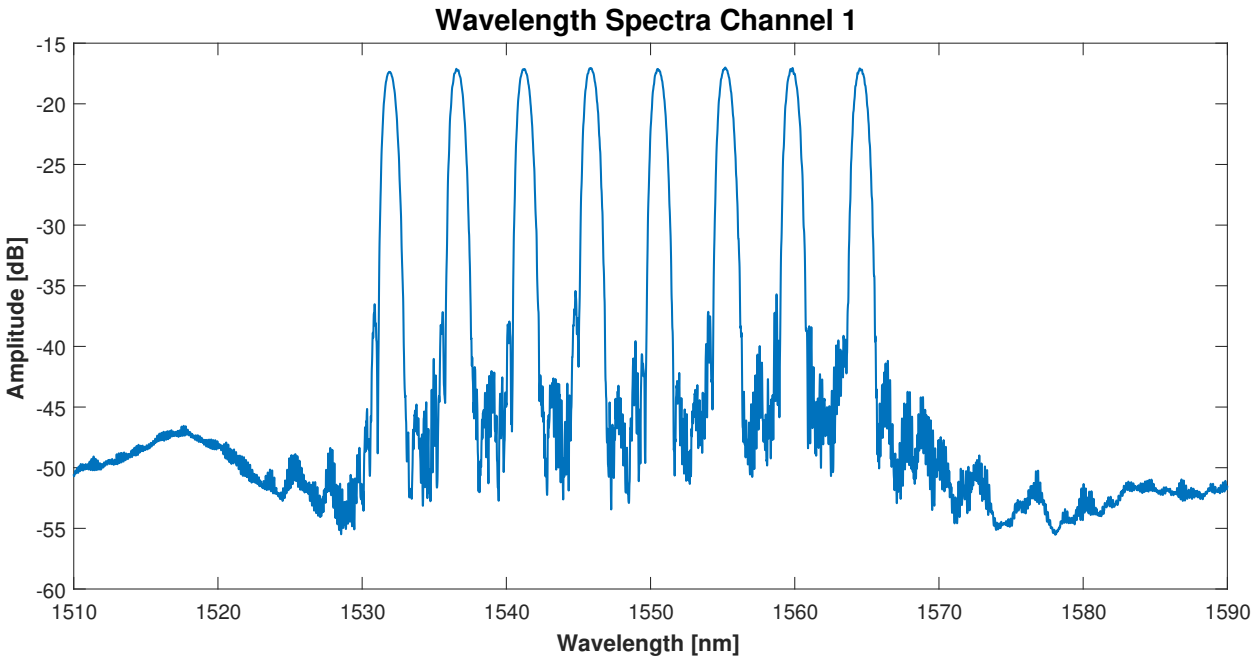

Figure 5.3: Wavelength spectra Gusto Bearing channel 1 at initial measurements

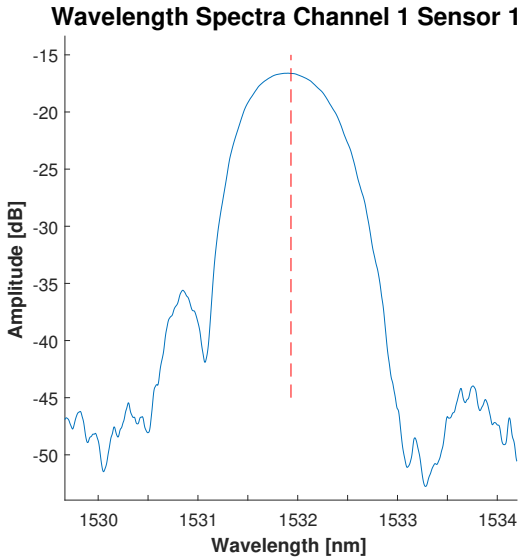

Figure 5.4: Wavelength spectra Gusto bearing channel 1 sensor 1 at initial measurements (Amplitude)

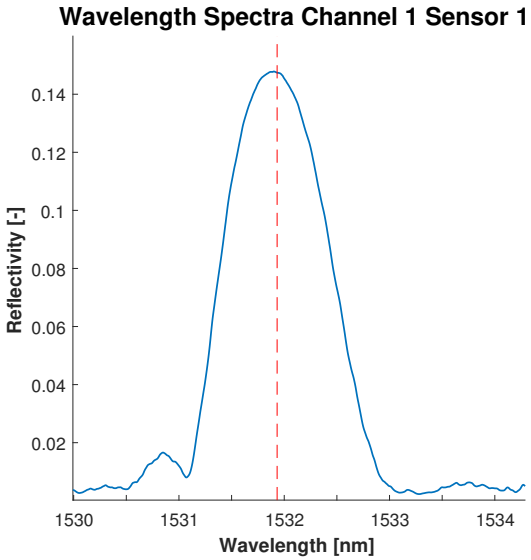

Figure 5.5: Wavelength spectra Gusto bearing channel 1 sensor 1 at initial measurements (Reflectivity)

The Initial data has shown that every channel shows a valid responds in the reflective spectra, all sensors are visible, have a similar amplitude and wavelength spacing. Side peaks are observed to the left of the peak in the reflective spectra, these are however exaggerated in the log scale. When the amplitudes are converted to magnitudes, the side peaks are below the used threshold used in the peak detection algorithm. For the remainder of the project, the side peaks are noted but assumed to be irrelevant and neglected in further processing of the data. It is also shown that the peaks show different slopes left and right of the peak, this becomes clear after the peak detection is done. This may cause different results depending on the peak detection method .

5.2. Test Phase I

In order to increase the reliability of the measurements, the proposed test was performed three times. To verify the temperature during the measurements, two thermocouples were placed on the outer ring of the bearing at the location of the FBG sensors (See Figure 5.6).

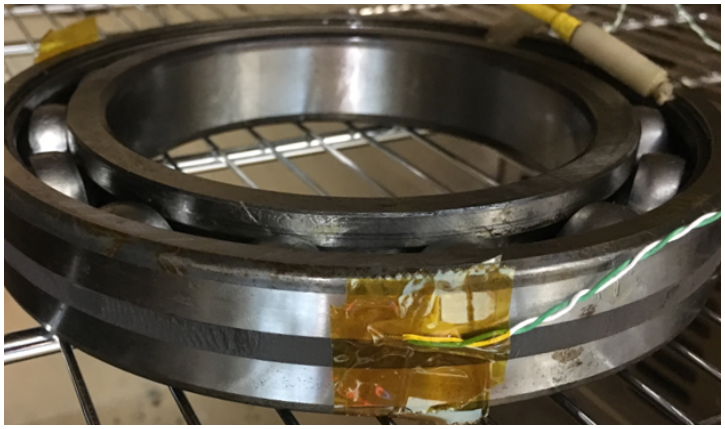

Figure 5.6: Thermocouple attached to the outer ring of the Gusto bearing

During the measurements it was observed that the temperature was not uniform over the bearing. As can be seen in Figures 5.7 and 5.8, the temperature between the two thermocouples differs. A similar observations is made for the first set of measurements. The sensors attached to Channel 0 and 1 did not reach the targeted 100 degrees Celsius. This may be caused by the opening in the side of the oven for guiding the fibers and thermocouple cables out in combination with the air stream generated by the fan in the back of the oven, as can be seen in Figure 5.9. It is also likely that on the side of the bearing the targeted temperature was not reached, the temperature was not uniform over that particular set of FBGs (Channel 0 and 1).

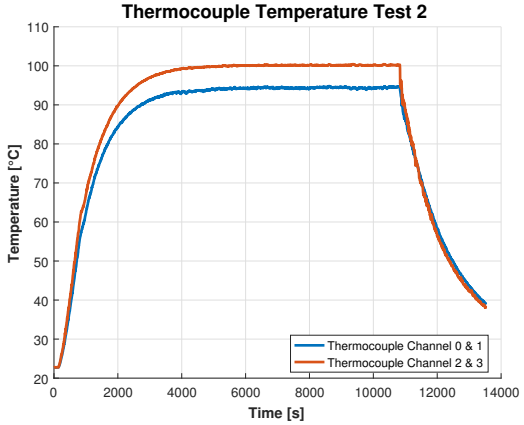

Figure 5.7: Thermocouple temperature output - Test 2

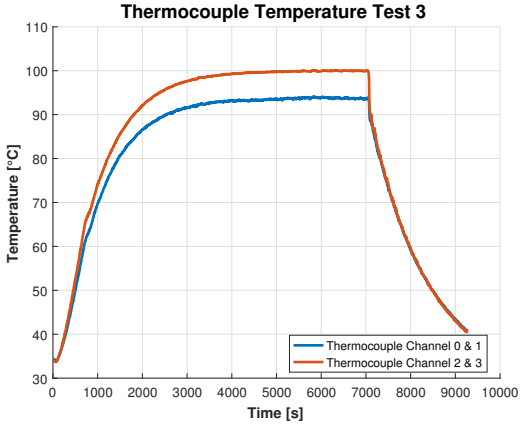

Figure 5.8: Thermocouple temperature output - Test 3

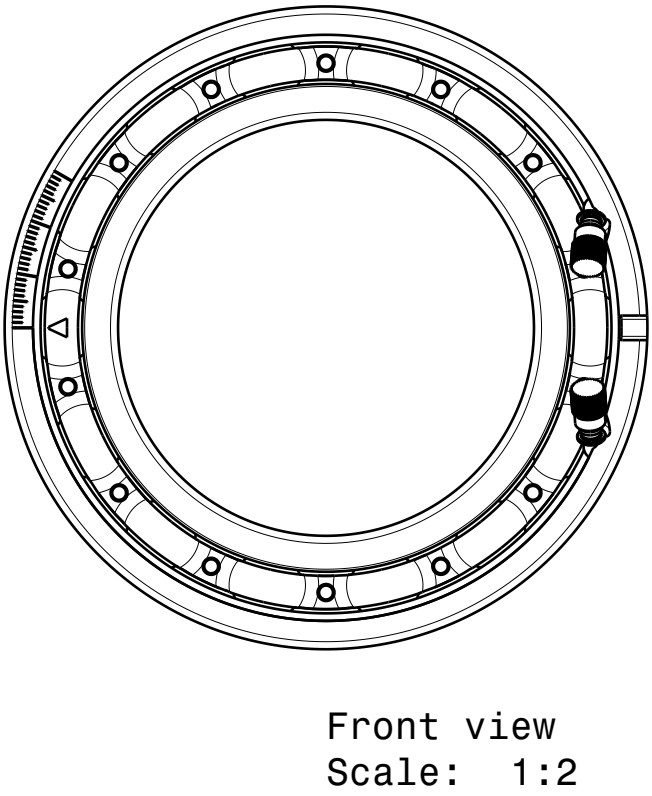

Figure 5.10: Gusto bearing position during Test I

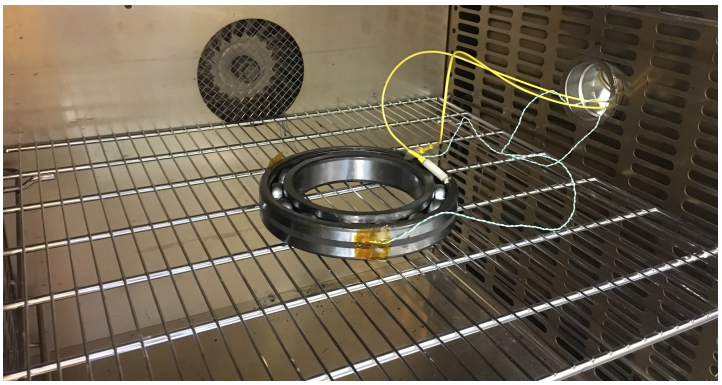

Figure 5.9: Gusto bearing placed in the middle of the Heraeus 0914 oven

Figure 5.10 gives the position of the bearing during the temperature tests. The bearing was not re-positioned or moved during the course of the three measurement runs. Figure 5.11 shows the position of the FBG sensors w.r.t. the rolling elements. In the figure, only two fibers are drawn, in the actual bearing the FBG sensors are divided over four fibers, as described in Section 3.1.2. Figure 5.12 gives a close-up of the contact point of the rolling element closest to the sensors. Due to the temperature change, the refractive index of the FBGs will change and thermal expansion will occur in the fiber. However, for the case of the strain FBGs, the sensors are firmly attached to the steel outer ring of the Gusto bearing. The thermal expansion coefficient of steel (9.5-12.5 $\cdot 10^{-6}$/K) is higher than the thermal expansion coefficient of the glass fiber (0.55 $\cdot 10^{-6}$/K). Therefore, for the strain FBGs, only the steel expansion coefficient and change in refractive index in the fiber are relevant. All strain sensors will experience the expansion of the outer ring due to the temperature change.

Figures 5.13 and 5.14 give the relative peak displacement of the sensor group located at the top of the

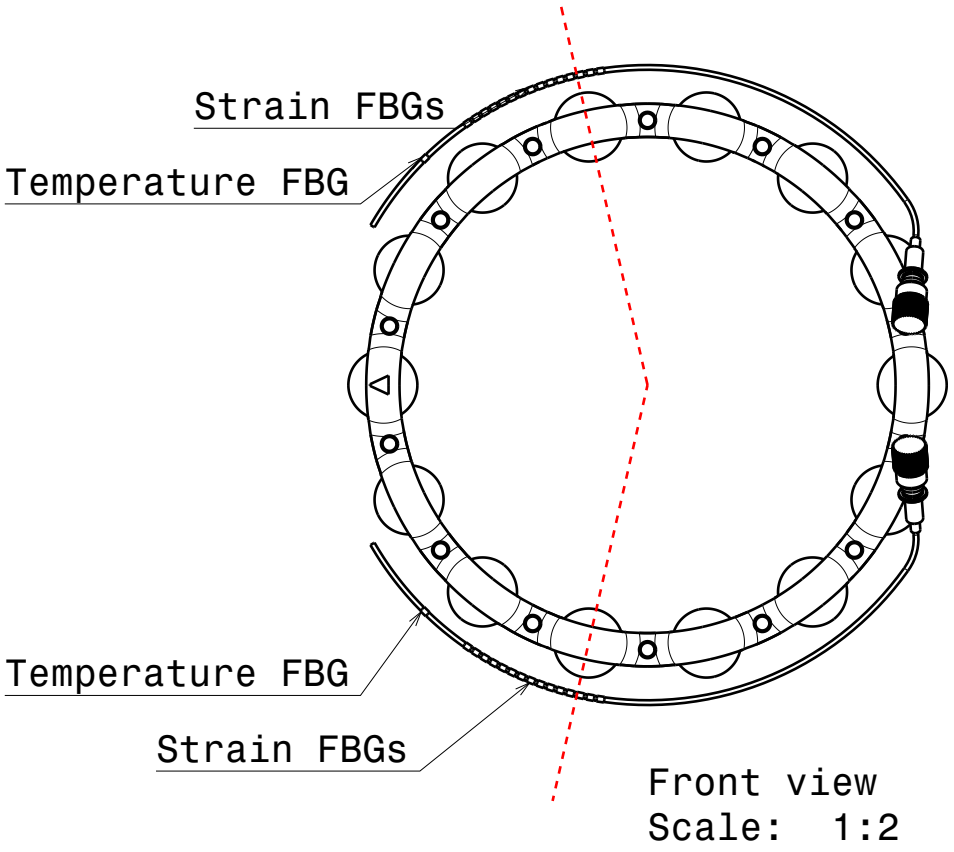

Figure 5.11: Gusto bearing - FBG locations w.r.t. rolling elements (1)

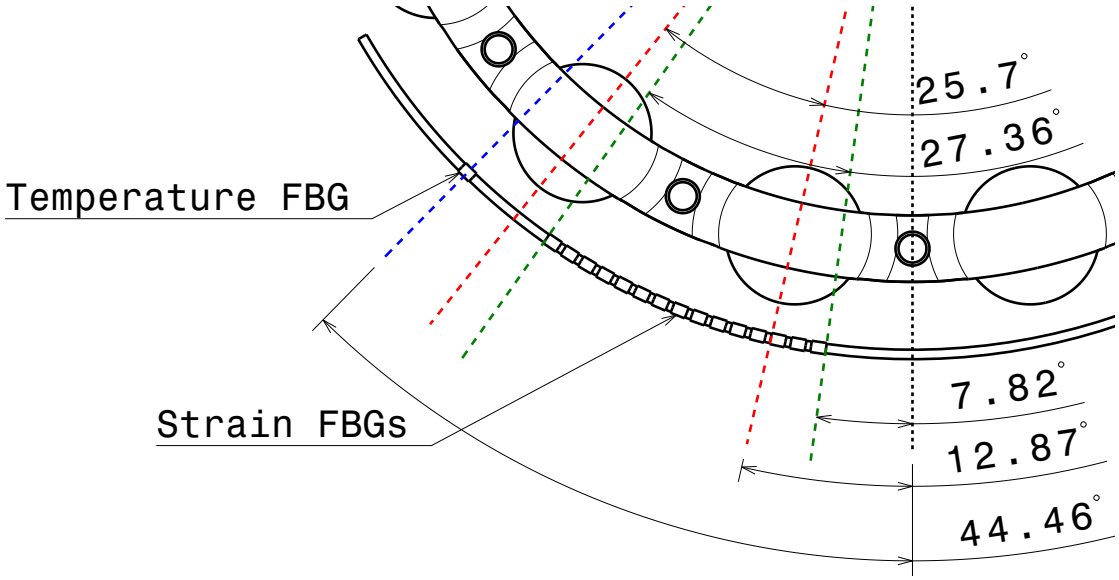

Figure 5.12: Gusto bearing - FBG locations w.r.t. rolling elements (Scale: 1:1) (2)

Gusto bearing (With reference to Figure 5.10), no distinct differences can be observed in from these values. Figures 5.15 and 5.16 give the relative peak displacement of the sensor group located at the bottom of the bearing, here a small increase can be observed for sensors 6 and 7 for both channels. It cannot be said if the difference in relative peak displacement is significant. For this reason the refractive index change is determined in Subsection 5.2.1 and the relative peak displacement are compensated for this change as well as for the thermal expansion of the steel, resulting in a theoretical mechanical strain. This will make it possible to see whether the differences in peak displacement are significant and should be accounted for.

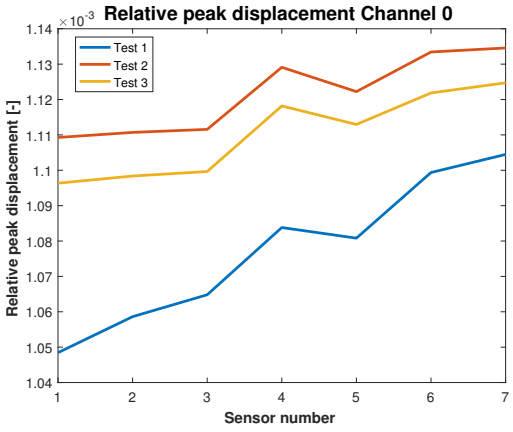

Figure 5.13: Relative peak displacement Channel 0 at 93.6 °C

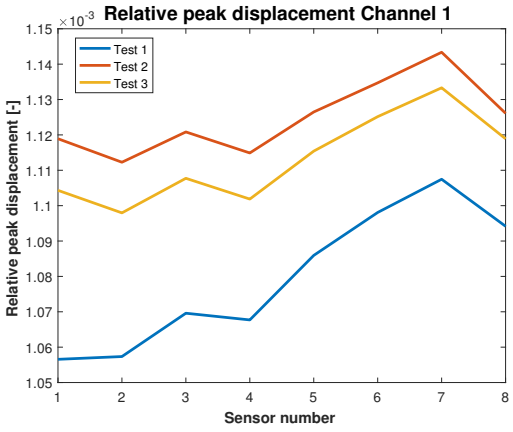

Figure 5.14: Relative peak displacement Channel 1 at 93.6 °C

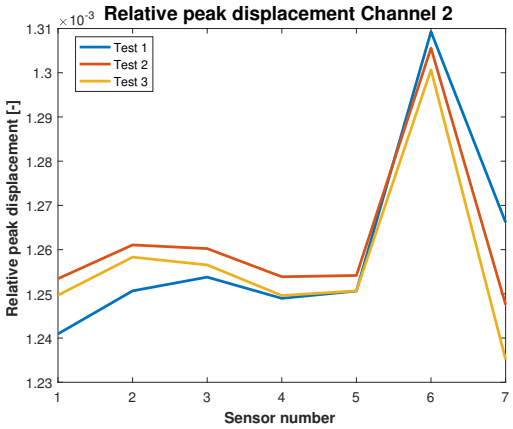

Figure 5.15: Relative peak displacement Channel 2 at 99.9 °C

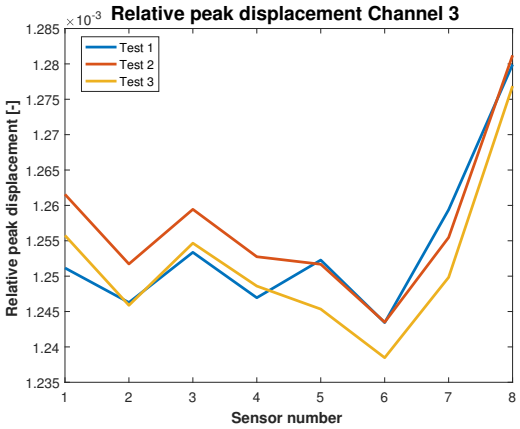

Figure 5.16: Relative peak displacement Channel 3 at 99.9 °C

5.2.1. Theoretical Mechanical Strain

In order to determine whether the differences in relative peak displacement over the sensors is significant, the theoretical mechanical strain on the sensors over the temperature range is calculated. For this calculation, it is assumed all variables are constant over the measured temperature range. For a temperature FBG the relation in Equation 5.1 holds.

$$\frac{\Delta\lambda}{\lambda_B} = (k_g \cdot \alpha_\Lambda + \alpha_n)\Delta T \tag{5.1}$$

With $\Delta\lambda$ the peak displacement in the refractive spectra, λ_B the initial wavelength in the refractive spectra, k_g the gauge factor, α_Λ the thermal expansion coefficient of the glass, α_n the thermo-optic coefficient and ΔT the temperature difference. All variables are known in this equation, except for the thermo-optic coefficient. In order to determine the thermo-optic coefficient, it is assumed that all FBGs

used in the Gusto bearing are of the same type and structure. Furthermore, it is assumed that the temperature FBGs are fixed to the bearing sufficiently far from the bearing, making sure no strain is introduced due to thermal expansion of the host material. This means that the temperature FBGs are only affected by the change in thermo-optic coefficient and the thermal expansion of the fiber itself (glass). The strain FBGs, that are firmly attached to the host material, will be subject to the thermal expansion of the host material as well. The steel outer ring will expand at a higher rate compared to the fiber (glass). Therefore, the expression shown in Equation 5.2 holds for the strain FBGs.

$$\frac{\Delta\lambda}{\lambda_B} = k_g \cdot \epsilon + (k_g \cdot \alpha_{st} + \alpha_n)\Delta T \tag{5.2}$$

With α_{st} the thermal expansion coefficient of steel, ϵ the applied mechanical strain and k_g the gauge factor which is defined as shown in Equation 5.3. Here p_e is the strain-optic coefficient, which is assumed to be 0.22 (assumed constant for every sensor).

$$k_g = 1 - p_e \tag{5.3}$$

Because the temperature range of this test is small, the thermo-optic coefficient is assumed to be constant over the temperature range. Because the thermocouples were attached to the surface of the outer ring, temperature differences may be present between the thermocouple and FBGs. Therefore, in order to calculate the thermo-optic coefficient, the settled maximum temperature was taken. For this state it is assumed that the bearing, FBGs and thermocouple have the same temperature, hence Equation 5.1 can be rewritten to the expression shown in Equation 5.4, valid for the temperature FBGs.

$$\alpha_n = \frac{\Delta\lambda}{\lambda_B} - k_g \cdot \alpha_\Lambda \tag{5.4}$$

The initial wavelength of the sensors were obtained from the second test at 22.73 °C and 22.78 °C for channel 0 and 2 respectively. This time point was chosen as the bearing was kept overnight in the oven between test 1 and 2, the bearing temperature was settled at ambient temperature at this point in time. The average of the refractive index change constant over 120 measurements (10 min) was taken once the bearing was settled at the maximum temperature. The results are shown in Table 5.2.

Table 5.2: Thermo-optic coefficient Temperature FBGs

	Chanel 0 &1	Channel 2 & 3
Test 1	6.2880E-06	6.1714E-06
Test 2	6.2485E-06	6.1749E-06
Test 3	6.2545E-06	6.1755E-06
Average	6.2637E-06	6.1739E-06

Now the expression in Equation 5.1 can be rewritten to the expression shown in Equation 5.5, solving for the temperature change as a function of the relative peak displacement.

$$\Delta T = \frac{1}{(k_g \cdot \alpha_\Lambda + \alpha_n)} \cdot \frac{\Delta\lambda}{\lambda_B \Delta T} \tag{5.5}$$

Substituting the found values for the thermo-optic coefficients and adding the initial temperature, gives the temperature measured by the temperature FBGs. In order to verify this, the temperature FBG measurements are plotted over the thermocouple measurements in Figure 5.17 and 5.18. The temperatures of the thermocouples are higher during warm-up of the bearing compared to the FBG temperatures, this is expected as the thermocouples where attached to the surface of the bearing, heating up faster compared to the embedded FBGs.

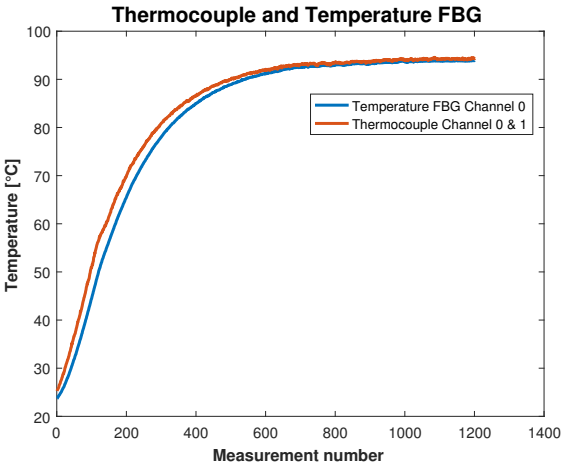

Figure 5.17: Thermocouple and Temperature FBG Channel 0 (Test 2)

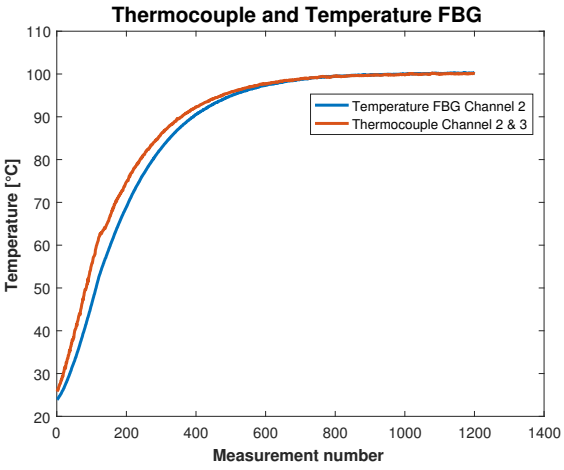

Figure 5.18: Thermocouple and Temperature FBG Channel 2 (Test 2)

It is assumed that all FBGs attached to the Gusto bearing are similar, therefore the thermo-optic coefficient is assumed to be the same for the accompanying sensor group. The strain sensors are also affected by the thermal expansion of the steel, as can be seen in Equation 5.2. The thermal expansion of the steel is the same for every sensor and a reasonable estimate on the thermal expansion coefficient of steel can be found in literature [1]. The thermal expansion for steel was found to be in the range of 9.5 to 12.6$\cdot 10^{-6}$ /K. Now Equation 5.2 can be rearranged to solve for ϵ, giving the expression shown in Equation 5.6.

$$\epsilon = \frac{\Delta\lambda}{\lambda_B \cdot k_g} - \left(\alpha_{st} + \frac{\alpha_n}{k_g}\right)\Delta T \tag{5.6}$$

As there is no mechanical strain applied to the bearing during this test, the value for ϵ should theoretically be zero. This will also depend on the exact value of the thermal expansion coefficient of the used steel in the bearing and the assumed value for the gauge factor. Here the gauge factor is assumed to be correct and the thermal expansion coefficient of the steel is varied in order to obtain a zero mechanical strain state for the entire temperature range in the first test. Figure 5.19 shows the mechanical strain as a function of temperature for a thermal expansion coefficient of steel of 9.5 $\cdot 10^{-6}$ /K. As can be seen the mechanical strain varies linearly and increases with increasing temperature change. It is expected that some strain is lost/dissipated in the bonding material between the FBGs and the steel, so a slightly negative mechanical strain is more plausible. Figure 5.20 shows a similar graph as shown in Figure 5.19 but, here a thermal expansion coefficient of steel of 12.5$\cdot 10^{-6}$ /K was used. As can be seen in the figure, the mechanical strain with increasing temperature is very small, as is expected. Therefore, a thermal expansion coefficient of 12.5$\cdot 10^{-6}$ /K will be used in further calculations.

[1] `http://www.matweb.com/search/datasheet.aspx?bassnum=MS0001&ckck=1` - Accessed 14/08/2017

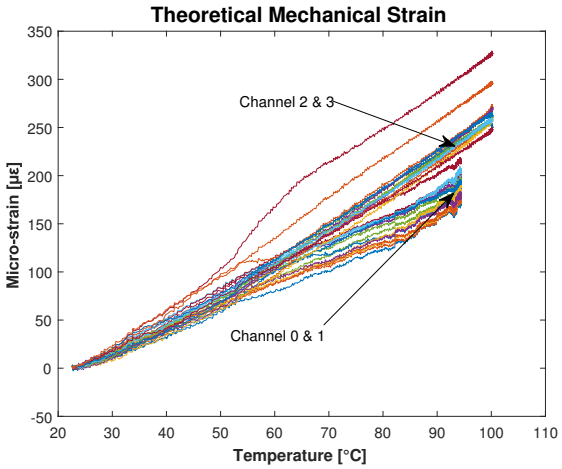

Figure 5.19: Theoretical mechanical strain (α_{st} = 9.5 $\cdot 10^{-6}$ /K) Test 2

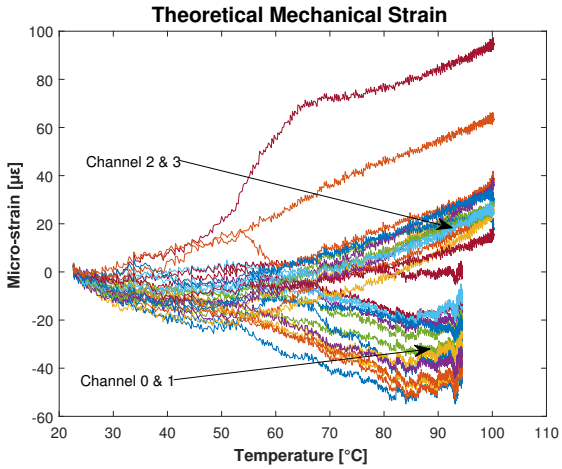

Figure 5.20: Theoretical mechanical strain (α_{st} = 12.5 $\cdot 10^{-6}$ /K) Test 2

Figure 5.21 again gives the mechanical strain with increasing temperature for a thermal expansion coefficient of 12.5$\cdot 10^{-6}$ /K but, here the results of Test 3 are shown. As can be seen the start temperature of Test 3 was higher than Test 2 but, the theoretical strain values for the measured temperatures match the values observed in Test 2. The slight offset observed in Test 3 at the start of the measurements could be explained by non-uniform cooling of the bearing between Test 2 and 3, obtaining an incorrect temperature reading from the temperature FBG w.r.t. the strain FBGs. In Figure 5.19, 5.20 and 5.21, one can observe that the FBGs placed on the same fiber and the FBGs placed on the fiber adjacent to the that fiber, have similar theoretical mechanical strain levels for different temperatures. Hence, the FBGs on the top side of the bearing are performing slightly different compared to the FBGs on the lower side of the bearing.

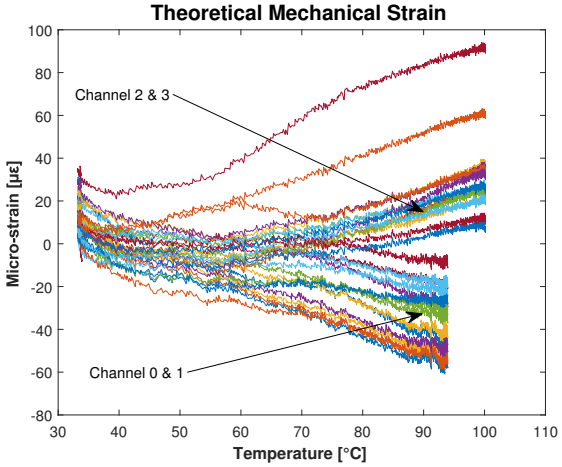

Figure 5.21: Theoretical mechanical strain (α_{st} = 12.5 $\cdot 10^{-6}$ /K) Test 3

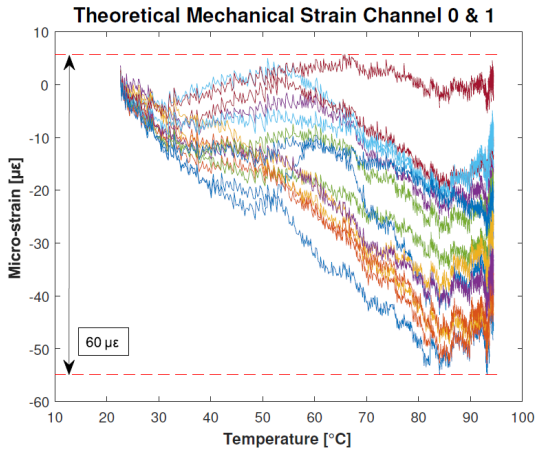

Figure 5.22: Theoretical mechanical strain Channel 0 & 1 (Test 2)

Figure 5.22 shows the theoretical mechanical strain of channel 0 and 1, using the 12.5 $\cdot 10^{-6}$ /K value for the thermal expansion coefficient of steel. The difference in mechanical strain from start to end temperature over the range of sensors in this group is 60.63 micro-strain. As can be seen, the different sensors are quite dispersed over the graph, this may be caused by the fact that this sensor group did not reach the targeted maximum temperature of the oven. Therefore the temperature measured by the temperature FBG may not be correct for every sensor in this group. Figure 5.23 shows the theoretical mechanical strain of channel 2 and 3, this sensor group did reach the targeted temperature of the oven. As can be seen, the different sensors in the group are behaving more similar over the temperature range, with the exception of the three labeled sensors. The difference in mechanical strain from start to end temperature over the range of sensors is 120.26 micro-strain. However, if the two sensors that

are clearly behaving differently, are excluded, the change is similar to the change observed in the first group, namely 64.59 micro-strain.

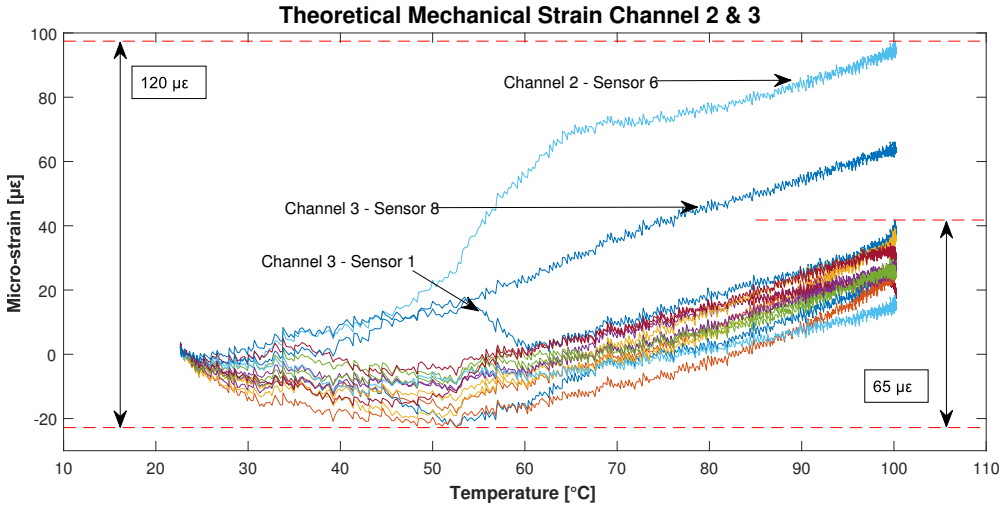

Figure 5.23: Theoretical mechanical strain Channel 2 & 3 (Test 2)

The behavior of sensor 6 on channel 2 and sensors 1 and 8 on channel 3 is different compared to the rest of the sensors on that side of the bearing. Similar observations can be made for Test 3, as can be seen in Figure 5.24. During the prototype testing, the bearing was tested in the temperature range of 40 to 60 °C. Based on Figure 5.23, this would mean the before mentioned sensors would display a slight strain offset compared to the other sensors. However, here temperature was the only variable, further testing is required in order to see whether these sensors also react different to mechanical strain, this is done in test phase II.

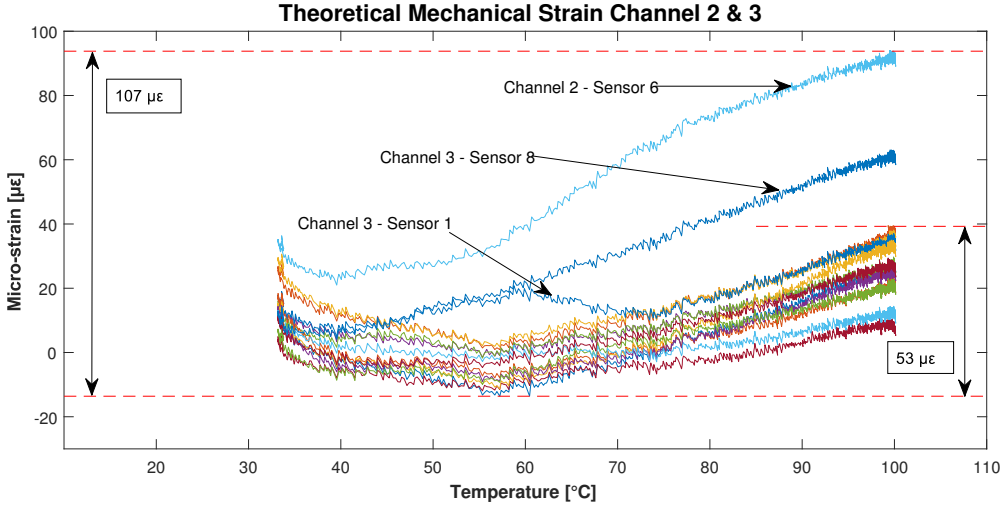

Figure 5.24: Theoretical mechanical strain Channel 2 & 3 (Test 3)

5.2.2. Peak Shapes

In order to compare the peak shapes at the initial temperature and maximum temperature, the peaks in the reflective spectra are superimposed. This is done by overlaying the found peaks by the geometric center method over each other. This is only shown for a selection of sensors on Channel 2 and 3, similar results were observed for Channels 0 and 1 and other sensors on Channels 2 and 3. A selection of four sensors is shown in this subsection, Figures 5.25 and 5.29 show the superimposed peaks of sensors that showed similar theoretical mechanical strain, the sensors shown in the lower half of Figures 5.23 and 5.24. Figures 5.27 and 5.31 show the superimposed peaks of sensors that showed different behavior in the theoretical mechanical strain, see the highlighted sensors in Figures 5.23 and

5.24.

What can be observed is that the general shape of the peaks do not change. No distinct asymmetric behavior or peak splitting phenomena can be observed between the two temperature cases. The sensors marked in Figure 5.23 do not show any differences in the reflective spectra in comparison to the normal behaving sensors. From the initial observation, one can conclude that the strain distribution over the sensors stays constant between the two temperature cases. In order to verify this, the FWHMs of all sensors are compared for the two temperature cases in Subsection 5.2.3. One can also see that for some sensors, and especially when the sensors are at maximum temperature, spectra waviness occurs. The NI interrogator is able to detect this, but it is very likely the resolution of the SBI interrogator is not able to detect this. Depending on the place of the peak in the resolution steps of the SBI interrogator, the waviness could lead to differences in peak shapes and hence peak locations. Due to the waviness and the lower resolution of the SBI interrogator, not all peak readouts are consistent, due to movement of the peaks over the wavelength resolution steps of the SBI interrogator.

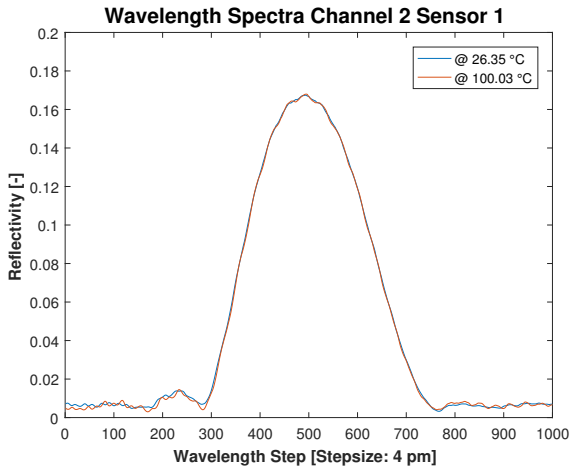

Figure 5.25: Superimposed Peaks Channel 2 Sensor 1 Test 2

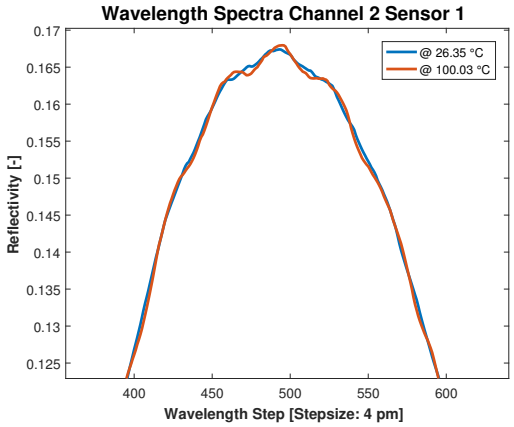

Figure 5.26: Superimposed Peaks Channel 2 Sensor 1 Test 2 enlarged

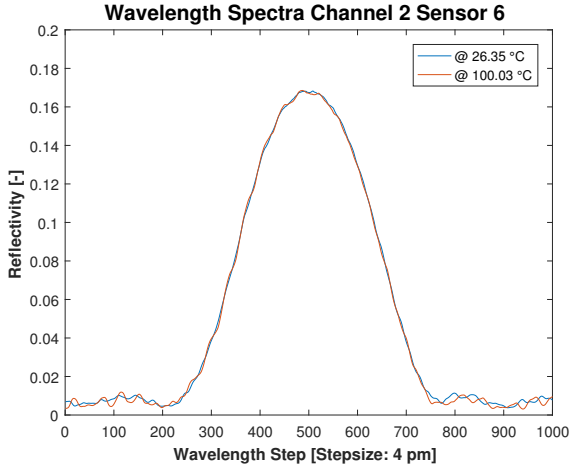

Figure 5.27: Superimposed Peaks Channel 2 Sensor 6 Test 2

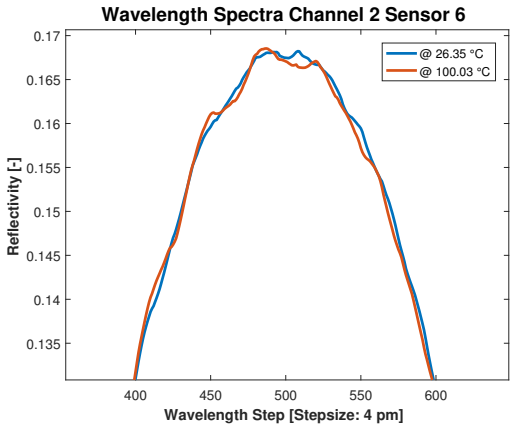

Figure 5.28: Superimposed Peaks Channel 2 Sensor 6 Test 2 enlarged

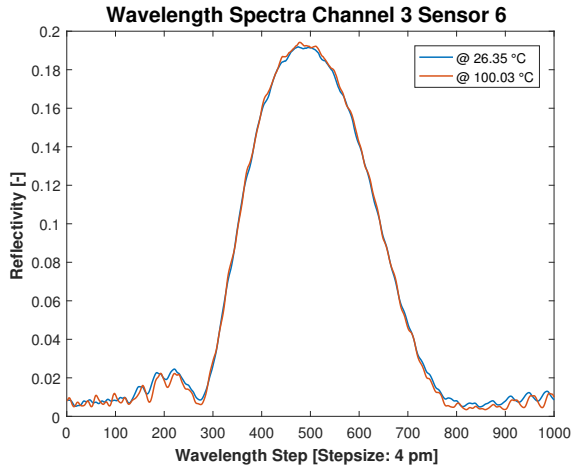

Figure 5.29: Superimposed Peaks Channel 3 Sensor 6 Test 2

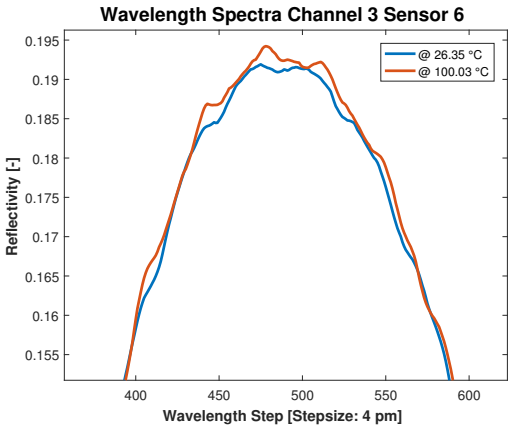

Figure 5.30: Superimposed Peaks Channel 3 Sensor 6 Test 2 enlarged

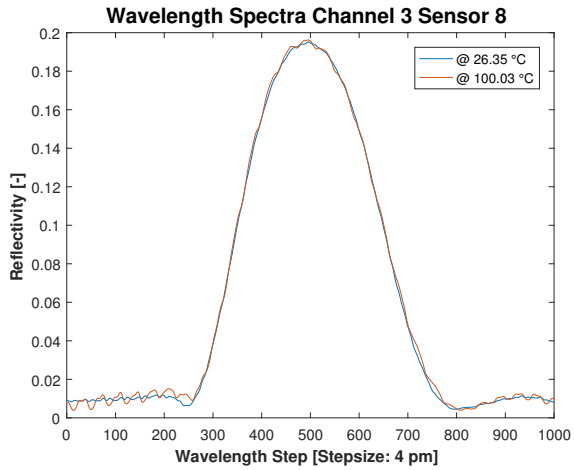

Figure 5.31: Superimposed Peaks Channel 3 Sensor 8 Test 2

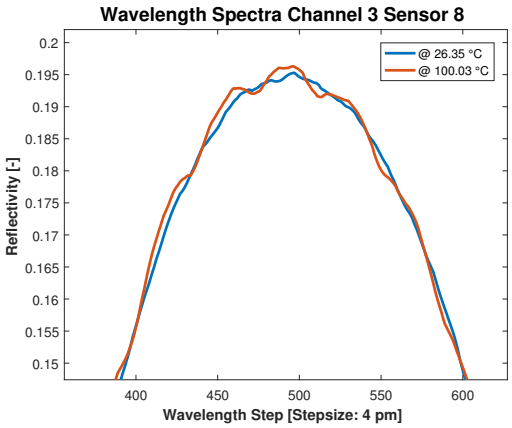

Figure 5.32: Superimposed Peaks Channel 3 Sensor 8 Test 2 enlarged

5.2.3. FWHM and Temperature

This subsection gives the FWHM of every sensor at the start of the measurements, at approximately 38 °C in Table 5.3 and at the settled maximum temperate in Table 5.4. The reason for choosing 38 °C as start temperature is due to the fact that the Test 3 started at this temperature (lower temperature values are only available for Test 1 and 2). The relevant Matlab code for generating the FWHM values can be found in Appendix B, in Listing B.4. As can be observed, the changes in FWHM due to the temperature change are very small, in the order of picometers, which is in this case smaller than 0.5 %. The differences of the FWHM between sensors on the same fiber are larger, in some cases even up to 0.1 nm, which is the resolution step of the interrogator used in the prototype test.

Table 5.3: FWHM at start measurements

FWHM [nm]									
Channel #	Test #	Temp. [°C]	Sensor #							
			1	2	3	4	5	6	7	8
0	1	38.78	1.116	1.136	1.148	1.124	1.184	1.208	1.208	1.180
	2	38.79	1.120	1.140	1.156	1.132	1.188	1.212	1.212	1.180
	3	38.85	1.124	1.140	1.164	1.140	1.200	1.212	1.216	1.176
	Average	38.81	1.120	1.139	1.156	1.132	1.191	1.211	1.212	1.179
1	1	38.78	1.136	1.140	1.168	1.176	1.176	1.228	1.156	1.208
	2	38.79	1.136	1.144	1.164	1.176	1.180	1.216	1.168	1.228
	3	38.85	1.144	1.144	1.168	1.168	1.172	1.232	1.184	1.236
	Average	38.81	1.139	1.143	1.167	1.173	1.176	1.225	1.169	1.224
2	1	38.79	1.104	1.144	1.132	1.144	1.184	1.188	1.208	1.196
	2	39.23	1.104	1.144	1.128	1.140	1.192	1.196	1.208	1.200
	3	38.65	1.112	1.148	1.132	1.152	1.192	1.200	1.208	1.200
	Average	38.89	1.107	1.145	1.131	1.145	1.189	1.195	1.208	1.199
3	1	38.79	1.132	1.164	1.168	1.148	1.168	1.184	1.176	1.224
	2	39.23	1.132	1.164	1.172	1.160	1.172	1.188	1.180	1.212
	3	38.65	1.132	1.160	1.176	1.168	1.168	1.188	1.188	1.212
	Average	38.89	1.132	1.163	1.172	1.159	1.169	1.187	1.181	1.216

Table 5.4: FWHM at maximum temperature

FWHM [nm]									
Channel #	Test #	Temp. [°C]	Sensor #							
			1	2	3	4	5	6	7	8
0	1	92.63	1.116	1.140	1.148	1.124	1.184	1.216	1.208	1.176
	2	94.24	1.116	1.140	1.144	1.124	1.184	1.216	1.204	1.176
	3	93.96	1.116	1.136	1.148	1.124	1.184	1.216	1.208	1.176
	Average	93.61	1.116	1.139	1.147	1.124	1.184	1.216	1.207	1.176
1	1	92.63	1.132	1.136	1.160	1.172	1.172	1.228	1.160	1.208
	2	94.24	1.132	1.136	1.164	1.172	1.176	1.224	1.160	1.212
	3	93.96	1.128	1.132	1.160	1.168	1.168	1.224	1.160	1.208
	Average	93.61	1.131	1.135	1.161	1.171	1.172	1.225	1.160	1.209
2	1	99.83	1.104	1.148	1.128	1.136	1.180	1.188	1.208	1.196
	2	100.03	1.104	1.140	1.128	1.136	1.180	1.180	1.196	1.200
	3	99.88	1.104	1.144	1.132	1.132	1.176	1.184	1.196	1.192
	Average	99.91	1.104	1.144	1.129	1.135	1.179	1.184	1.200	1.196
3	1	99.83	1.132	1.160	1.160	1.152	1.168	1.180	1.172	1.224
	2	100.03	1.128	1.160	1.160	1.152	1.168	1.180	1.172	1.224
	3	99.88	1.124	1.160	1.160	1.156	1.164	1.180	1.172	1.220
	Average	99.91	1.128	1.160	1.160	1.153	1.167	1.180	1.172	1.223

5.3. Test Phase II

The test performed described in this section was executed at SKF Business and Technology Park in Nieuwegein. The load is applied to the shaft by the metal blocks, evenly loading the shaft and hence the bearing. For this test phase, the values found in Test phase I for the thermo-optic coefficient of the fibers and the thermal expansion coefficient of the steel are used. Furthermore, it is assumed that changes in temperature during the test were small and are therefore neglected.

Figure 5.33 shows the load profile that was used during the measurements. The exact applied load was not a top priority therefore, no effort was made to generate exact load steps without overshoot for this test. In order to load different sensors, the shaft was rotated after every load cycle. This way the rolling element was measured in different positions w.r.t. the sensors. The highlighted values in the tables in Appendix E show the rolling element positions over the sensors for every measurement. In order to measure both sensor groups, the outer ring of the bearing was rotated 180 degrees. This way the applied load was directed towards the opposite sensor group.

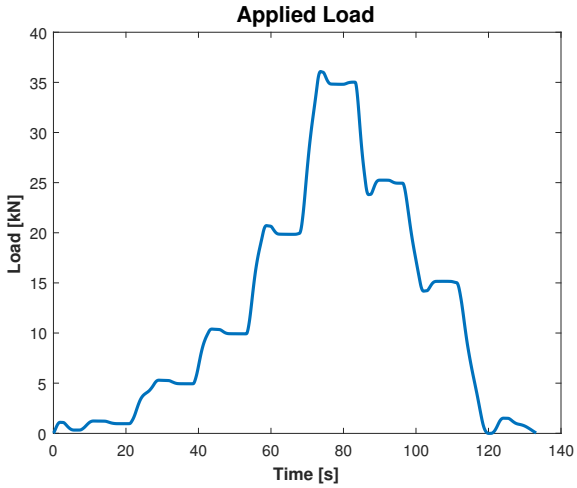

Figure 5.33: Applied load by Instron during Test Phase II (x: time of the test, y: applied load in kN as measured by the Instron load cell)

Before starting the measurements, it was checked whether the assumption, the sensor with the lowest Bragg wavelength is located closest to the connector, was correct. This was done by rotating the shaft in clockwise direction with a small load applied and see which sensors gave a strain reading for the rolling element passing. For this the Gusto bearing was placed in the position shown in Figure 5.10 with a small load applied downward.

For this assumption to be correct, the sensors on Channel 0 and 1 should show, for a rolling element passing, sensor readouts for the sensors with the highest Bragg wavelength to the sensors with the lowest Bragg wavelength. For Channel 2 and 3 an opposite directions should be observed. In order to show the results, sensor readouts from actual measurements are shown for known rolling element positions. Figures 5.34 and 5.35 show the strain distribution of different rolling element positions for Channel 0 & 1 and Channel 2 & 3, respectively. The position changes are in clockwise direction for both graphs, the applied load was 35 kN. As can be seen, the assumption made earlier is indeed correct. Numbering the sensors from 1 to 16, starting with the sensor closest to the connector, matches the numbering proposed earlier.

In order to obtain a complete overview of the numbering used so far, see Figure 5.36. The sensors on Channel 0 & 1 and Channel 2 & 3 form a group of sensors, each containing 15 strain FBGs and 1 temperature FBG. From this point, the sensors will be addressed by group and sensor number in that group (for a full overview of sensor numbering in this document, see Table C.1 in Appendix C).

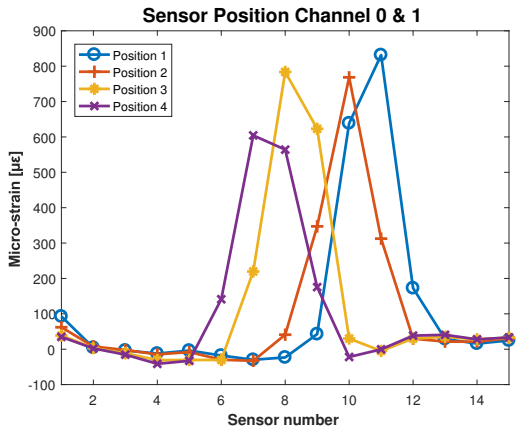

Figure 5.34: Sensor positions Channel CW rotation 0 & 1/Group 1 (x: strain sensor number from connector to end, y: measured strain per sensor in micro-strain)

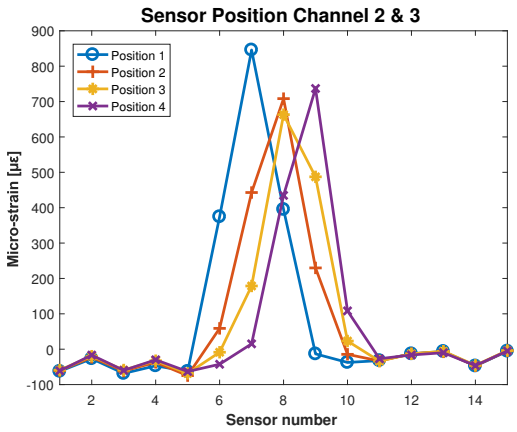

Figure 5.35: Sensor positions CW rotation Channel 2 & 3/Group 2 (x: strain sensor number from connector to end, y: measured strain per sensor in micro-strain)

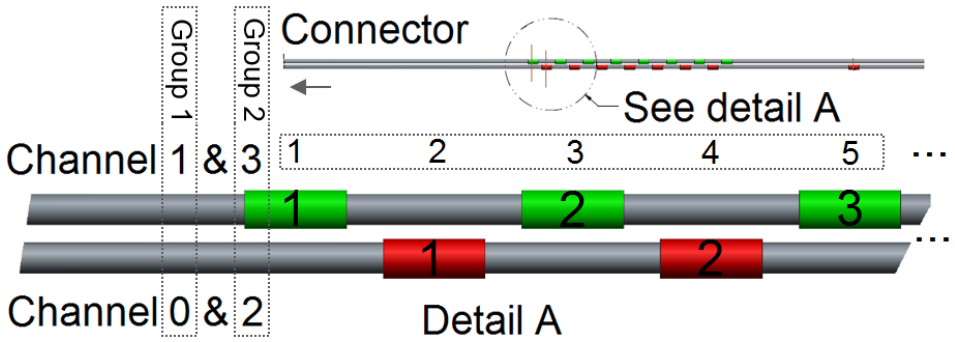

Figure 5.36: Sensor numbering - Final (Numbers in dashed box belong to Group 1 & 2 and accompanying sensors (green & red))

Figures 5.37 and 5.38 give the maximum strain for different rolling element positions for group 1 and 2, respectively. As can be seen in the figures, the measured strain by the FBGs matches the pattern of the applied load shown in Figure 5.33. The strain values are also similar to the strain values observed by SKF in the prototype testing. As was described in Subsection 4.2.3 the FWHM of the reflective spectra is expected to widen if a non-uniform strain is applied over the sensor, this is analyzed in Subsection 5.3.1.

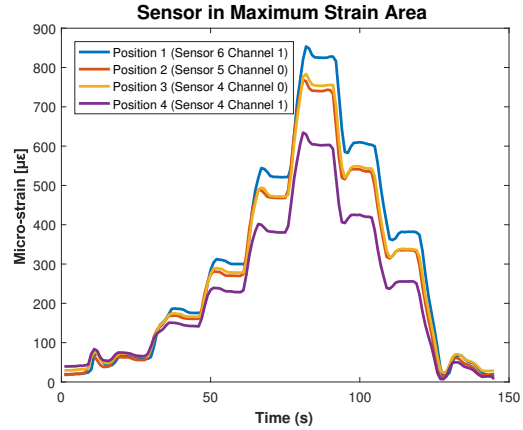

Figure 5.37: Sensors in maximum strain area Channel 0 & 1/Group 1 (x: time of the test, y: measured strain in micro-strain)

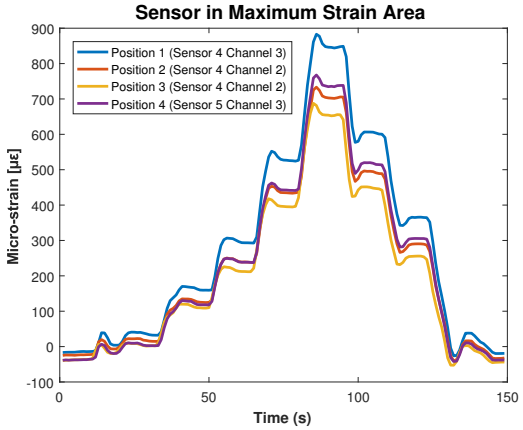

Figure 5.38: Sensors in maximum strain area Channel 2 & 3/Group 2 (x: time of the test, y: measured strain in micro-strain)

Before analyzing the FWHM in non-uniform strain areas, the strain distribution over the sensors was estimated. This was done in order to compare the results to the prototype test results, here differences between sensors were observed near the strain peaks. As this analysis will make use of the strain distribution with inputs from all sensors, one should see a clear dispersion of the results near the strain peaks. Also order to generate the strain distribution of a single rolling element with a certain confidence, different rolling element positions were used. Inputs are similar to the ones shown in Figures 5.34 and 5.35.

For the generating this profile, the peak strain plus five adjacent sensors on either sides for every rolling element position were taken as input. As expected, not all rolling element positions give the same peak strain, as the true strain peak may be in between two sensors. Therefore, all peaks are centered around 5.44 mm, this value was chosen as in preliminary fittings, five sensors per position were used, 5.44 mm being the middle of the third sensor. Finding the strain peaks was done by using the same method as finding the peaks in the reflective spectra, described in Subsection 4.3.3 (here I_i was replaced by the measured strain and $x_1 = 0$ for the first sensor in the particular subset). Measurements with the rolling element at an edge of the sensor group were not taken into account for generating the strain distribution estimate. Figure 5.39 shows the fitted strain distribution of Group 2 at 35 kN. Every black dot represents the middle of a FBG sensor, the sensors have a spacing of 2.72 mm. For this a Fourier fit with five terms was used, the full model can be found in Appendix D.

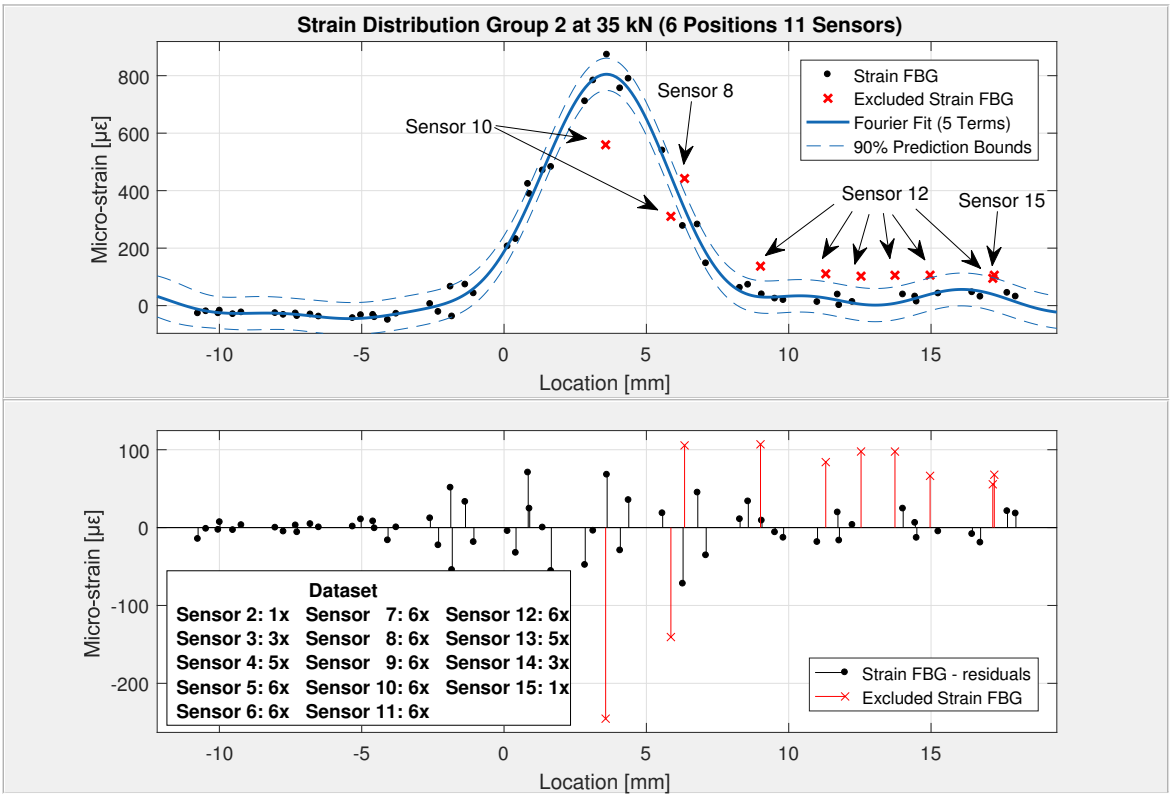

Figure 5.39: Fourier Fit with 5 terms for 6 rolling element positions and 11 sensors per position - Group 2 35kN

Sensor 12 and 15 in Figure 5.39 were excluded from the fit, as these sensor showed a clear offset. This was expected from Test Phase I, where Channel 2 - Sensor 6 and Channel 3 - Sensor 8 showed a different behavior to temperature, shown in Figure 5.23 and 5.24. The other excluded measurements were readouts from sensors 10 and 8, that showed for that particular measurement an offset to the expected strain. The origin of these errors were not found in the given time frame, but were given as suggestion for future research in Section 6.5. The fitted measurement data does not show the negatives strain levels near the peak or the dispersion near the strain peaks, as was observed by SKF. Figure 5.40 shows the strain pattern (left) of a measurement performed by SKF with the Smartscan SBI interrogator. The strain levels shown were observed for a static measurement (bearing was not

rotating) with a force of 15 kN applied (right), the negative strain increases (becomes more negative) with increasing applied force.

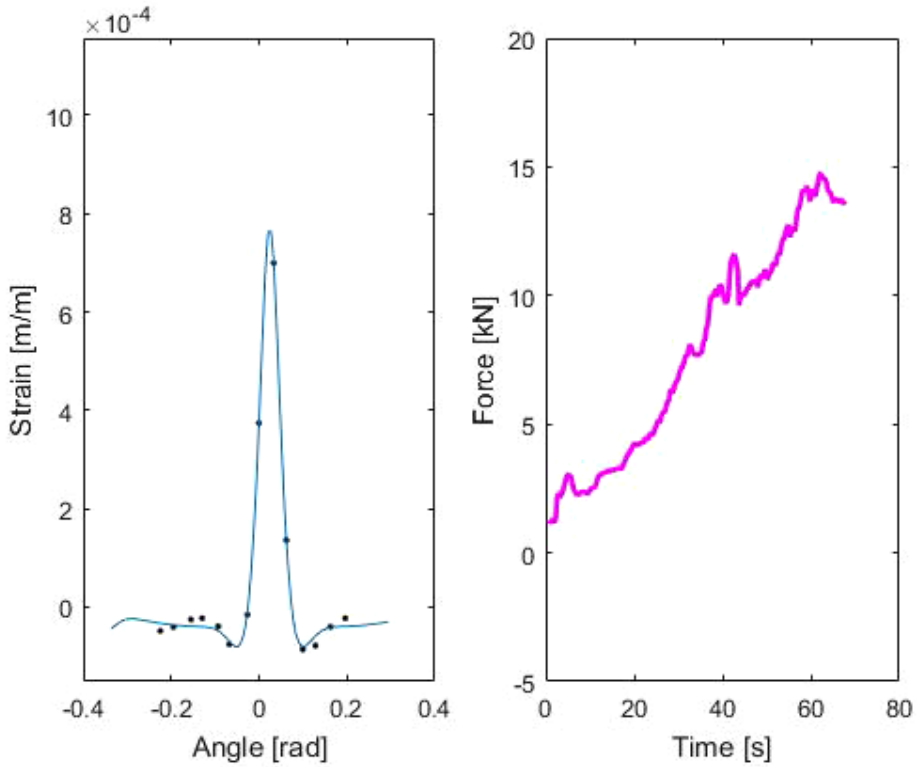

Figure 5.40: Gusto prototype test data using SBI interrogator (left: fitted strain distribution over the sensors at last measured time, right: applied load over time) (1/2)

The strain distribution profile in Figure 5.39 was however generated with measurements from different sensors in that group. In the problem statement in Section 3.2, describing the observed differences in the measurement data, the strain profiles were created with measurements from single sensors over time. This was shown in Figure 3.11, one can observe in the figure that not every sensor shows the negative strain near the strain peak. Therefore, the strain patterns per rolling element position are assessed at the maximum load of 35 kN, note that these profiles are based on a single measurement in time. Two examples are given in Figures 5.41 and 5.42. What can be observed is that in position 2, the sensor located at around -3 mm (Sensor 5 Group 2) shows a similar behavior in comparison to the sensors shown near the strain peak in Figure 5.40 however, the behavior is less distinct. Nonetheless, this particular position could be interesting, as can be seen in Figure 5.43, not all measurements performed by SKF with the SBI interrogator show the distinct negative strains near the strain peaks and the shown distribution observed by SKF is very similar to the one shown in Figure 5.42.

Regardless whether the negative strain near the peak is present in the strain distribution or not, the sensors in the area near the strain peak are subjected to a highly non-uniform strain. The sensor length is 2 mm, a sensor at the edge of the strain peak will therefore be subjected to the steep strain increase of the strain peak as well as the low (constant) strain in the proximity of the peak. This may result in a change of FHWM, this is discussed in Section 5.3.1

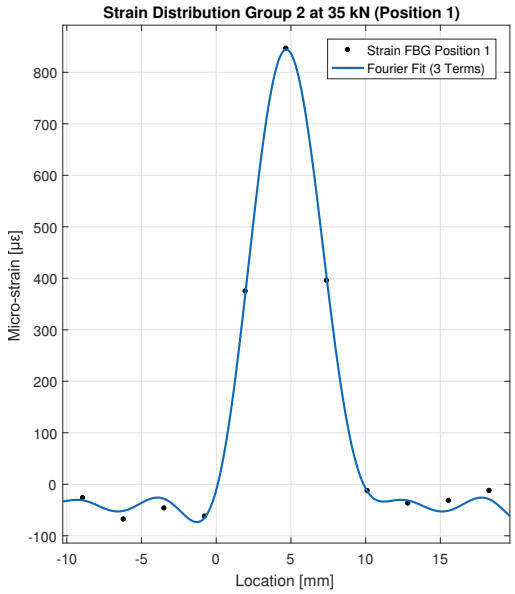

Figure 5.41: Fourier Fit with 3 terms using NI interrogator - Position 1 Group 2 35kN

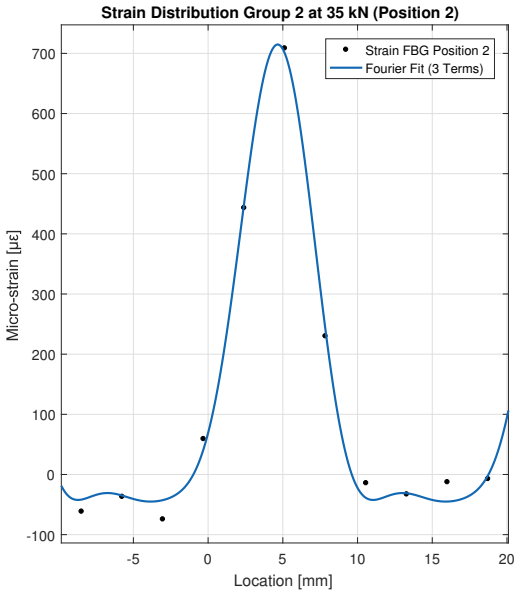

Figure 5.42: Fourier Fit with 3 terms using NI interrogator - Position 2 Group 2 35kN

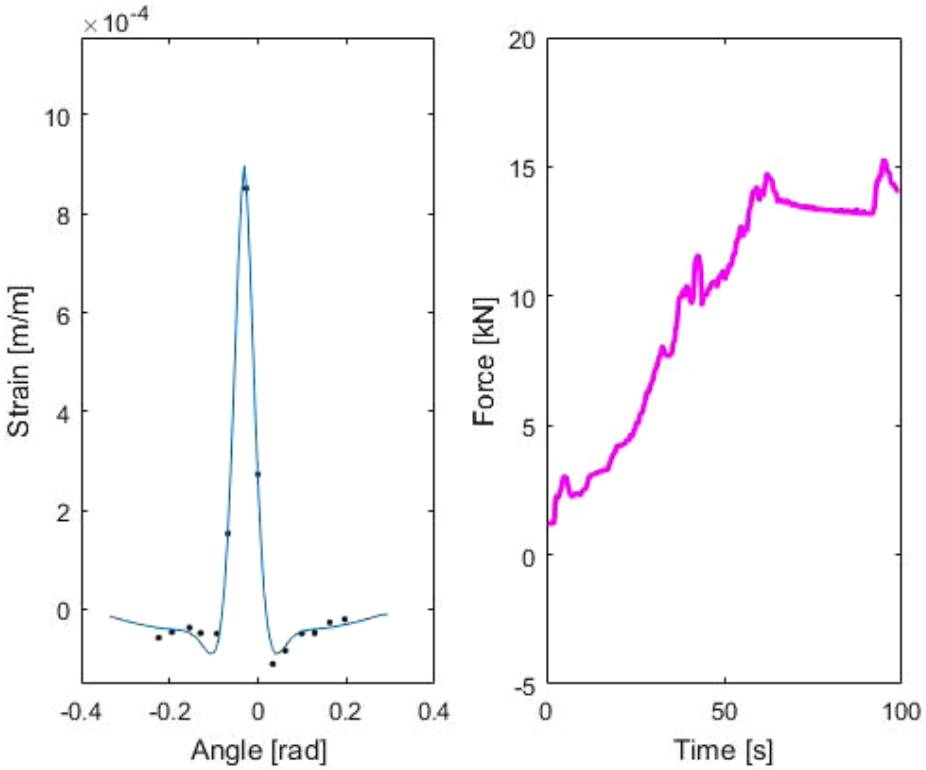

Figure 5.43: Gusto prototype test data using SBI interrogator (left: fitted strain distribution over the sensors at last measured time, right: applied load over time)(2/2)

In order to simulate the data processing of the Smartscan SBI interrogator, the reflective spectra data from the NI interrogator was reduced to the resolution of the SBI interrogator. This was done by omitting data between wavelength steps of the SBI interrogator. This was done by setting the first step of the SBI interrogator equal to the first step of the NI interrogator and taking the 25th data point of the NI interrogator as the second data point of the SBI interrogator (25 times 4 pm equals 0.1 nm, the resolution step of the SBI interrogator), the data was not averaged in any way. With the obtained reflective spectra,

different peak detection settings were used in order to generate the strain distribution over the sensors. The SBI interrogator uses a fixed amount of points around the detected peak in order to come up with a centroid for the peak and no threshold is used. Figure 5.44 shows the strain distribution of position 2 at 35 kN, using the SBI mapped data and a centroid peak detection method, using 17 points (8 points around the peak, resulting in a peak detection over 1.7 nm of wavelength spectra) with no threshold. Comparing this to Figure 5.42, shows that some sensors are affected more than others by the change in resolution and peak detection method. When reducing the amount of points per peak detection even further, as is shown in Figure 5.45, where only 13 points were used for the peak detection, the fitted strain distribution is comparable to the one observed by SKF. It was found that when the amount of points per peak detection is reduced, the negative strains near the strain peaks become more distinct, this was happening for all measured rolling element positions. The actual peak detection method for the Smartscan SBI uses 19 points per peak detection, the reason for lowering this amount is in order to assess/simulate the peak detection method behavior when peak widening occurs.

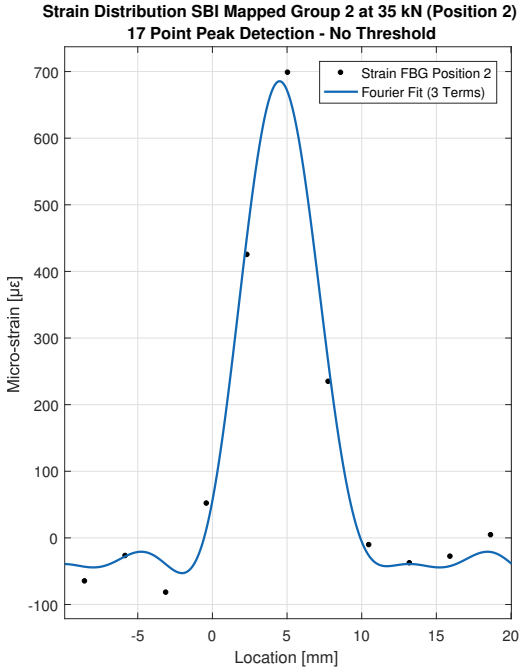

Figure 5.44: Fourier Fit on SBI mapped data using NI interrogator, 17 points peak detection (no threshold) - Position 2 Group 2 35kN

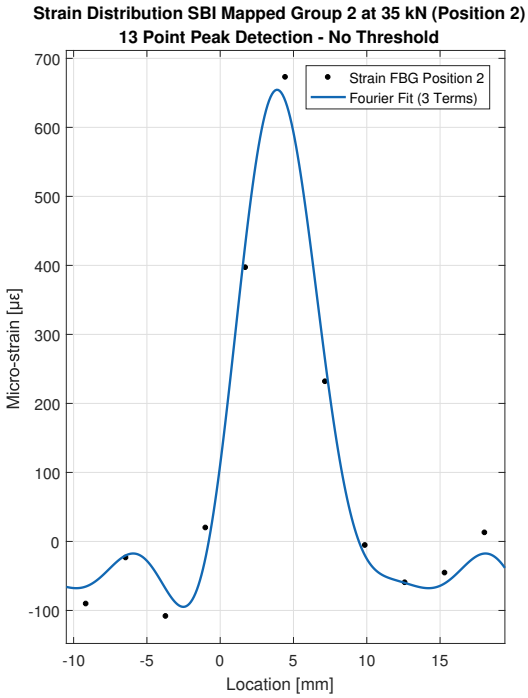

Figure 5.45: Fourier Fit on SBI mapped data using NI interrogator, 13 points peak detection (no threshold) - Position 2 Group 2 35kN

Regardless of the change in FWHM for different load conditions, Section 5.2.3 showed that there were also differences in FWHM between sensors. Figure 5.46 shows the SBI peak detection width for two sensors with different FWHM. The peaks are centered around the data point closest to the peak detected by the centroid peak detection method. As can be observed in the figure, when no threshold is used, peak detection per sensor is not equal. Figure 5.47 shows the same reflective spectra, but with a peak detection width of 13 points. The figures show that, because of the lower resolution of the SBI interrogator, the data point that will be selected for the center point of the peak detection method, will always have an offset to the actual peak. This will result in taking more points into account for the peak detection on one side of the peak in the reflective spectra. When the peak shape and FWHM stays constant during the course of the measurements, this does not affect the strain readout however, when there are changes present in the peak shape and/or FWHM during the measurements, this may result in inconsistent peak detection.

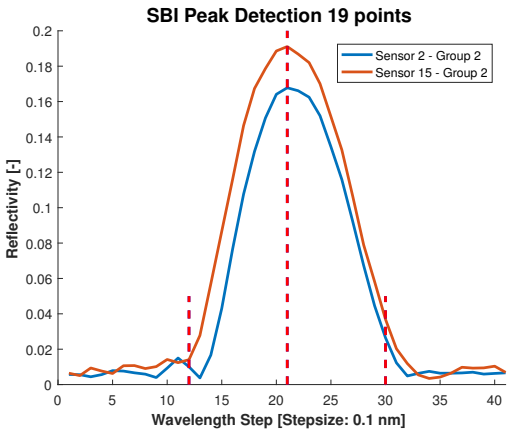

Figure 5.46: SBI mapped spectra using NI interrogator (centered around maximum value in spectra, middle dashed red line), 19 points peak detection (outer dashed red lines) - Position 2 Group 2 35kN

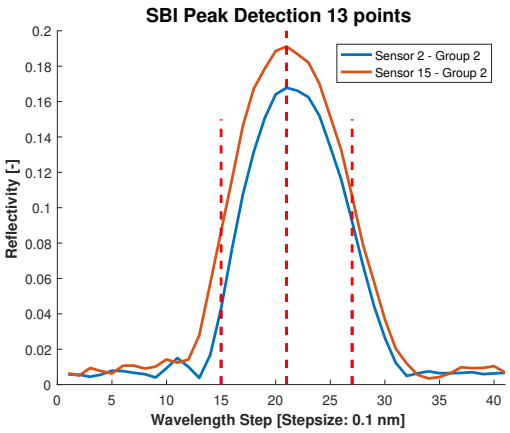

Figure 5.47: SBI mapped spectra using NI interrogator (centered around maximum value in spectra, middle dashed red line), 13 points peak detection (outer dashed red lines) - Position 2 Group 2 35kN

Table 5.5 shows the differences in strain for the different peak detection methods, taking the NI measurements as a base measurement. The NI peak detection method included a threshold of 0.05 reflectivity, a threshold in the SBI interrogator was not possible because the lower resolution gave large steps in the reflectivity. For this comparison it was chosen to compare two sensors on the same fiber, both having the same maximum reflectively. Sensor 1 in Group 2 has a FWHM of 1.124 nm and Sensor 15 in Group 2 a FWHM of 1.224 nm, note that the sensors are located away from the contact point of the rolling element and outer raceway. As can be observed, the absolute difference in strain between the different methods between the sensors is very small, however differences compared to the NI interrogator are up to over 100 %. This can especially have an influence in the lower strain regions of the measurements. Table 5.6 shows the same methods and sensors but for the 20 kN load case. One can observe that for sensor 1, the number of points in the peak detection method have a large effect on the strain readout, while for sensor 15 the differences are small.

Table 5.5: Peak Detection Comparison Sensor 1 and 15 Group 2 at 35 kN Position 1

Sensor #	Interrogator	# Points	Load [kN]	Wavelength [nm]	Strain [$\mu\epsilon$]	Difference
1	NI PXIe 4844	501	35	1531.2753	-24.37	
	SmartScan SBI	13	35	1531.2384	-50.60	107.66%
	SmartScan SBI	15	35	1531.2555	-38.74	58.95%
	SmartScan SBI	17	35	1531.2709	-26.73	9.67%
	SmartScan SBI	19	35	1531.2753	-22.18	-9.00%
15	NI PXIe 4844	501	35	1564.4355	92.19	
	SmartScan SBI	13	35	1564.4117	72.66	-21.19%
	SmartScan SBI	15	35	1564.4183	78.08	-15.30%
	SmartScan SBI	17	35	1564.4287	86.62	-6.04%
	SmartScan SBI	19	35	1564.4371	93.53	1.46%

Table 5.6: Peak Detection Comparison Sensor 1 and 15 Group 2 at 20 kN Position 1

Sensor #	Interrogator	# Points	Load [kN]	Strain [$\mu\epsilon$]	Difference
1	NI PXIe 4844	501	20	-17.58	
	SmartScan SBI	13	20	-46.97	167.16%
	SmartScan SBI	15	20	-34.03	93.55%
	SmartScan SBI	17	20	-21.41	21.80%
	SmartScan SBI	19	20	-17.10	-2.74%
15	NI PXIe 4844	501	20	62.79	
	SmartScan SBI	13	20	58.26	-7.21%
	SmartScan SBI	15	20	60.48	-3.68%
	SmartScan SBI	17	20	63.43	1.02%
	SmartScan SBI	19	20	67.63	7.70%

5.3.1. FWHM and Load

Figures 5.49 and 5.48 give the measured strain and FWHM of FBG sensors 10 and 11 from group 1 in bearing position 1, respectively. Sensor 10 does not show any of the expected peak widening as a result of non-uniform strain over the sensor. Sensor 11 does show some changes in FWHM, the FHWM makes a clear jump every time the applied load is changing to the next step.

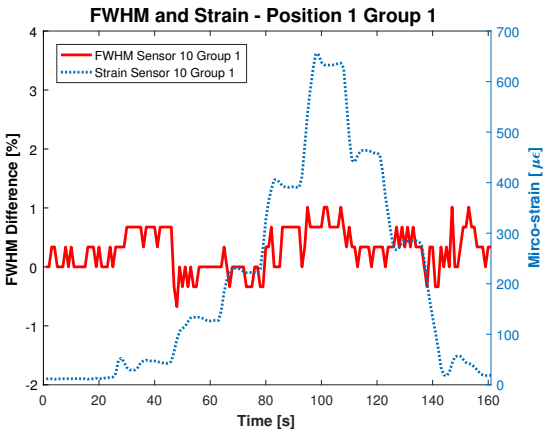

Figure 5.48: FHWM difference w.r.t. initial value (left y-axis) versus measured strain by the FBG sensor in micro-strain (right y-axis) over time (x-axis) - Position 1 Group 1 Sensor 10

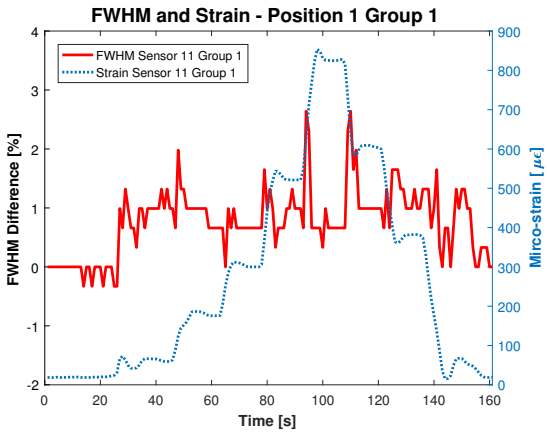

Figure 5.49: FHWM difference w.r.t. initial value (left y-axis) versus measured strain by the FBG sensor in micro-strain (right y-axis) over time (x-axis) - Position 1 Group 1 Sensor 11

Figure 5.51, showing sensor 9 in group 1 in rolling element position 3, shows distinct FHWM increases for increasing applied load, while sensor 8 in the same measurement run shows no distinct steps (Figure 5.50. Figure 5.52 again shows a sensor with distinct FHWM changes for changes in applied load, while the sensor next to it again shows no distinct changes in FHWM (Figure 5.53).

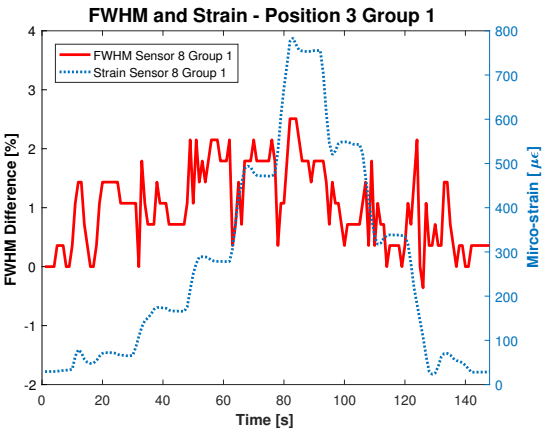

Figure 5.50: FHWM difference w.r.t. initial value (left y-axis) versus measured strain by the FBG sensor in micro-strain (right y-axis) over time (x-axis) - Position 3 Group 1 Sensor 8

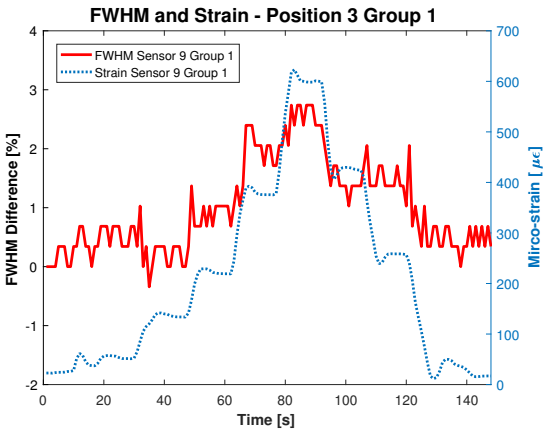

Figure 5.51: FHWM difference w.r.t. initial value (left y-axis) versus measured strain by the FBG sensor in micro-strain (right y-axis) over time (x-axis) - Position 3 Group 1 Sensor 9

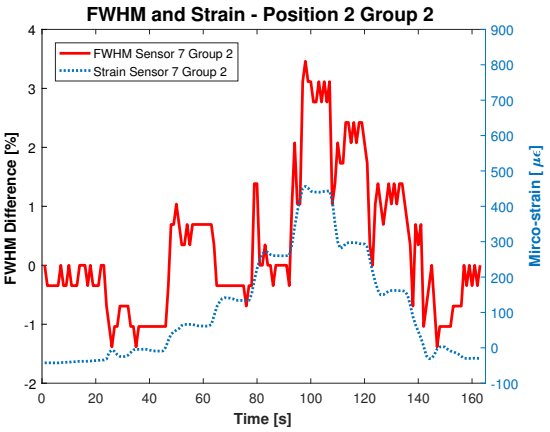

Figure 5.52: FHWM difference w.r.t. initial value (left y-axis) versus measured strain by the FBG sensor in micro-strain (right y-axis) over time (x-axis) - Position 2 Group 2 Sensor 7

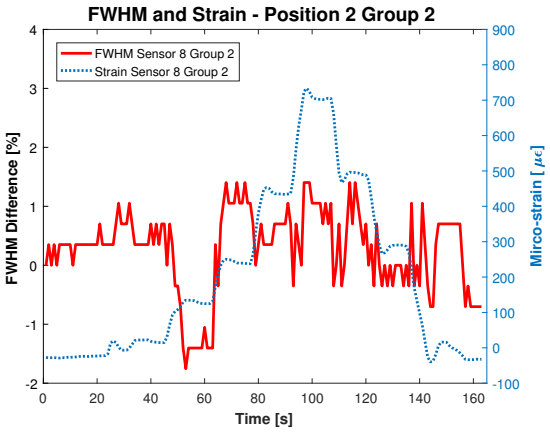

Figure 5.53: FHWM difference w.r.t. initial value (left y-axis) versus measured strain by the FBG sensor in micro-strain (right y-axis) over time (x-axis) - Position 2 Group 2 Sensor 8

Figures 5.54 and 5.55 both show sensor 12 in group 2 for two different rolling element positions. Rolling element position 7 shows an increase in FWHM when load is applied, while rolling element position 8 shows a decrease in FWHM when load is applied.

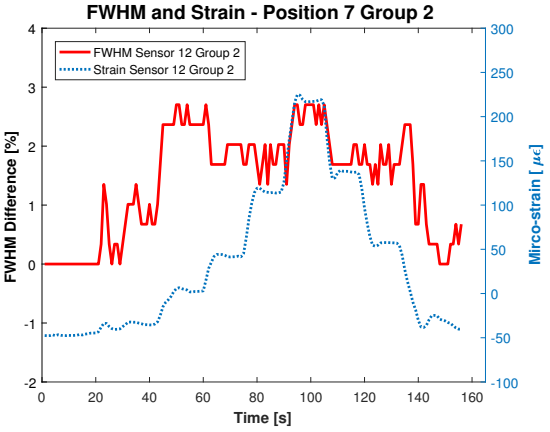

Figure 5.54: FHWM difference w.r.t. initial value (left y-axis) versus measured strain by the FBG sensor in micro-strain (right y-axis) over time (x-axis) - Position 7 Group 2 Sensor 12

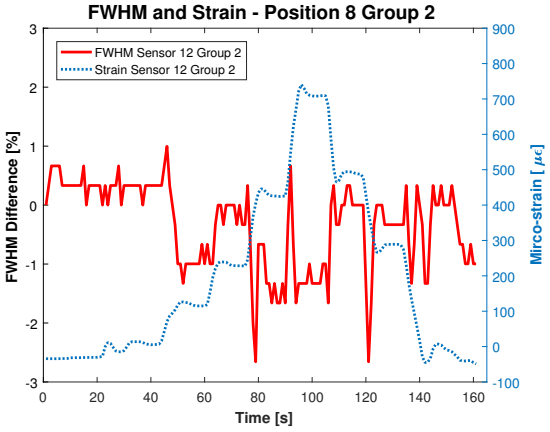

Figure 5.55: FHWM difference w.r.t. initial value (left y-axis) versus measured strain by the FBG sensor in micro-strain (right y-axis) over time (x-axis) - Position 8 Group 2 Sensor 12

See Appendix E for an overview of the rolling element positions (highlighted values in the tables) and all FWHM values for group 1 and 2 at 20 kN and 35 kN. The results shown in this subsection are inconsistent and no clear conclusion can be drawn from the presented results. However, peak widening is occurring and this certainly has an effect on the obtained peaks in the reflective spectra with the current peak detection method. Part of the change in FWHM could also be explained by the waviness in the spectra, as described in Subsection 5.2.2, note that this could also counteract the peak widening observations.

6

Discussion

6.1. Test Phase I

The first test phase focused on the thermal behavior of the FBG sensors. For this test the only variable was temperature. The bearing was heated from 20 to 100 degrees Celsius, with sensor readouts every 5 seconds.

All sensors attached to the Gusto bearing give an overall symmetric response however, a small side peak can be observed for almost every sensor. This side peak does not change for different temperature conditions and is not taken into account with the current peak detection method. Because the side peaks do not change for the measured temperature range, the side peaks are assumed to be irrelevant for this project. No distinct peak splitting can be observed in any of the sensors, indicating no excessive non-uniform (pre-)strain is present in the fibers for the measured temperature range. Differences in peak shapes in the reflective spectra between sensors are present, this may indicate differences in pre-strain between the sensors as a result of the placement of the fibers on the bearing.

It was shown that not all sensors show the same peak displacement due to a temperature change. After correcting for the temperature, a theoretical mechanical strain was obtained. Some sensors showed a difference of up to 80 micro-strain, which would mean a translation of the entire strain reading of 80 micro-strain, depending on the temperature of the bearing at the time of the measurement. This could explain the differences in strain minima and maxima between the sensors. For the maximum load condition of 35 kN, 80 micro-strain is approximately 10 % of the measured maximum strain. Temperature calibration should therefore be done per sensor over the entire range of the operating temperature of the bearing (some sensors show non-linear behavior over the measured temperature range). Temperature differences between sensors could even further increase the strain translation between sensors (temperature is only measured by a single temperature FBG per sensors group). With the conducted measurements, it cannot be explained why some sensors behave differently in different temperature conditions. There is a difference between the theoretical mechanical strain per sensor group on each side of the bearing. As the FBGs on a single side of the bearing are already divided over two fibers, differences in thermal expansion coefficient of the glass is unlikely, as well as differences in the gauge factors. A possible explanation in the difference observed between the two groups could lie in the bonding of the FBGs to the steel. Slight differences in bonding performance may result in different strain loss/strain transfer in the bonding, hence the difference between the two groups.

The FWHM of the FBG sensors are constant over the measured temperature range however, there are differences of FWHM from sensor to sensor on the same fiber. This could indicate that some sensors are subjected to a certain strain distribution, this could be due to bonding inconsistencies, creating a non uniform grating distribution over the sensor. It could also indicate that there are manufacturing differences between the sensors. Another thing one can observe is that the FWHM is slightly decreasing with increasing temperature, this may indicate that the grating distribution is more uniform at higher temperatures, hence a more uniform strain at higher temperatures. The differences in FWHM are how-

ever small and could also be related to the waviness in the reflective spectra, extra tests should be performed in order to assess the significance of these differences.

6.2. Test Phase II

In this test phase the FBG sensors were loaded. Because the two sensor groups were located on opposite sides of the bearing, the tests were conducted separately per sensors group. The sensors were loaded in steps, running up to 35 kN. The duration of one load cycle was 130 s. For each load cycle, the rolling element position w.r.t. the sensors was changed, this was done in a clockwise direction. In order to measure the opposite sensor group, the outer ring of the bearing was rotated 180 degrees.

The tests show that the FWHM and the shape of the peak in the reflective spectra have an influence on how the peak is detected by the Smartscan SBI interrogator. A peak in the reflective spectra with a higher slope on the left will be processed differently than a peak with a higher slope on the right. Also, a change in peak shape may have a larger impact on the peak detection method for sensors with a smaller FWHM compared to sensors with a larger FWHM.

The differences observed between the sensors could therefore be explained by noting that the FWHM of the sensors located further away from the connector are higher. The peak detection of the sensors is therefore not consistent, this inconsistency will especially be visible in areas of low and non-uniform strain, hence near the strain peaks. As can also be seen in the test results of SKF, sensors further to the right (sensors with notably larger FWHMs) in Figure 6.1 show different behavior in the areas near the strain peaks.

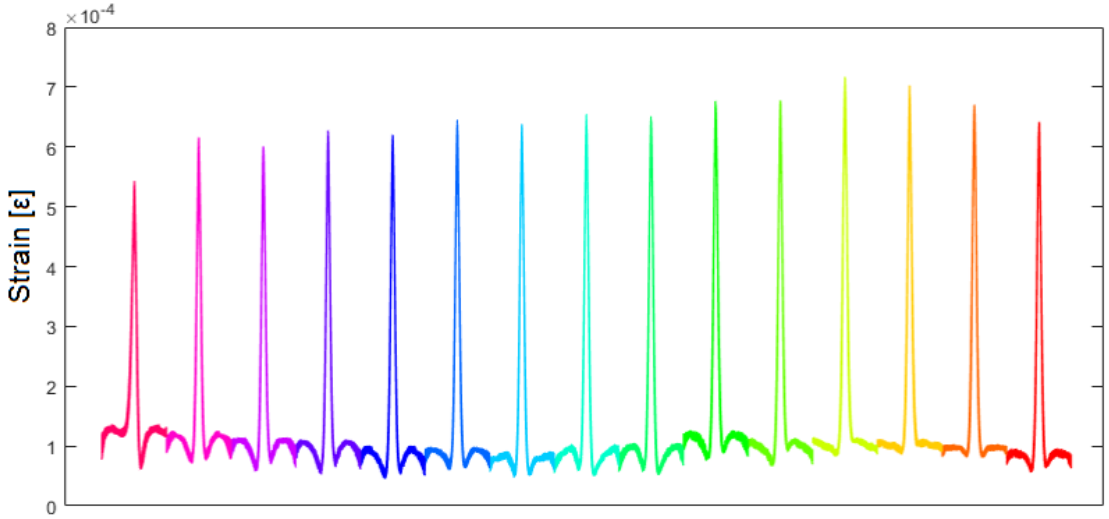

Figure 6.1: Superimposed strain signal of 60+ rolling elements of multiple FBG sensors in close proximity of each other [74]

6.3. Research Objective

This project was initiated with the objective to answer the following research question;

"What causes the observed differences in the strain distribution from sensor to sensor in a rolling element bearing equipped with Fiber Bragg Gratings sensors?"

This question was based on the differences observed in the Gusto bearing. It was chosen to further test the Gusto bearing with an interrogator capable of scanning the reflective spectra with a resolution 25 times higher compared to the interrogator used by SKF in the original measurements. These tests showed that in the operating temperature range of the Gusto bearing, sensors may behave differently to the temperature changes w.r.t. each other, resulting in a translation of the strain levels between sensors. Furthermore, it was observed that the negative strains near the strain peaks in the strain distribution for a single rolling element, were not as distinct when measured with the higher resolution interrogator. This may be explained by a combination of the peak detection method used by the SBI

interrogator, the lower resolution of the SBI interrogator and the differences in FWHMs between the sensors and between different load conditions.

6.4. Recommendations

Add an additional temperature FBG to the groups in order to obtain a better estimate of the temperature distribution over the sensors. Every sensor should be calibrated for temperature separately, as not every sensor is behaving the same in different temperature conditions. Another method for obtaining a better temperature distribution is by using two types of FBGs which react differently to the same strain field. From the difference between the two sensor types, the temperature could be extracted [54].

During the measurements it was observed that the FWHM for sensors closest to the connector was lower compared to sensors furthest away from the connector. This could be due to bonding differences of the FBGs, an additional sensor readout with a batch of sensors not yet attached to a bearing could give a good indication whether this observation is caused by the placement method or not.

Additional research should be performed to the consequences of using off-the-shelf peak detection methods for the given application. Highly dynamic and non-uniform strain over the sensors may require different peak detection methods than the one used by the SBI interrogator. This method should take into account the FWHM of every sensor for every measurement and the shape of the peak in the reflective spectra.

6.5. Suggestions for Future Research

During the measurements it was observed that for some load cases and sensors, the peak in the reflective spectra showed waviness. The NI interrogator was able to detect this waviness however, it is not known how the SBI interrogator copes with this phenomena. Depending on the shape and place in the spectra, the SBI interrogator could read the peak in the spectra with maxima or minima in the waves only. Figure 6.2 gives the reflective spectra of sensor 12 on group 2, which is showing some waviness in the reflective spectra. Figure 6.3 shows sensor 2 on group 2, which shows a far more smooth reflective spectra. The effect and origin of the waviness in the reflective spectra could be assessed in further research.

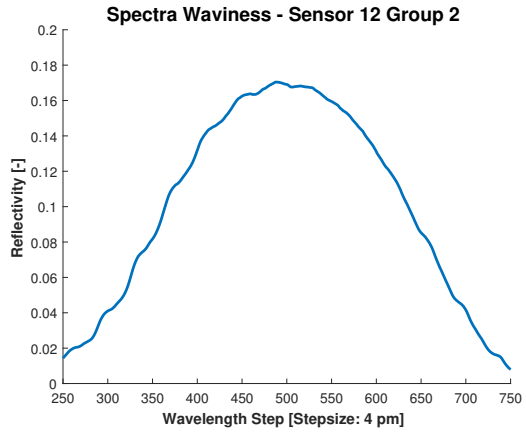

Figure 6.2: Spectra Waviness - Position 2 Group 2 Sensor 12

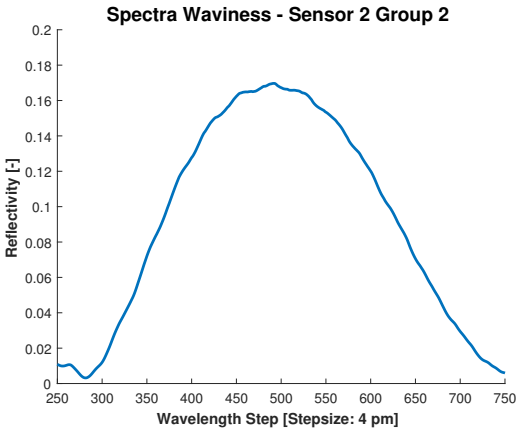

Figure 6.3: Spectra Waviness - Position 2 Group 2 Sensor 2

Further research could focus on assessing the behavior of the sensors in different positions in the strain distribution of the rolling element, as shown in Figure 6.4. Here the strain profile for different rolling element positions w.r.t. the sensors was superimposed in order to create a strain for the rolling element in question. For this profile 9 rolling element positions were used. For the creation of a more consistent peak detection method, a peak shape analysis could be performed on all obtained reflective spectra during this project, taking into account the positions of the sensors in the strain profile. Also the origins and prevention of measurement errors could be further assessed.

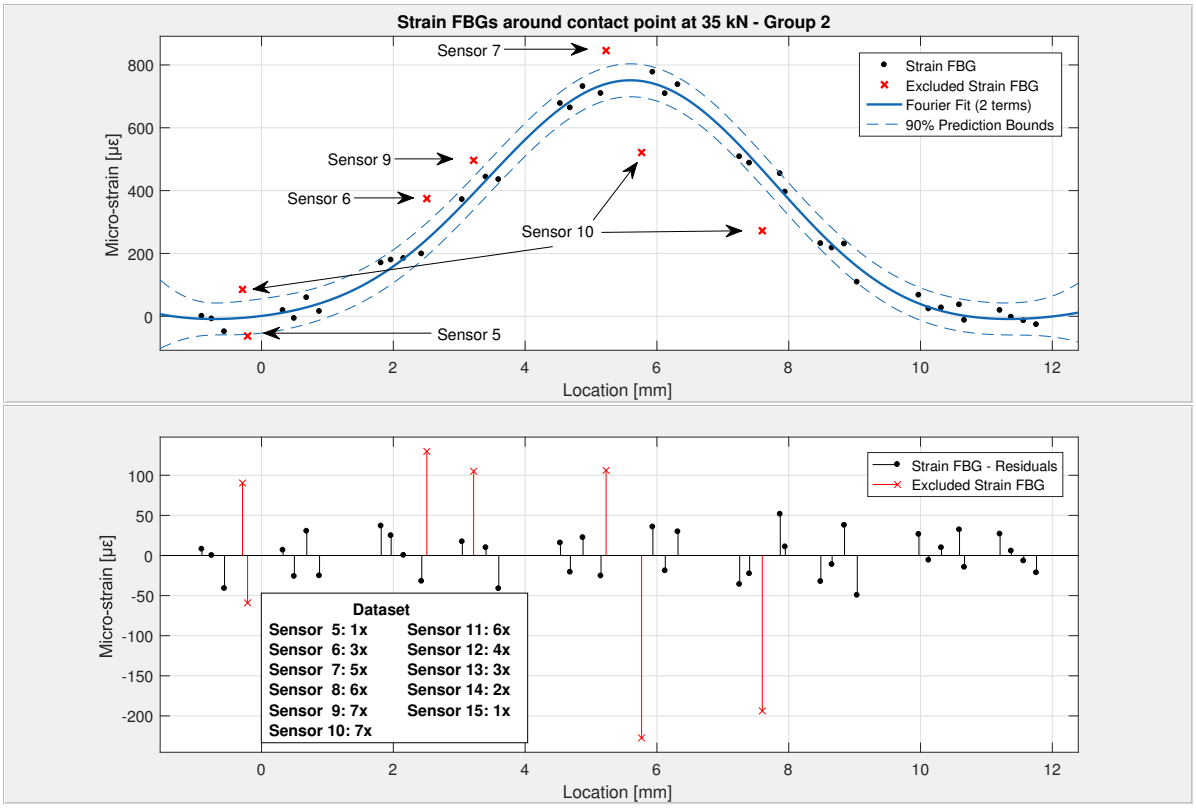

Figure 6.4: Fourier fit on strain FBGs located at contact point for positions 1 to 9 - Group 2 35kN

Bibliography

[1] D. Z. Anderson, V. Mizrahi, T. Erdogan, and A. E. White. Production of in-fibre gratings using a diffractive optical element. Electronics Letters, 29:566, Jan-01-1993 1993. ISSN 00135194. doi: 10.1049/el:19930379.

[2] I. Ashry, A. Elrashidi, A. Mahros, M. Alhaddad, and K. Elleithy. Investigating the performance of apodized Fiber Bragg gratings for sensing applications. Proceedings of the 2014 Zone 1 Conference of the American Society for Engineering Education - "Engineering Education: Industry Involvement and Interdisciplinary Trends", ASEE Zone 1 2014, 2014. doi: 10.1109/ASEEZone1.2014.6820640.

[3] Charles G. Askins, Martin A. Putnam, and E. J. Friebele. Instrumentation for interrogating many-element fiber bragg grating arrays. Proc. SPIE, 2444:257–266, 1995. doi: 10.1117/12.207681. URL http://dx.doi.org/10.1117/12.207681.

[4] Vikram Bhatia. Properties and Sensing Applications of Long-Period Gratings. PhD thesis, Virginia Polytechnic Institue and State University, 1996.

[5] Vikram Bhatia. Applications of long-period gratings to single and multi-parameter sensing. Optics express, 4(11):457–466, 1999. ISSN 1094-4087. doi: 10.1364/OE.4.000457. URL http://www.osapublishing.org/abstract.cfm?uri=oe-4-11-457{%}5Cnhttps://www.osapublishing.org/oe/abstract.cfm?uri=oe-4-11-457{%}5Cnhttp://www.opticsinfobase.org/abstract.cfm?URI=oe-4-11-457.

[6] G.P. Brady, S. Hope, A.B.Lobo Ribeiro, D.J. Webb, L. Reekie, J.L. Archambault, and D.A. Jackson. Demultiplexing of fibre Bragg grating temperature and strain sensors. Optics Communications, 111(1-2):51–54, 1994. ISSN 00304018. doi: 10.1016/0030-4018(94)90137-6. URL http://www.sciencedirect.com/science/article/pii/0030401894901376.

[7] Luis P. Canal, Roohollah Sarfaraz, Georgios Violakis, John Botsis, Véronique Michaud, and Hans G. Limberger. Monitoring strain gradients in adhesive composite joints by embedded fiber Bragg grating sensors. Composite Structures, 112(1):241–247, 2014. ISSN 02638223. doi: 10.1016/j.compstruct.2014.02.014. URL http://dx.doi.org/10.1016/j.compstruct.2014.02.014.

[8] C Caucheteur, S Bette, H Ottevaere, T Nasilowski, M Wuilpart, F Berghmans, H. Thienpont, and P. Mégret. Study of the polarization properties of fiber Bragg gratings for sensing purposes. Leosbenelux.Org, 2(1):309–312, 2005. URL http://leosbenelux.org/symp05/s05p309.pdf.

[9] WH Chung, Hwa-Yaw Tam, P.K.A. Wai, and A. Khandelwal. Time- and wavelength-division multiplexing of FBG sensors using a semiconductor optical amplifier in ring cavity configuration. IEEE Photonics Technology Letters, 17(12):2709–2711, 2005. ISSN 1041-1135. doi: 10.1109/LPT.2005.859484. URL http://www.en.polyu.edu.hk/{~}wai/journal/ptl{_}05e.pdf{%}5Cnhttp://ieeexplore.ieee.org/lpdocs/epic03/wrapper.htm?arnumber=1542198.

[10] G. A. Cranch, G. M. H. Flockhart, and C. K. Kirkendall. Efficient large-scale multiplexing of fiber Bragg grating and fiber Fabry-Perot sensors for structural health monitoring applications. Proc. SPIE 6179, 6179:61790P, 2006. ISSN 0277786X. doi: 10.1117/12.657416. URL http://proceedings.spiedigitallibrary.org/proceeding.aspx?articleid=1324448.

[11] Bhargab Das and Vikash Chandra. Fiber-MZI-based FBG sensor interrogation : comparative study with a CCD spectrometer. Applied Optics, 55(29):8287 – 8292, 2016.

[12] M A Davis and A D Kersey. All-fibre Bragg grating strain-sensor demodulation technique using a wavelength division coupler. Smr/Eso, 30(1):75–77, 1994. ISSN 00135194. doi: 10.1049/el:19940059.

[13] M. A. Davis and A. D. Kersey. Application of a Fiber Fourier Transform Spectrometer to the Detection of Wavelength-Encoded Signals from Bragg Grating Sensors. Journal of Lightwave Technology, 13(7):1289–1295, 1995. ISSN 15582213. doi: 10.1109/50.400685.

[14] Maxence Borot de Battisti, Baudouin Denis de Senneville, Metha Maenhout, Jan J W Lagendijk, Marco van Vulpen, Gilion Hautvast, Dirk Binnekamp, and Marinus A Moerland. Fiber Bragg gratings-based sensing for real-time needle tracking during MR-guided brachytherapy. Medical Physics, 43(10):5288–5297, 2016. ISSN 00942405. URL http://10.0.4.94/1.4961743{%}0Ahttp://search.ebscohost.com/login.aspx?direct=true{&}db=a9h{&}AN=118580622{&}site=ehost-live.

[15] Raffaella Di Sante. Fibre Optic Sensors for Structural Health Monitoring of Aircraft Composite Structures: Recent Advances and Applications. Sensors (Basel, Switzerland), 15(8):18666–18713, 2015. ISSN 1424-8220. doi: 10.3390/s150818666. URL http://www.mdpi.com/1424-8220/15/8/18666/htm.

[16] Xiaoyi Dong, Hao Zhang, Bo Liu, and Yinping Miao. Tilted fiber bragg gratings: Principle and sensing applications. Photonic Sensors, 1(1):6–30, 2011. ISSN 16749251. doi: 10.1007/s13320-010-0016-x.

[17] Lukasz Dziuda, Franciszek Wojciech Skibniewski, Mariusz Krej, and Jaroslaw Lewandowski. Monitoring respiration and cardiac activity using fiber Bragg grating-based sensor. IEEE Transactions on Biomedical Engineering, 59(7):1934–1942, 2012. ISSN 00189294. doi: 10.1109/TBME.2012.2194145.

[18] Coenraad Esveld. Geometrisch en constructief ontwerp van wegen en spoorwegen. Number September. TU Delft, Delft, 2005.

[19] Chaoui Fahd, Aghzout Otman, Chakkour Mounia, and E L Yakhloufi Mounir. Apodization Optimization of FBG Strain Sensor for Quasi-distributed Sensing Measurement Applications. Active and Passive Electronic Components, 2016, 2016. URL http://dx.doi.org/10.1155/2016/6523046.

[20] Shiuh Chuan Her and Chih Ying Huang. Effect of coating on the strain transfer of optical fiber sensors. Sensors, 11(7):6926–6941, 2011. ISSN 14248220. doi: 10.3390/s110706926.

[21] K O Hill. Aperiodic Distributed-Parameter Waveguides for Integrated Optics. Applied Optics, 13 (8):1853–1856, 1974. ISSN 0003-6935. doi: 10.1364/AO.13.001853. URL http://ao.osa.org/abstract.cfm?URI=ao-13-8-1853.

[22] K. O. Hill, Y. Fujii, D. C. Johnson, and B. S. Kawasaki. Photosensitivity in optical fiber waveguides: Application to reflection filter fabrication. Applied Physics Letters, 32(10):647–649, 1978. ISSN 10773118. doi: 10.1063/1.89881.

[23] K. O. Hill, B. Malo, F. Bilodeau, D. C. Johnson, and J. Albert. Bragg gratings fabricated in monomode photosensitive optical fiber by UV exposure through a phase mask. Applied Physics Letters, 62(10):1035–1037, 1993. ISSN 00036951. doi: 10.1063/1.108786.

[24] Kenneth O. Hill and Gerald Meltz. Fiber Bragg grating technology fundamentals and overview. Journal of Lightwave Technology, 15(8):1263–1276, 1997. ISSN 07338724. doi: 10.1109/50.618320.

[25] Seong-Wook Hong and Van-Canh Tong. Rolling-element bearing modeling: A review. International Journal of Precision Engineering and Manufacturing, 17(12):1729–1749, 2016. ISSN 2234-7593. doi: 10.1007/s12541-016-0200-z. URL http://link.springer.com/10.1007/s12541-016-0200-z.

[26] Hong Mei Huang and Shen Fang Yuan. Study on the spectral response of fiber Bragg grating sensor under non-uniform strain distribution in structural health monitoring. Optoelectronics Letters, 7(2):109–112, 2011. ISSN 1673-1905. doi: 10.1007/s11801-011-0089-9. URL http://www.springerlink.com/content/h633q50294610240/.

[27] Keisuke Imade, Takashi Kageyama, Daisuke Koyama, Yoshiaki Watanabe, Kentaro Nakamura, and Iwaki Akiyama. Measurement of sound pressure and temperature in tissue-mimicking material using an optical fiber Bragg grating sensor. Journal of Medical Ultrasonics, 43(4):473–479, 2016. ISSN 16132254. doi: 10.1007/s10396-016-0726-9.

[28] D A Jackson, A B Lobo Ribeiro, Applied Optics Group, L Reekie, and J L Archambault. Simple multiplexing scheme for a fiber-optic Grating Sensor Network. Optics Letters, 18(14):1192–1194, 1993.

[29] Stephen W James and Ralph P Tatam. Optical fibre long-period grating sensors: characteristics and application. Measurement Science and Technology, 14(5):R49–R61, 2003. ISSN 0957-0233. doi: 10.1088/0957-0233/14/5/201.

[30] Eun Joo Jung, Chang-Seok Kim, Myung Yung Jeong, Moon Ki Kim, Min Yong Jeon, Woonggyu Jung, and Zhongping Chen. Characterization of FBG sensor interrogation based on a FDML wavelength swept laser. Optics express, 16(21):16552–16560, 2008. ISSN 1094-4087. doi: 10.1364/OE.16.016552.

[31] Patrick Paskalis Kanopoulos. Development of a Fibre Bragg Grating Sensor for Rock Defermation Monitoring. PhD thesis, University of Toronto, 2014.

[32] B S Kawasaki, K O Hill, D C Johnson, and Y Fujii. Narrow-band Bragg reflectors in optical fibers. Optics Letters, 3(2):66–68, 1978. ISSN 0146-9592. doi: 10.1364/OL.3.000066. URL http://ol.osa.org/abstract.cfm?URI=ol-3-2-66.

[33] A D Kersey, T A Berkoff, and W W Morey. Multiplexed Fiber Bragg Grating Strain-Sensor System with a Fiber Fabry-Perot Wavelength Filter. Optics Letters, 18(16):1370–1372, 1993. ISSN 0146-9592. doi: 10.1364/OL.18.001370.

[34] M J Kim, Y H Kim, G Mudhana, and B H Lee. Simultaneous Measurement of Temperature and Strain Based on Double Cladding Fiber Interferometer Assisted by Fiber Grating Pair. IEEE Photon. Technol. Lett., 20(15):1290–1292, 2008. ISSN 08952477. doi: 10.1002/mop.23644.

[35] KMJ. Smartscan udp message format. Technical report, Smart Fibers, 141 Dedworth Road - Windsor - Berkshire -SL4 5BB - United Kingdom, August 2011. Document Ref:7-049-3018-D.

[36] Robert Kunc, Andrej Žerovnik, and Ivan Prebil. Verification of numerical determination of carrying capacity of large rolling bearings with hardened raceway. International Journal of Fatigue, 29 (9-11):1913–1919, 2007. ISSN 01421123. doi: 10.1016/j.ijfatigue.2007.02.003.

[37] Yong Seok Kwon, Myeong Ock Ko, Mi Sun Jung, Ik Gon Park, Namje Kim, Sang Pil Han, Han Cheol Ryu, Kyung Hyun Park, and Min Yong Jeon. Dynamic sensor interrogation using wavelength-swept laser with a polygon-scanner-based wavelength filter. Sensors (Basel, Switzerland), 13(8):9669–9678, 2013. ISSN 14248220. doi: 10.3390/s130809669.

[38] Alfredo Lamberti, Steve Vanlanduit, Ben De Pauw, and Francis Berghmans. Influence of fiber bragg grating spectrum degradation on the performance of sensor interrogation algorithms. Sensors (Switzerland), 14(12):24258–24277, 2014. ISSN 14248220. doi: 10.3390/s141224258.

[39] D. Leduc, Y. Lecieux, P. A. Morvan, and C. Lupi. Architecture of optical fiber sensor for the simultaneous measurement of axial and radial strains. Smart Materials and Structures, 22(7):075002, 2013. ISSN 0964-1726. doi: 10.1088/0964-1726/22/7/075002. URL http://stacks.iop.org/0964-1726/22/i=7/a=075002?key=crossref.e16261102a28d3e0a6e4bfa13a800663.

[40] B C Lee, E J Jung, C S Kim, and M Y Jeon. Dynamic and static strain fiber Bragg grating sensor interrogation with a 1.3 mu m Fourier domain mode-locked wavelength-swept laser. Measurement Science & Technology, 21(9):–, 2010. ISSN 0957-0233. doi: 10.1088/0957-0233/21/9/094008.

[41] Hojoon Lee. Multiple fiber Bragg grating sensor system using code-division multiple access. Applied optics, 41(25):5245–8, 2002. ISSN 0003-6935. doi: 10.1364/AO.41.005245. URL http://www.ncbi.nlm.nih.gov/pubmed/12211549.

[42] Hwi Don Lee, Gyeong Hun Kim, Tae Joong Eom, Myung Yung Jeong, and Chang-seok Kim. Linearized Wavelength Interrogation System of Fiber Bragg Grating Strain Sensor Based on Wavelength-Swept Active Mode Locking Fiber Laser. Journal of Lightwave Technology, 33(12): 2617–2622, 2015.

[43] Hyung Seok Lee, Hwi Don Lee, Hyo Jin Kim, Jae Du Cho, Myung Yung Jeong, and Chang Seok Kim. A fiber bragg grating sensor interrogation system based on a linearly wavelength-swept thermo-optic laser chip. Sensors (Switzerland), 14(9):16109–16116, 2014. ISSN 14248220. doi: 10.3390/s140916109.

[44] Keunwoo Lee, Joohyung Lee, Yoon-Soo Jang, Seongheum Han, Heesuk Jang, Young-Jin Kim, and Seung-Woo Kim. Fourier-transform spectroscopy using an Er-doped fiber femtosecond laser by sweeping the pulse repetition rate. Scientific reports, 5 (October):15726, 2015. ISSN 2045-2322. doi: 10.1038/srep15726. URL http://www.pubmedcentral.nih.gov/articlerender.fcgi?artid=4621541{&}tool=pmcentrez{&}rendertype=abstract.

[45] Oleg P Lelikov. Mechanical Drives. In Karl-Heinrich Grote Professor Dr.-Ing. and Erik K. Antonsson Professor, editors, Springer Handbook of Mechanical Engineering, chapter 6, pages 327–522. Springer Berlin Heidelberg, 2009. ISBN 978-3-540-49131-6. doi: 10.1007/978-3-540-30738-9.

[46] Hong Li, Lianqing Zhu, Mingli Dong, Xiaoping Lou, and Yangkuan Guo. Analysis on strain transfer of surface-bonding FBG on Al 7075-T6 alloy host. Optik, 127(3):1233–1236, 2016. ISSN 00304026. doi: 10.1016/j.ijleo.2015.10.227. URL http://dx.doi.org/10.1016/j.ijleo.2015.10.227.

[47] Kuo Li. Review of the Strain Modulation Methods Used in Fiber Bragg Grating Sensors. Journal of Sensors, 2016, 2016. ISSN 16877268. doi: 10.1155/2016/1284520.

[48] H.-Y. Ling, K.-T. Lau, L. Cheng, and K.-W. Chow. Embedded fibre Bragg grating sensors for non-uniform strain sensing in composite structures. Measurement Science and Technology, 16(12): 2415–2424, 2005. ISSN 09570233 13616501. doi: 10.1088/0957-0233/16/12/003.

[49] Qinpeng Liu, Xueguang Qiao, Zhen'an Jia, and Haiwei Fu. Spectra power and bandwidth of fiber Bragg grating under influence of gradient strain. Photonic Sensors, 6(4):333–338, 2016. ISSN 1674-9251. doi: 10.1007/s13320-016-0325-9. URL http://link.springer.com/10.1007/s13320-016-0325-9.

[50] Y. Liu, L. Zhang, and I. Bennion. Fibre optic load sensors with high transverse strain sensitivity based on long-period gratings in B/Ge co-doped fibre. Electronics Letters, 35(8):661–663, 1999. ISSN 00135194. doi: 10.1049/el:19990457.

[51] Nikhil D Londhe, Nagaraj K Arakere, and Raphael T Haftka. Reevaluation of Rolling Element Bearing Load-Life Equation Based on Fatigue Endurance Data. Tribology Transactions, 58(5): 815–828, 2015. ISSN 1040-2004. doi: 10.1080/10402004.2015.1021943. URL http://dx.doi.org/10.1080/10402004.2015.1021943.

[52] Ana Luísa Correia Dias Loureiro. Determination of the strain distribution in the adhesive joints using Fiber Bragg Grating (FBG). PhD thesis, Faculdade de Engenharia Universidade do Porto, 2011.

[53] G Luyckx, W De Waele, J Degrieck, W Van Paepegem, J Vlekken, S Vandamme, and K Chah. Three-dimensional strain and temperature monitoring of composite laminates. Insight - Non-Destructive Testing and Condition Monitoring, 49(1):10–16, 2007. ISSN 1354-2575. doi: 10.1784/insi.2007.49.1.10.

[54] Geert Luyckx, Eli Voet, Nicolas Lammens, and Joris Degrieck. Strain measurements of composite laminates with embedded fibre bragg gratings: Criticism and opportunities for research. Sensors, 11(1):384–408, 2011. ISSN 14248220. doi: 10.3390/s110100384.

[55] Peijun Ma, Shuai Wang, Lingling Zhao, Michael Pecht, Xiaohong Su, and Zhe Ye. An improved exponential model for predicting the remaining useful life of Rolling Element Bearings. 2015 IEEE Conference on Prognostics and Health Management: Enhancing Safety, Efficiency, Availability, and Effectiveness of Systems Through PHAf Technology and Application, PHM 2015, 62(12): 7762–7773, 2015. ISSN 0278-0046. doi: 10.1109/ICPHM.2015.7245060.

[56] Masanori Matsuhara and K Hill. Optical-Waveguide Band-Rejection Filters : Design. Applied optics, 13(12):2886–2889, 1974.

[57] Serge M. Melle, Kexing Liu, and Raymond M. Measures. A Passive Wavelength Demodulation System for Guided-Wave Bragg Grating Sensors. IEEE Photonics Technology Letters, 4(5):516–518, 1992. ISSN 19410174. doi: 10.1109/68.136506.

[58] G Meltz, W W Morey, and W H Glenn. Formation of Bragg gratings in optical fibers by a transverse holographic method. Optics Letters, 14(15):823–825, 1989. ISSN 0146-9592. doi: 10.1364/OL.14.000823.

[59] Y Mizutani and Roger M Groves. Multi-Functional Measurement Using a Single FBG Sensor. Experimental Mechanics, 2011. doi: 10.1007/s11340-011-9467-2.

[60] L. C S Nunes, Bruno S. Olivieri, Carla C. Kato, L. C G Valente, and A. M B Braga. FBG sensor multiplexing system based on the TDM and fixed filters approach. Sensors and Actuators, A: Physical, 138(2):341–349, 2007. ISSN 09244247. doi: 10.1016/j.sna.2007.05.009.

[61] Andreas Onoufriou, Kyriacos Kalli, David Pureur, and Alain Mugnier. Fibre Bragg Gratings. In Springer Series in Optical Sciences, pages 189–269. ResearchGate, 2006. doi: 10.1007/3-540-31770-8.

[62] Andreas Othonos. Fiber bragg gratings. Review of scientific instruments, 68(12):4309–4341, 1997.

[63] Dick Petersen, Carl Howard, Nader Sawalhi, Alireza Moazen Ahmadi, and Sarabjeet Singh. Analysis of bearing stiffness variations, contact forces and vibrations in radially loaded double row rolling element bearings with raceway defects. Mechanical Systems and Signal Processing, 50-51:139–160, 2015. ISSN 10961216. doi: 10.1016/j.ymssp.2014.04.014. URL http://dx.doi.org/10.1016/j.ymssp.2014.04.014.

[64] Joseph V. Poplawski, Steven M. Peters, and Erwin V. Zaretsky. Effect Of Roller Profile On Cylindrical Roller Bearing Life Prediction—Part I: Comparison of Bearing Life Theories. Tribology Transactions, 44(3):339–350, 2001. ISSN 1040-2004. doi: 10.1080/10402000108982466. URL http://www.tandfonline.com/doi/abs/10.1080/10402000108982466.

[65] J Qi. A comparison study of the sensing characteristics of FBG and TFBG. Sensor Review, 33 (1):68–79, 2013. ISSN 0260-2288. doi: 10.1108/02602281311294360.

[66] Yasukazu Sano and Toshihiko Yoshino. Employing Arrayed Waveguide Grating for Distributed Fiber Bragg Grating Sensors. Lightwave Technology, Journal of, 21(1):132–139, 2003.

[67] N. Sawalhi and R. B. Randall. Simulating gear and bearing interactions in the presence of faults. Part I. The combined gear bearing dynamic model and the simulation of localised bearing faults. Mechanical Systems and Signal Processing, 22(8):1924–1951, 2008. ISSN 08883270. doi: 10.1016/j.ymssp.2007.12.001.

[68] N. Sawalhi and R. B. Randall. Simulating gear and bearing interactions in the presence of faults Part II: Simulation of the vibrations produced by extended bearing faults. Mechanical Systems and Signal Processing, 22(8):1952–1966, 2008. ISSN 0888-3270. doi: 10.1016/j.ymssp.2007.12.002.

[69] Debabrata Sikdar, Vinita Tiwari, Anupam Soni, Ritesh Jaiswal, and Surekha Bhanot. Polarization multiplexed interrogation technique for FBG sensor array. Photonic Sensors, 5(3):193–201, 2015. ISSN 21907439. doi: 10.1007/s13320-015-0235-2.

[70] SKF. Railway technical handbook volume 1 - axleboxes, wheelset bearings, sensors, condition monitoring, subsystems and services. Technical report, SKF Group, 2012. Chapter 5, p 108.

[71] SKF Group. SKF Rolling Bearings Catalogue. 2016.

[72] Alexander Slocum. Fundamentals of Design - Topic 10 - Bearings. chapter 10, pages 10–1–10–38. Massachusetts Institute of Technology, Cambridge, Massachusetts, USA, 2008. ISBN 0802713122.

[73] SmartScan SBI Single Board Interrogator - For OEM Integration into Customer Systems. Smart Fibres, 2017.

[74] Stijn van Eesbeek. Algorithm design - i15177 nmo fiber optical sensing for pumps & compressors. Powerpoint, 2017. SKF Internal Document.

[75] Kai Tai Wan, Christopher K Y Leung, and Noah G Olson. Investigation of the strain transfer for surface-attached optical fiber strain sensors. Smart Materials and Structures, 17(3):035037, 2008. ISSN 0964-1726. doi: 10.1088/0964-1726/17/3/035037.

[76] Q B Wang, Y Qiu, H T Zhao, J A Chen, Y Y Wang, and Z M Fan. Analysis of strain transfer of six-layer surface-bonded fiber Bragg gratings. Applied Optics, 51(18):4129–4138, 2012. ISSN 15394522. doi: 10.1364/AO.51.004129.

[77] Marcelo M Werneck, Regina C S B Allil, Bessie A Ribeiro, and Fábio V B De Nazaré. A Guide to Fiber Bragg Grating Sensors. Intech, pages 1–24, 2013. doi: 10.5772/54682. URL http://cdn.intechopen.com/pdfs-wm/44684.pdf.

[78] S. Yashiro, T. Okabe, N. Toyama, and N. Takeda. Monitoring damage in holed CFRP laminates using embedded chirped FBG sensors. International Journal of Solids and Structures, 44(2):603–613, 2006. ISSN 00207683. doi: 10.1016/j.ijsolstr.2006.05.004.

[79] Syed Farhan Haider Zaidi. Advanced Dynamic Interrogation Techniques for Hybrid Distributed / Discrete Optical Fiber. PhD thesis, Scuola Superiore Sant' Anna, 2013.

[80] L. Zhang, Y. Liu, L. Everall, J. A R Williams, and I. Bennion. Design and realization of long-period grating devices in conventional and high birefringence fibers and their novel applications as fiber-optic load sensors. IEEE Journal on Selected Topics in Quantum Electronics, 5(5):1373–1378, 1999. ISSN 1077260X. doi: 10.1109/2944.806763.

[81] Fangdong Zhu, Dongsheng Zhang, Peng Fan, Litong Li, and Yongxing Guo. Non-uniform strain measurement along a fiber Bragg grating using optical frequency domain reflectometry. Chinese Optics Letters, 11(10):1–6, 2013. doi: 10.3788/COL201311.100603.1.

[82] H Zimmermann. "Die Berechnung des Eisenbahnoberbaues" (The analysis of the railroad track. In German). Verlag W. Ernst & Sohn, 1888. (original not seen).

A

Datasheet SKF 6022 Bearing

SKF

6022-2RS1

SKF Explorer

Dimensions

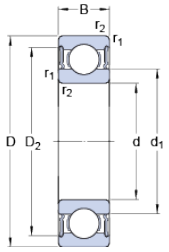

d		110	mm
D		170	mm
B		28	mm
d_1	≈	129.05	mm
D_2	≈	155.3	mm
$r_{1,2}$	min.	2	mm

Abutment dimensions

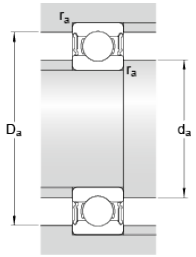

d_a	min.	119	mm
d_a	max.	128.9	mm
D_a	max.	161	mm
r_a	max.	2	mm

Calculation data

Basic dynamic load rating	C	85.2	kN
Basic static load rating	C_0	73.5	kN
Fatigue load limit	P_u	2.6	kN
Limiting speed		2400	r/min
Calculation factor	k_r	0.025	
Calculation factor	f_0	15.6	

Mass

Mass bearing	2.02	kg

Figure A.1: Datasheet SKF 6022 Bearing [71]

B

Relevant Matlab Code

Listing B.1: Import raw data files - Relevant Matlab Code

```
%% Enter start end time of measurements
T_start(1)  =  datetime(2017,8,22,13,19,28);                % Start time ...
    (yyyy,mm,dd,HH,MM,SS)
T_end(1)    =  datetime(2017,8,22,13,22,12);                % End time ...
    (yyyy,mm,dd,HH,MM,SS)
T_Test{1}   =  transpose(T_start(1):seconds(1):T_end(1));   % Time vector with a time ...
    = 1 seconds

%% Read Spectral Amplitudes
h = waitbar(0, Reading data ... );
for T = 1:length(T_Test)
    for n = 1:length(T_Test{T})                 % Number of measurements
        Result{T,n} = dlmread(fullfile ...
            ( filepath ,...
        [ Load_Test_220817_ ,datestr(T_Test{T}(n),formatout), .txt ]),  \t );
        waitbar(T / length(T_Test))
    end
end
close(h)
```

Listing B.2: Finding peak estimates - Relevant Matlab Code

```
%% Find Peak Estimate Test
% Before finding geometric centroid, a rough estimate of peak location must
% be known. (Only LOCS is relevant in this section, other variables were
% for validation)
LOCS = cell(length(T_Test),length(T_Test{1}));
p = waitbar(0, Finding Peak Estimates... );
for T=1:length(T_Test)
    for i=1:length(T_Test{T})                   % Number of measurements
        for j=1:4                               % Number of Channels
            [PKS,LOCS{T,i}(:,j)] = ...
                findpeaks(Result{T,i}(:,j), MinPeakHeight ,-20, ...
                 MinPeakDistance ,750);
        end
    end
     waitbar(T / length(T_Test))
end
close(p)
%Output: LOCS{#Test,#Measurement}(#Sensor,#Channel)
```

Listing B.3: Final peak detection - Relevant Matlab Code

```
%% Geometrical Centre (Centroid) - Peak Detection
% Relevant output for this section is PKGC, peak wavelengths of 32 sensors
% over course of measurements (time)
Width = 250;                            % Width of peak (250 1 250) aprrox 2 nm
GCPKrangeAmp = cell(length(T_Test),length(T_Test{1}),4);
GCPKrangeWav = cell(length(T_Test),length(T_Test{1}),4);
PKGC = cell(length(T_Test),4);
p = waitbar(0, 'Geometrical Centre - Peak Detection...');
for T=1:length(T_Test)                          % Number of Tests
    for i = 1:length(T_Test{T})                 % Number of measurements
        Result{T,i} = db2mag(Result{T,i}(:,:));
        for j = 1:length(LOCS{T,1}(:,1))        % Number of Sensors on Channel
            for k = 1:4                         % Number of Channels
                GCPKrangeAmp{T,i,k}(:,j) = Result{T,i}(LOCS{T,i}(j,k) ...
                    -Width:1:LOCS{T,i}(j,k)+Width,k);
                GCPKrangeWav{T,i,k}(:,j) = W(LOCS{T,i}(j,k) ...
                    -Width:1:LOCS{T,i}(j,k)+Width);
                for n = 1:length(GCPKrangeAmp{T,i,k}(:,j))
                                                % Selected Width of peak
                    if GCPKrangeAmp{T,i,k}(n,j) >= 0.05
                                % 0.05 Selected reflective threshold
                        GCPKrangeAmp{T,i,k}(n,j) = GCPKrangeAmp{T,i,k}(n,j);
                    else
                        GCPKrangeAmp{T,i,k}(n,j) =0;
                    end
                end
                PKGC{T,k}(i,j) = sum(GCPKrangeWav{T,i,k}(:,j) ...
                    .*GCPKrangeAmp{T,i,k}(:,j).*W_d)/sum(GCPKrangeAmp ...
                    {T,i,k}(:,j).*W_d);     % Centroid calculation
            end
        end
    end
    waitbar(T / length(T_Test))
end
close(p)
%Output: PKGC{#Test,#Channel}(#Measurement,#Sensor)

%% Create Peak Index matrix
Tindex = cell(length(T_Test),4);
for T=1:length(T_Test)                          % Number of Tests
    for i = 1:length(T_Test{T})                 % Number of measurements
        for j = 1:length(LOCS{T,1}(:,1))        % Number of Sensors on Channel
            for k = 1:4                         % Number of Channels
                [N,bin] = histc(PKGC{T,k}(i,j),W);
                index=bin+1;
                if abs(PKGC{T,k}(i,j)-W(bin))<abs(PKGC{T,k}(i,j)-W(bin+1))
                    fclosest=W(bin);
                    Tindex{T,k}(i,j)=bin;
                else
                    fclosest=W(index);
                    Tindex{T,k}(i,j)=index;
                end
            end
        end
    end
end
%Ouput: Tindex{#Test,#Channel}(#Measurement,#Sensor)
```

Listing B.4: Finding FWHM - Relevant Matlab Code

```
%% Finding FWHM
GCPKrangeAmp2 = cell(length(T_Test),length(T_Test{1}),4);
GCPKrangeWav2 = cell(length(T_Test),length(T_Test{1}),4);
FWHM = cell(length(T_Test),4);
for T=1:length(T_Test)                          % Number of Tests
    for i = 1:length(T_Test{T})                 % Number of measurements
        for j = 1:length(LOCS{T,1}(:,1))        % Number of Sensors on Channel
            for k = 1:4                         % Number of Channels
                GCPKrangeAmp2{T,i,k}(:,j) = ...
                    Result{T,i}(Tindex{T,k}(i,j)-Width:1:Tindex{T,k}(i,j)+Width,k);
                GCPKrangeWav2{T,i,k}(:,j) = ...
                    W(Tindex{T,k}(i,j)-Width:1:Tindex{T,k}(i,j)+Width);
                for n = 1:length(GCPKrangeAmp2{T,i,k}(:,j))          % Selected ...
                    Width of peak
                    if GCPKrangeAmp2{T,i,k}(n,j) >= Result{T,i}(LOCS{T,i}(j,k),k)/2     ...
                        % FWHM
                        GCPKrangeAmp2{T,i,k}(n,j) = GCPKrangeAmp2{T,i,k}(n,j);
                    else
                        GCPKrangeAmp2{T,i,k}(n,j) =0;
                    end
                FWHM{T,k}(i,j) = W_d*sum(GCPKrangeAmp2{T,i,k}(:,j) > 0);
                end
            end
        end
    end
end
%Ouput: FWHM{#Test,#Channel}(#Measurement,#Sensor)
```

C

Sensor Numbering

During the course of this project, two different methods were used for numbering the sensors on the Gusto bearing. Figure C.1 shows the numbering direction for the sensors on each channel. Accompanying channels were also addressed as groups, with the numbers shown in the figure. Table C.1 gives the relation between the two uased numbering methods.

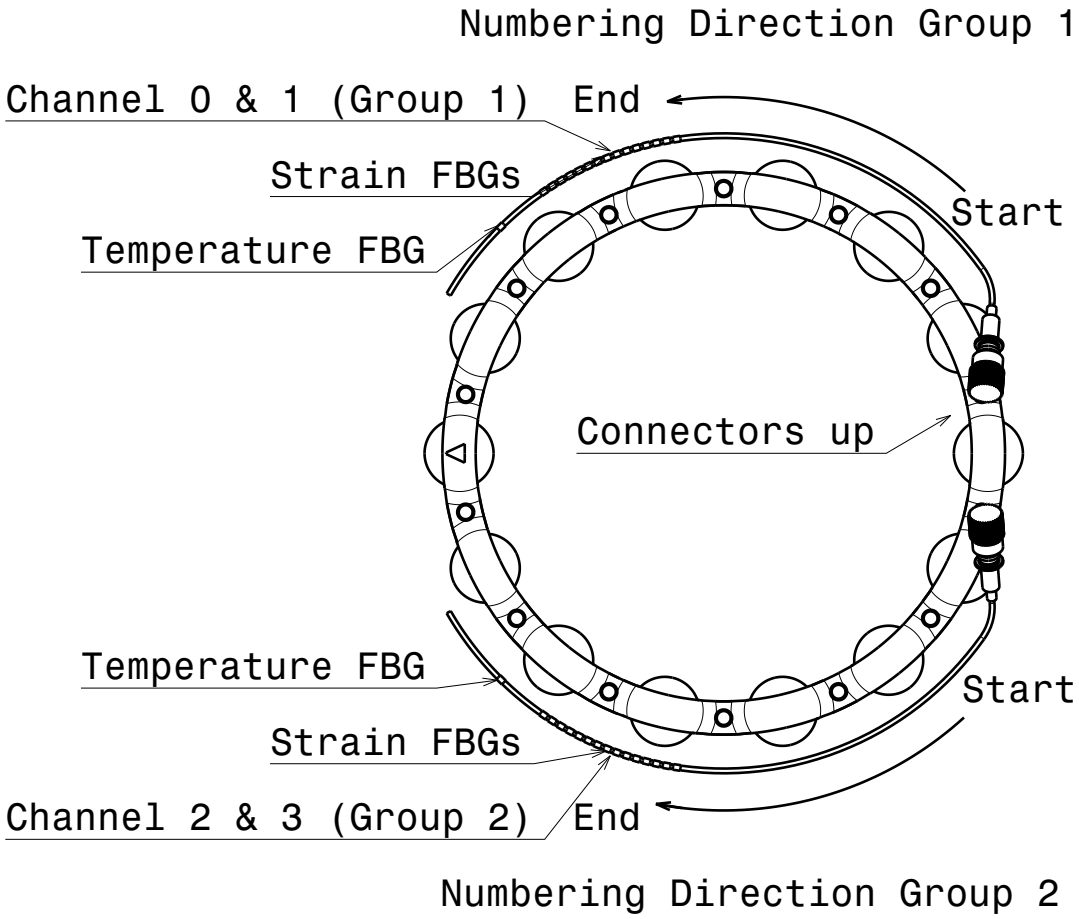

Figure C.1: Gusto bearing - FBG Channel and Group Location

Table C.1: Sensor Numbering

Channel	Sensor	Group 1	Group 2
0	1	2	-
	2	4	-
	3	6	-
	4	8	-
	5	10	-
	6	12	-
	7	14	-
	8	16	-
1	1	1	-
	2	3	-
	3	5	-
	4	7	-
	5	9	-
	6	11	-
	7	13	-
	8	15	-
2	1	-	2
	2	-	4
	3	-	6
	4	-	8
	5	-	10
	6	-	12
	7	-	14
	8	-	16
3	1	-	1
	2	-	3
	3	-	5
	4	-	7
	5	-	9
	6	-	11
	7	-	13
	8	-	15

D

Fourier Fit Data

For all fitted data the expression in Equation D.1 was used as the general model, with (n) the number of terms.

$$f(x) = a0 + a1\cos(x \cdot w) + b1\sin(x \cdot w) + a2\cos(2 \cdot x \cdot w) + b2\sin(2 \cdot x \cdot w) + \ldots + a(n)\cos((n) \cdot x \cdot w) + b(n)\sin((n) \cdot x \cdot w) \quad \text{(D.1)}$$

Fourier Fit Position 1 to 6 - Group 2 35kN (Figure 5.39)
For this fit 6 rolling element positions and 11 sensor readouts per position were used. The peak was centered around 5.44 mm.

Coefficients (with 95% confidence bounds):

a0 =	141.5	(128.8, 154.1)
a1 =	170.9	(158.9, 183)
b1 =	194.3	(172.6, 216.1)
a2 =	29.17	(6.434, 51.9)
b2 =	199.7	(186.3, 213)
a3 =	-76.63	(-91.44, -61.81)
b3 =	85.17	(61.52, 108.8)
a4 =	-59.14	(-70.65, -47.62)
b4 =	12.42	(-4.136, 28.97)
a5 =	-17.81	(-41.7, 6.078)
b5 =	-26.27	(-37.99, -14.54)
w =	0.2123	(0.1976, 0.227)

Goodness of fit:

SSE:	4.072e+04
R-square:	0.9883
Adjusted R-square:	0.9854
RMSE:	30.42

Fourier Fit Position 1 Group 2 35kN (Figure 5.41)
For this fit 1 rolling element position and 11 sensor readouts were used. The peak was centered around 5.44 mm.

Coefficients (with 95% confidence bounds):

a0 =	178.9	(137.1, 220.7)
a1 =	63.21	(-10.7, 137.1)
b1 =	366.7	(311.9, 421.6)
a2 =	-200.6	(-235.4, -165.8)
b2 =	84.44	(-11.44, 180.3)
a3 =	-52.71	(-109.7, 4.311)
b3 =	-55.59	(-85.45, -25.74)
w =	0.2896	(0.2455, 0.3336)

Goodness of fit:

SSE:	1309
R-square:	0.9985
Adjusted R-square:	0.995
RMSE:	20.89

Fourier Fit Position 2 Group 2 35kN (Figure 5.42)
For this fit 1 rolling element position and 11 sensor readouts were used. The peak was centered around 5.44 mm.

Coefficients (with 95% confidence bounds):

a0 =	180.4	(135.8, 224.9)
a1 =	43.61	(-69.09, 156.3)
b1 =	340.4	(271.6, 409.1)
a2 =	-153.9	(-204.1, -103.8)
b2 =	33.9	(-56.1, 123.9)
a3 =	-1.061	(-51.11, 48.99)
b3 =	-35.06	(-103.8, 33.71)
w =	0.3182	(0.2648, 0.3715)

Goodness of fit:

SSE:	3651
R-square:	0.9943
Adjusted R-square:	0.9809
RMSE:	34.88

Fourier Fit Position 2 Group 2 35kN SBI 17 points peak detection (Figure 5.44)
For this fit 1 rolling element position and 11 sensor readouts were used. The peak was centered around 5.44 mm.

Coefficients (with 95% confidence bounds):

a0 =	145.7	(29.48, 261.9)
a1 =	101.4	(-76.03, 278.9)
b1 =	289.5	(103.1, 476)
a2 =	-139	(-265, -12.95)
b2 =	109.1	(-133.8, 352)
a3 =	-52.27	(-202.1, 97.54)
b3 =	-22.43	(-101.2, 56.32)
w =	0.2709	(0.1181, 0.4236)

Goodness of fit:

SSE:	7292
R-square:	0.9882
Adjusted R-square:	0.9606
RMSE:	49.3

Fourier Fit Position 2 Group 2 35kN SBI 13 points peak detection (Figure 5.45)
For this fit 1 rolling element position and 11 sensor readouts were used. The peak was centered around 5.44 mm.

Coefficients (with 95% confidence bounds):

a0 =	122.9	(25.07, 220.7)
a1 =	140.7	(21.62, 259.7)
b1 =	259	(84.8, 433.2)
a2 =	-95.29	(-227.3, 36.73)
b2 =	152.3	(11.23, 293.3)
a3 =	-56.71	(-160.9, 47.47)
b3 =	23.33	(-74.65, 121.3)
w =	0.2614	(0.1385, 0.3843)

Goodness of fit:

SSE:	8746
R-square:	0.9854
Adjusted R-square:	0.9514
RMSE:	53.99

Fourier Fit Position 1 to 9 Group 2 35kN Excluding Outliers (Figure 6.4)
For this fit 9 rolling element positions and 5 sensor readouts per position were used. The peak was centered around 5.44 mm and 7 sensor readouts were excluded from the fit.

Coefficients (with 95% confidence bounds):

a0 =	310	(233.4, 386.6)
a1 =	-367	(-435.5, -298.4)
b1 =	95.52	(-169.4, 360.4)
a2 =	58.05	(23.1, 93.01)
b2 =	-22.61	(-143.6, 98.37)
w =	0.5207	(0.3923, 0.6491)

Goodness of fit:

SSE:	2.643e+04
R-square:	0.9905
Adjusted R-square:	0.989
RMSE:	28.74

E

FWHM Loaded Test

Table E.1: FWHM Group 1 - 20kN (1/2)

	Group 1	Strain FBG														
		1	2	3	4	5	6	7	8	9	10	11	12	13	14	15
Position 1	FWHM Initial [nm]	1.132	1.120	1.136	1.136	1.164	1.148	1.160	1.128	1.172	**1.184**	**1.212**	**1.212**	1.160	1.208	1.220
	FWHM 20 kN [nm]	1.132	1.120	1.136	1.132	1.164	1.144	1.160	1.124	1.180	**1.192**	**1.224**	**1.204**	1.200	1.208	1.208
	Difference	0.00%	0.00%	0.00%	-0.35%	0.00%	-0.35%	0.00%	-0.35%	0.68%	**0.68%**	**0.99%**	**-0.66%**	3.45%	0.00%	-0.98%
	Strain [$\mu\epsilon$]	61.70	6.52	-0.51	-6.29	2.32	-12.09	-22.52	-20.68	20.07	**391.65**	**520.79**	**104.27**	13.55	-7.37	-3.91
Position 2	FWHM Initial [nm]	1.132	1.116	1.136	1.136	1.164	1.152	1.160	1.128	**1.172**	**1.184**	**1.224**	1.216	1.164	1.212	1.216
	FWHM 20 kN [nm]	1.132	1.120	1.136	1.132	1.160	1.148	1.156	1.136	**1.180**	**1.196**	**1.228**	1.204	1.192	1.208	1.208
	Difference	0.00%	0.36%	0.00%	-0.35%	-0.34%	-0.35%	-0.34%	0.71%	**0.68%**	**1.01%**	**0.33%**	-0.99%	2.41%	-0.33%	-0.66%
	Strain [$\mu\epsilon$]	44.81	7.30	-1.39	-9.58	-0.97	-19.71	-24.78	19.10	**203.42**	**468.33**	**185.88**	19.36	9.20	-3.65	-2.73
Position 3	FWHM Initial [nm]	1.132	1.116	1.136	1.136	1.164	1.148	**1.172**	**1.116**	**1.168**	1.180	1.228	1.216	1.160	1.208	1.212
	FWHM 20 kN [nm]	1.136	1.116	1.132	1.128	1.168	1.148	**1.168**	**1.136**	**1.192**	1.172	1.224	1.208	1.160	1.208	1.208
	Difference	0.35%	0.00%	-0.35%	-0.70%	0.34%	0.00%	**-0.34%**	**1.79%**	**2.05%**	-0.68%	-0.33%	-0.66%	0.00%	0.00%	-0.33%
	Strain [$\mu\epsilon$]	31.04	4.99	-4.84	-17.84	-14.34	-19.44	**130.40**	**472.13**	**376.05**	12.84	-6.47	19.04	18.89	-0.80	-0.69
Position 4	FWHM Initial [nm]	1.132	1.116	1.132	1.140	1.160	**1.152**	**1.172**	**1.120**	**1.180**	1.184	1.228	1.216	1.164	1.208	1.216
	FWHM 20 kN [nm]	1.136	1.120	1.136	1.132	1.168	**1.156**	**1.176**	**1.128**	**1.168**	1.188	1.224	1.212	1.164	1.208	1.208
	Difference	0.35%	0.36%	0.35%	-0.70%	0.69%	**0.35%**	**0.34%**	**0.71%**	**-1.02%**	0.34%	-0.33%	-0.33%	0.00%	0.00%	-0.66%
	Strain [$\mu\epsilon$]	26.59	3.82	-10.27	-25.32	-17.63	**88.22**	**382.08**	**353.73**	**109.09**	-16.66	-1.49	24.46	21.33	0.50	1.07
Position 5	FWHM Initial [nm]	1.132	1.120	1.132	1.136	**1.164**	**1.148**	**1.156**	**1.116**	1.180	1.188	1.228	1.216	1.160	1.208	1.212
	FWHM 20 kN [nm]	1.136	1.120	1.140	1.128	**1.152**	**1.160**	**1.164**	**1.112**	1.180	1.188	1.232	1.212	1.164	1.212	1.208
	Difference	0.35%	0.00%	0.71%	-0.70%	**-1.03%**	**1.05%**	**0.69%**	**-0.36%**	0.00%	0.00%	0.33%	-0.33%	0.34%	0.33%	-0.33%
	Strain [$\mu\epsilon$]	23.08	-2.82	-17.05	-30.27	**32.11**	**429.57**	**346.18**	**36.39**	-2.84	-9.55	9.10	27.31	23.97	2.19	3.55
Position 6	FWHM Initial [nm]	1.132	1.120	1.136	**1.144**	**1.148**	**1.148**	1.156	1.124	1.176	1.184	1.228	1.216	1.160	1.208	1.208
	FWHM 20 kN [nm]	1.132	1.112	1.136	**1.140**	**1.164**	**1.160**	1.160	1.140	1.172	1.192	1.232	1.208	1.164	1.212	1.208
	Difference	0.00%	-0.71%	0.00%	**-0.35%**	**1.39%**	**1.05%**	0.35%	1.42%	-0.34%	0.68%	0.33%	-0.66%	0.34%	0.33%	0.00%
	Strain [$\mu\epsilon$]	14.99	-15.95	-9.62	**185.16**	**455.65**	**184.31**	-5.68	-25.30	-8.77	2.47	15.29	30.31	27.28	5.16	4.48
Position 7	FWHM Initial [nm]	1.136	1.116	**1.136**	**1.132**	**1.172**	1.148	1.164	1.124	1.176	1.184	1.224	1.216	1.160	1.208	1.212
	FWHM 20 kN [nm]	1.132	1.112	**1.156**	**1.128**	**1.164**	1.148	1.160	1.132	1.168	1.192	1.232	1.212	1.164	1.212	1.204
	Difference	-0.35%	-0.36%	**1.76%**	**-0.35%**	**-0.68%**	0.00%	-0.34%	0.71%	-0.68%	0.68%	0.65%	-0.33%	0.34%	0.33%	-0.66%
	Strain [$\mu\epsilon$]	4.99	-4.75	**203.44**	**476.94**	**235.16**	-27.98	-31.48	-14.25	-0.01	6.94	18.83	33.16	29.29	5.44	15.52
Position 8	FWHM Initial [nm]	1.132	**1.116**	**1.144**	**1.124**	1.164	1.148	1.164	1.128	1.176	1.184	1.224	1.216	1.160	1.212	1.208
	FWHM 20 kN [nm]	1.124	**1.124**	**1.152**	**1.132**	1.156	1.160	1.168	1.132	1.164	1.184	1.228	1.212	1.180	1.208	1.212
	Difference	-0.71%	**0.72%**	**0.70%**	**0.71%**	-0.69%	1.05%	0.34%	0.35%	-1.02%	0.00%	0.33%	-0.33%	1.72%	-0.33%	0.33%
	Strain [$\mu\epsilon$]	0.71	**178.98**	**466.60**	**142.53**	20.06	-24.67	-24.73	-6.54	4.44	9.14	20.92	33.45	29.27	9.65	88.05

Table E.2: FWHM Group 1 - 20kN (2/2)

	Group 1	Strain FBG														
		1	2	3	4	5	6	7	8	9	10	11	12	13	14	15
Position 9	FWHM Initial [nm]	1.128	**1.116**	**1.136**	**1.132**	1.160	1.148	1.160	1.128	1.176	1.188	1.228	1.216	1.164	1.208	**1.208**
	FWHM 20 kN [nm]	1.132	**1.136**	**1.156**	**1.128**	1.160	1.148	1.172	1.128	1.168	1.184	1.224	1.212	1.180	1.208	**1.196**
	Difference	0.35%	**1.79%**	**1.76%**	**-0.35%**	0.00%	0.00%	1.03%	0.00%	-0.68%	-0.34%	-0.33%	-0.33%	1.37%	0.00%	**-0.99%**
	Strain [$\mu\epsilon$]	18.78	**380.68**	**393.11**	**33.80**	-4.75	-19.90	-20.02	-4.65	4.95	9.77	18.87	32.10	23.70	24.37	**180.85**
Position 10	FWHM Initial [nm]	**1.132**	**1.120**	**1.136**	1.132	1.164	1.148	1.164	1.128	1.176	1.188	1.228	1.216	1.164	**1.212**	**1.208**
	FWHM 20 kN [nm]	**1.132**	**1.112**	**1.160**	1.136	1.168	1.148	1.160	1.128	1.168	1.184	1.228	1.212	1.164	**1.208**	**1.212**
	Difference	**0.00%**	**-0.71%**	**2.11%**	0.35%	0.34%	0.00%	-0.34%	0.00%	-0.68%	-0.34%	0.00%	-0.33%	0.00%	**-0.33%**	**0.33%**
	Strain [$\mu\epsilon$]	**103.25**	**504.76**	**150.74**	-15.36	-7.93	-13.90	-14.74	-2.52	6.38	10.32	21.09	27.45	20.95	**87.88**	**368.02**
Position 11	FWHM Initial [nm]	**1.128**	**1.120**	1.136	1.136	1.164	1.144	1.164	1.124	1.176	1.188	1.228	1.216	**1.168**	**1.212**	**1.208**
	FWHM 20 kN [nm]	**1.132**	**1.116**	1.132	1.132	1.164	1.148	1.160	1.124	1.168	1.184	1.232	1.212	**1.168**	**1.224**	**1.216**
	Difference	**0.35%**	**-0.36%**	-0.35%	-0.35%	0.00%	0.35%	-0.34%	0.00%	-0.68%	-0.34%	0.33%	-0.33%	**0.00%**	**0.99%**	**0.66%**
	Strain [$\mu\epsilon$]	**305.00**	**110.04**	-10.54	-14.74	1.08	-6.43	-11.45	0.15	7.74	8.47	16.60	22.47	**48.98**	**425.19**	**311.48**

Table E.3: FWHM Group 2 - 20kN (1/2)

Group 2		Strain FBG														
		1	2	3	4	5	6	7	8	9	10	11	12	13	14	15
Position 1	FWHM Initial [nm]	1.124	1.104	1.160	1.144	1.168	**1.124**	**1.148**	**1.132**	1.168	1.180	1.180	1.184	1.176	1.200	1.224
	FWHM 20 kN [nm]	1.128	1.100	1.160	1.148	1.164	**1.136**	**1.156**	**1.144**	1.168	1.172	1.180	1.184	1.172	1.200	1.224
	Difference	0.36%	-0.36%	0.00%	0.35%	-0.34%	**1.07%**	**0.70%**	**1.06%**	0.00%	-0.68%	0.00%	0.00%	-0.34%	0.00%	0.00%
	Strain [$\mu\epsilon$]	-55.66	-19.32	-53.01	-25.26	-52.33	**226.96**	**526.74**	**228.18**	-35.20	-46.72	-46.89	-34.14	-33.17	-77.63	-34.79
Position 2	FWHM Initial [nm]	1.124	1.100	1.160	1.140	1.168	1.124	**1.156**	**1.140**	**1.172**	1.180	1.180	1.184	1.176	1.200	1.224
	FWHM 20 kN [nm]	1.128	1.100	1.160	1.144	1.172	1.132	**1.156**	**1.148**	**1.160**	1.184	1.180	1.188	1.180	1.196	1.220
	Difference	0.36%	0.00%	0.00%	0.35%	0.34%	0.71%	**0.00%**	**0.70%**	**-1.02%**	0.34%	0.00%	0.34%	0.34%	-0.33%	-0.33%
	Strain [$\mu\epsilon$]	-53.45	-13.99	-49.83	-21.40	-53.88	29.95	**259.83**	**433.60**	**119.40**	-35.17	-45.35	-33.44	-32.49	-76.63	-32.70
Position 3	FWHM Initial [nm]	1.124	1.104	1.160	1.144	1.164	1.128	**1.152**	**1.136**	**1.168**	1.180	1.180	1.184	1.180	1.200	1.224
	FWHM 20 kN [nm]	1.128	1.104	1.160	1.140	1.168	1.120	**1.160**	**1.144**	**1.176**	1.176	1.184	1.176	1.168	1.200	1.224
	Difference	0.36%	0.00%	0.00%	-0.35%	0.34%	-0.71%	**0.69%**	**0.70%**	**0.68%**	-0.34%	0.34%	-0.68%	-1.02%	0.00%	0.00%
	Strain [$\mu\epsilon$]	-52.17	-11.52	-48.61	-18.96	-51.74	-14.82	**92.51**	**395.16**	**279.23**	-9.53	-44.70	-32.74	-29.82	-75.11	-32.84
Position 4	FWHM Initial [nm]	1.128	1.104	1.160	1.136	1.164	1.124	1.152	**1.132**	**1.164**	**1.180**	1.180	1.184	1.180	1.200	1.220
	FWHM 20 kN [nm]	1.128	1.100	1.160	1.140	1.160	1.120	1.152	**1.136**	**1.160**	**1.188**	1.168	1.188	1.168	1.200	1.224
	Difference	0.00%	-0.36%	0.00%	0.35%	-0.34%	-0.36%	0.00%	**0.35%**	**-0.34%**	**0.68%**	-1.02%	0.34%	-1.02%	0.00%	0.33%
	Strain [$\mu\epsilon$]	-54.39	-10.04	-48.74	-17.15	-49.35	-33.46	-10.15	**254.01**	**443.14**	**41.62**	-42.72	-33.65	-34.42	-74.84	-33.60
Position 5	FWHM Initial [nm]	1.128	1.100	1.160	1.140	1.164	1.128	1.152	**1.132**	**1.168**	**1.180**	1.180	1.180	1.176	1.204	1.220
	FWHM 20 kN [nm]	1.128	1.104	1.160	1.140	1.160	1.120	1.140	**1.152**	**1.160**	**1.188**	1.184	1.196	1.172	1.200	1.224
	Difference	0.00%	0.36%	0.00%	0.00%	-0.34%	-0.71%	-1.04%	**1.77%**	**-0.68%**	**0.68%**	0.34%	1.36%	-0.34%	-0.33%	0.33%
	Strain [$\mu\epsilon$]	-52.04	-6.12	-48.61	-15.48	-46.00	-37.78	-47.24	**92.21**	**438.41**	**149.43**	-10.23	-28.29	-33.88	-74.44	-32.47
Position 6	FWHM Initial [nm]	1.124	1.100	1.160	1.140	1.168	1.128	1.156	1.128	**1.164**	**1.180**	**1.176**	1.184	1.176	1.204	1.220
	FWHM 20 kN [nm]	1.128	1.100	1.160	1.144	1.160	1.124	1.156	1.140	**1.156**	**1.188**	**1.184**	1.200	1.184	1.204	1.224
	Difference	0.36%	0.00%	0.00%	0.35%	-0.68%	-0.35%	0.00%	1.06%	**-0.69%**	**0.68%**	**0.68%**	1.35%	0.68%	0.00%	0.33%
	Strain [$\mu\epsilon$]	-47.90	0.74	-48.29	-13.74	-44.04	-33.79	-52.93	-11.37	**205.46**	**302.57**	**116.13**	-10.58	-34.71	-74.08	-30.20
Position 7	FWHM Initial [nm]	1.128	1.096	1.156	1.140	1.164	1.124	1.156	1.128	1.160	**1.184**	**1.176**	**1.184**	1.176	1.200	1.220
	FWHM 20 kN [nm]	1.128	1.096	1.160	1.144	1.164	1.124	1.160	1.136	1.160	**1.180**	**1.188**	**1.208**	1.168	1.200	1.220
	Difference	0.00%	0.00%	0.35%	0.35%	0.00%	0.00%	0.35%	0.71%	0.00%	**-0.34%**	**1.02%**	**2.03%**	-0.68%	0.00%	0.00%
	Strain [$\mu\epsilon$]	-40.14	14.68	-49.02	-12.38	-41.02	-27.14	-44.58	-47.29	-25.31	**292.30**	**469.36**	**113.83**	-29.48	-73.27	-29.23
Position 8	FWHM Initial [nm]	1.128	1.096	1.160	1.140	1.160	1.124	1.156	1.128	1.160	1.176	**1.188**	**1.204**	**1.176**	1.200	1.224
	FWHM 20 kN [nm]	1.132	1.096	1.160	1.144	1.168	1.124	1.156	1.144	1.168	1.176	**1.180**	**1.184**	**1.176**	1.200	1.204
	Difference	0.35%	0.00%	0.00%	0.35%	0.69%	0.00%	0.00%	1.42%	0.69%	0.00%	**-0.67%**	**-1.66%**	**0.00%**	0.00%	-1.63%
	Strain [$\mu\epsilon$]	-28.86	28.24	-53.19	-14.11	-41.62	-26.91	-40.09	-40.33	-41.87	30.24	**96.63**	**426.15**	**257.58**	-23.48	-33.16

Table E.4: FWHM Group 2 - 20kN (2/2)

	Group 2	Strain FBG														
		1	2	3	4	5	6	7	8	9	10	11	12	13	14	15
Position 9	FWHM Initial [nm]	1.128	1.092	1.156	1.136	1.164	1.124	1.156	1.128	1.160	1.184	1.184	**1.184**	**1.172**	**1.200**	1.224
	FWHM 20 kN [nm]	1.128	1.112	1.152	1.140	1.160	1.124	1.152	1.140	1.160	1.184	1.180	**1.196**	**1.196**	**1.204**	1.224
	Difference	0.00%	1.83%	-0.35%	0.35%	-0.34%	0.00%	-0.35%	1.06%	0.00%	0.00%	-0.34%	**1.01%**	**2.05%**	**0.33%**	0.00%
	Strain [$\mu\epsilon$]	52.40	72.47	-60.26	-17.97	-43.60	-28.65	-41.47	-39.07	-39.96	-20.58	-25.24	**77.76**	**404.33**	**274.02**	13.85
Position 10	FWHM Initial [nm]	**1.132**	**1.096**	1.156	1.136	1.160	1.124	1.156	1.128	1.160	1.184	1.176	1.188	1.176	**1.200**	**1.224**
	FWHM 20 kN [nm]	**1.128**	**1.112**	1.160	1.136	1.180	1.120	1.148	1.144	1.164	1.176	1.184	1.188	1.180	**1.196**	**1.208**
	Difference	**-0.35%**	**1.46%**	0.35%	0.00%	1.72%	-0.36%	-0.69%	1.42%	0.34%	-0.68%	0.68%	0.00%	0.34%	**-0.33%**	**-1.31%**
	Strain [$\mu\epsilon$]	**309.47**	**340.10**	60.78	-26.95	-58.78	-38.26	-47.24	-43.66	-43.09	-27.01	-28.79	-19.53	-21.24	**36.57**	**422.51**

Table E.5: FWHM Group 1 - 35kN (1/2)

	Group 1	Strain FBG														
		1	2	3	4	5	6	7	8	9	10	11	12	13	14	15
Position 1	FWHM Initial [nm]	1.132	1.120	1.136	1.136	1.164	1.148	1.160	1.128	1.172	**1.184**	**1.212**	**1.212**	1.160	1.208	1.220
	FWHM 35 kN [nm]	1.124	1.120	1.136	1.132	1.164	1.144	1.160	1.124	1.168	**1.192**	**1.216**	**1.216**	1.172	1.204	1.212
	Difference	-0.71%	0.00%	0.00%	-0.35%	0.00%	-0.35%	0.00%	-0.35%	-0.34%	**0.68%**	**0.33%**	**0.33%**	1.03%	-0.33%	-0.66%
	Max Strain [$\mu\epsilon$]	92.69	4.31	-3.55	-12.38	-3.81	-17.90	-29.85	-23.26	42.61	**638.59**	**831.44**	**172.60**	28.99	15.78	24.74
Position 2	FWHM Initial [nm]	1.132	1.116	1.136	1.136	1.164	1.152	1.160	1.128	**1.172**	**1.184**	**1.224**	1.216	1.164	1.212	1.216
	FWHM 35 kN [nm]	1.132	1.120	1.140	1.128	1.164	1.148	1.168	1.136	**1.176**	**1.200**	**1.236**	1.180	1.212	1.212	1.204
	Difference	0.00%	0.36%	0.35%	-0.70%	0.00%	-0.35%	0.69%	0.71%	**0.34%**	**1.35%**	**0.98%**	-2.96%	4.12%	0.00%	-0.99%
	Max Strain [$\mu\epsilon$]	61.94	3.89	-6.89	-18.36	-11.78	-32.16	-33.07	39.44	**333.70**	**740.69**	**302.27**	29.16	21.57	20.98	29.19
Position 3	FWHM Initial [nm]	1.132	1.116	1.136	1.136	1.164	1.148	**1.172**	**1.116**	**1.168**	1.180	1.228	1.216	1.160	1.208	1.212
	FWHM 35 kN [nm]	1.136	1.116	1.136	1.128	1.168	1.148	**1.164**	**1.140**	**1.200**	1.184	1.240	1.208	1.160	1.212	1.208
	Difference	0.35%	0.00%	0.00%	-0.70%	0.34%	0.00%	**-0.68%**	**2.15%**	**2.74%**	0.34%	0.98%	-0.66%	0.00%	0.33%	-0.33%
	Max Strain [$\mu\epsilon$]	36.41	0.06	-14.39	-33.81	-32.83	-31.28	**216.92**	**756.48**	**600.91**	28.74	-4.96	28.56	34.27	25.71	31.02
Position 4	FWHM Initial [nm]	1.132	1.116	1.132	1.140	1.160	**1.152**	**1.172**	**1.120**	**1.180**	1.184	1.228	1.216	1.164	1.208	1.216
	FWHM 35 kN [nm]	1.136	1.116	1.140	1.128	1.168	**1.172**	**1.180**	**1.144**	**1.168**	1.172	1.220	1.204	1.168	1.212	1.208
	Difference	0.35%	0.00%	0.71%	-1.05%	0.69%	**1.74%**	**0.68%**	**2.14%**	**-1.02%**	-1.01%	-0.65%	-0.99%	0.34%	0.33%	-0.66%
	Max Strain [$\mu\epsilon$]	31.38	-3.84	-21.91	-48.04	-37.72	**147.22**	**604.61**	**566.31**	**182.25**	-22.99	-2.88	38.03	40.18	28.43	33.69
Position 5	FWHM Initial [nm]	1.132	1.120	1.132	1.136	**1.164**	**1.148**	**1.156**	**1.116**	1.180	1.188	1.228	1.216	1.160	1.208	1.212
	FWHM 35 kN [nm]	1.132	1.120	1.136	1.124	**1.176**	**1.188**	**1.152**	**1.140**	1.164	1.188	1.232	1.204	1.164	1.212	1.208
	Difference	0.00%	0.00%	0.35%	-1.06%	**1.03%**	**3.48%**	**-0.35%**	**2.15%**	-1.36%	0.00%	0.33%	-0.99%	0.34%	0.33%	-0.33%
	Max Strain [$\mu\epsilon$]	25.66	-12.89	-36.09	-52.62	**54.06**	**681.69**	**554.99**	**66.69**	-7.75	-14.00	9.94	44.25	43.98	31.67	37.24
Position 6	FWHM Initial [nm]	1.132	1.120	1.136	**1.144**	**1.148**	**1.148**	1.156	1.124	1.176	1.184	1.228	1.216	1.160	1.208	1.208
	FWHM 35 kN [nm]	1.132	1.116	1.140	**1.160**	**1.172**	**1.164**	1.168	1.140	1.168	1.184	1.232	1.212	1.164	1.208	1.208
	Difference	0.00%	-0.36%	0.35%	**1.40%**	**2.09%**	**1.39%**	1.04%	1.42%	-0.68%	0.00%	0.33%	-0.33%	0.34%	0.00%	0.00%
	Max Strain [$\mu\epsilon$]	12.80	-35.68	-21.30	**299.01**	**711.97**	**289.89**	1.68	-44.91	-20.70	6.17	25.62	50.77	50.85	35.99	41.61
Position 7	FWHM Initial [nm]	1.136	1.116	**1.136**	**1.132**	**1.172**	1.148	1.164	1.124	1.176	1.184	1.224	1.216	1.160	1.208	1.212
	FWHM 35 kN [nm]	1.132	1.112	**1.152**	**1.136**	**1.156**	1.152	1.164	1.136	1.172	1.192	1.236	1.208	1.168	1.212	1.204
	Difference	-0.35%	-0.36%	**1.41%**	**0.35%**	**-1.37%**	0.35%	0.00%	1.07%	-0.34%	0.68%	0.98%	-0.66%	0.69%	0.33%	-0.66%
	Max Strain [$\mu\epsilon$]	-5.43	-15.74	**325.86**	**751.83**	**367.65**	-47.89	-51.84	-25.07	-6.31	15.77	33.04	56.35	55.78	38.11	57.74
Position 8	FWHM Initial [nm]	1.132	**1.116**	**1.144**	**1.124**	1.164	1.148	1.164	1.128	1.176	1.184	1.224	1.216	1.160	1.212	1.208
	FWHM 35 kN [nm]	1.128	**1.132**	**1.148**	**1.148**	1.156	1.160	1.164	1.132	1.172	1.192	1.224	1.212	1.184	1.208	1.208
	Difference	-0.35%	**1.43%**	**0.35%**	**2.14%**	-0.69%	1.05%	0.00%	0.35%	-0.34%	0.68%	0.00%	-0.33%	2.07%	-0.33%	0.00%
	Max Strain [$\mu\epsilon$]	-8.93	**279.39**	**730.32**	**230.66**	20.56	-47.87	-37.04	-10.94	2.12	20.97	35.44	57.78	53.38	48.36	183.99

Table E.6: FWHM Group 1 - 35kN (2/2)

	Group 1	Strain FBG														
		1	2	3	4	5	6	7	8	9	10	11	12	13	14	15
Position 9	FWHM Initial [nm]	1.128	**1.116**	**1.136**	**1.132**	1.160	1.148	1.160	1.128	1.176	1.188	1.228	1.216	1.164	1.208	**1.208**
	FWHM 35 kN [nm]	1.128	**1.152**	**1.160**	**1.120**	1.164	1.152	1.168	1.132	1.172	1.192	1.232	1.208	1.160	1.208	**1.212**
	Difference	0.00%	**3.23%**	**2.11%**	**-1.06%**	0.34%	0.35%	0.69%	0.35%	-0.34%	0.34%	0.33%	-0.66%	-0.34%	0.00%	**0.33%**
	Max Strain [$\mu\epsilon$]	15.99	**598.86**	**619.43**	**47.43**	-25.63	-40.86	-29.51	-8.87	4.86	22.43	37.56	54.18	44.85	69.14	**328.32**
Position 10	FWHM Initial [nm]	**1.132**	**1.120**	**1.136**	1.132	1.164	1.148	1.164	1.128	1.176	1.188	1.228	1.216	1.164	**1.212**	**1.208**
	FWHM 35 kN [nm]	**1.128**	**1.128**	**1.168**	1.136	1.160	1.148	1.172	1.124	1.168	1.192	1.232	1.208	1.164	**1.216**	**1.220**
	Difference	**-0.35%**	**0.71%**	**2.82%**	0.35%	-0.34%	0.00%	0.69%	-0.35%	-0.68%	0.34%	0.33%	-0.66%	0.00%	**0.33%**	**0.99%**
	Max Strain [$\mu\epsilon$]	**153.99**	**793.06**	**241.44**	-35.97	-34.31	-28.66	-22.03	-4.84	8.67	23.17	37.41	49.08	38.79	**168.68**	**601.95**
Position 11	FWHM Initial [nm]	**1.128**	**1.120**	1.136	1.136	1.164	1.144	1.164	1.124	1.176	1.188	1.228	1.216	**1.168**	**1.212**	**1.208**
	FWHM 35 kN [nm]	**1.132**	**1.120**	1.136	1.124	1.160	1.148	1.168	1.124	1.168	1.184	1.228	1.212	**1.160**	**1.220**	**1.224**
	Difference	**0.35%**	**0.00%**	0.00%	-1.06%	-0.34%	0.35%	0.34%	0.00%	-0.68%	-0.34%	0.00%	-0.33%	**-0.68%**	**0.66%**	**1.32%**
	Max Strain [$\mu\epsilon$]	**458.47**	**176.29**	-28.24	-35.99	-14.52	-15.62	-14.46	0.18	10.29	20.01	30.62	46.78	**91.69**	**695.35**	**513.15**

Table E.7: FWHM Group 2 - 35kN (1/2)

	Group 2	Strain FBG														
		1	2	3	4	5	6	7	8	9	10	11	12	13	14	15
Position 1	FWHM Initial [nm]	1.124	1.104	1.160	1.144	1.168	**1.124**	**1.148**	**1.132**	1.168	1.180	1.180	1.184	1.176	1.200	1.224
	FWHM 35 kN [nm]	1.128	1.096	1.160	1.140	1.160	**1.128**	**1.176**	**1.140**	1.164	1.172	1.180	1.192	1.168	1.200	1.224
	Difference	0.36%	-0.72%	0.00%	-0.35%	-0.68%	**0.36%**	**2.44%**	**0.71%**	-0.34%	-0.68%	0.00%	0.68%	-0.68%	0.00%	0.00%
	Max Strain [$\mu\epsilon$]	-62.45	-26.81	-68.45	-46.88	-62.74	**374.44**	**845.79**	**395.11**	-13.20	-37.46	-32.22	-12.96	-6.33	-47.33	-5.39
Position 2	FWHM Initial [nm]	1.124	1.100	1.160	1.140	1.168	1.124	**1.156**	**1.140**	**1.172**	1.180	1.180	1.184	1.176	1.200	1.224
	FWHM 35 kN [nm]	1.124	1.100	1.156	1.144	1.168	1.128	**1.192**	**1.152**	**1.156**	1.184	1.176	1.184	1.176	1.204	1.220
	Difference	0.00%	0.00%	-0.34%	0.35%	0.00%	0.36%	**3.11%**	**1.05%**	**-1.37%**	0.34%	-0.34%	0.00%	0.00%	0.33%	-0.33%
	Max Strain [$\mu\epsilon$]	-60.57	-22.87	-61.77	-37.15	-74.69	58.89	**442.89**	**708.27**	**229.75**	-14.51	-33.15	-12.83	-7.55	-46.91	-4.56
Position 3	FWHM Initial [nm]	1.124	1.104	1.160	1.144	1.164	1.128	**1.152**	**1.136**	**1.168**	1.180	1.180	1.184	1.180	1.200	1.224
	FWHM 35 kN [nm]	1.128	1.100	1.164	1.144	1.172	1.128	**1.176**	**1.132**	**1.164**	1.172	1.184	1.176	1.180	1.200	1.228
	Difference	0.36%	-0.36%	0.34%	0.00%	0.69%	0.00%	**2.08%**	**-0.35%**	**-0.34%**	-0.68%	0.34%	-0.68%	0.00%	0.00%	0.33%
	Max Strain [$\mu\epsilon$]	-59.04	-19.70	-58.82	-32.48	-68.48	-8.64	**178.73**	**663.12**	**487.25**	23.08	-33.72	-13.16	-5.74	-45.64	-3.86
Position 4	FWHM Initial [nm]	1.128	1.104	1.160	1.136	1.164	1.124	1.152	**1.132**	**1.164**	**1.180**	1.180	1.184	1.180	1.200	1.220
	FWHM 35 kN [nm]	1.124	1.100	1.156	1.140	1.164	1.124	1.164	**1.152**	**1.168**	**1.192**	1.172	1.200	1.172	1.204	1.224
	Difference	-0.35%	-0.36%	-0.34%	0.35%	0.00%	0.00%	1.04%	**1.77%**	**0.34%**	**1.02%**	-0.68%	1.35%	-0.68%	0.33%	0.33%
	Max Strain [$\mu\epsilon$]	-61.06	-16.66	-59.88	-29.96	-63.10	-42.57	15.11	**434.76**	**736.96**	**108.31**	-26.92	-16.30	-9.92	-46.30	-4.98
Position 5	FWHM Initial [nm]	1.128	1.100	1.160	1.140	1.164	1.128	1.152	**1.132**	**1.168**	**1.180**	1.180	1.180	1.176	1.204	1.220
	FWHM 35 kN [nm]	1.124	1.100	1.160	1.140	1.164	1.120	1.144	**1.156**	**1.164**	**1.188**	1.184	1.188	1.164	1.200	1.220
	Difference	-0.35%	0.00%	0.00%	0.00%	0.00%	-0.71%	-0.69%	**2.12%**	**-0.34%**	**0.68%**	0.34%	0.68%	-1.02%	-0.33%	0.00%
	Max Strain [$\mu\epsilon$]	-58.18	-9.90	-58.54	-26.19	-57.22	-47.49	-49.28	**183.77**	**730.86**	**272.28**	26.53	-8.25	-13.28	-46.80	-4.76
Position 6	FWHM Initial [nm]	1.124	1.100	1.160	1.140	1.168	1.128	1.156	1.128	**1.164**	**1.180**	**1.176**	1.184	1.176	1.204	1.220
	FWHM 35 kN [nm]	1.128	1.100	1.164	1.140	1.164	1.124	1.160	1.136	**1.168**	**1.196**	**1.192**	1.200	1.188	1.204	1.224
	Difference	0.36%	0.00%	0.34%	0.00%	-0.34%	-0.35%	0.35%	0.71%	**0.34%**	**1.36%**	**1.36%**	1.35%	1.02%	0.00%	0.33%
	Max Strain [$\mu\epsilon$]	-52.34	-1.44	-57.99	-22.20	-51.86	-41.58	-59.57	18.23	**371.09**	**521.24**	**231.07**	18.44	-13.49	-46.10	-2.53
Position 7	FWHM Initial [nm]	1.128	1.096	1.156	1.140	1.164	1.124	1.156	1.128	1.160	**1.184**	**1.176**	**1.184**	1.176	1.200	1.220
	FWHM 35 kN [nm]	1.128	1.096	1.164	1.140	1.164	1.124	1.152	1.152	1.160	**1.180**	**1.188**	**1.216**	1.172	1.200	1.220
	Difference	0.00%	0.00%	0.69%	0.00%	0.00%	0.00%	-0.35%	2.13%	0.00%	**-0.34%**	**1.02%**	**2.70%**	-0.34%	0.00%	0.00%
	Max Strain [$\mu\epsilon$]	-42.05	18.57	-58.91	-20.78	-46.50	-30.07	-46.03	-39.92	-7.12	**496.44**	**776.68**	**217.10**	-3.10	-47.05	-3.00
Position 8	FWHM Initial [nm]	1.128	1.096	1.160	1.140	1.160	1.124	1.156	1.128	1.160	1.176	**1.188**	**1.204**	**1.176**	1.200	1.224
	FWHM 35 kN [nm]	1.132	1.108	1.164	1.144	1.160	1.124	1.148	1.152	1.172	1.176	**1.188**	**1.188**	**1.192**	1.204	1.212
	Difference	0.35%	1.09%	0.34%	0.35%	0.00%	0.00%	-0.69%	2.13%	1.03%	0.00%	**0.00%**	**-1.33%**	**1.36%**	0.33%	-0.98%
	Max Strain [$\mu\epsilon$]	-26.58	37.65	-67.07	-24.12	-49.24	-29.19	-38.30	-32.24	-32.13	85.37	**198.32**	**708.91**	**453.66**	36.22	-6.29

Table E.8: FWHM Group 2 - 35kN (2/2)

	Group 2	Strain FBG														
		1	2	3	4	5	6	7	8	9	10	11	12	13	14	15
Position 9	FWHM Initial [nm]	1.128	1.092	1.156	1.136	1.164	1.124	1.156	1.128	1.160	1.184	1.184	**1.184**	**1.172**	**1.200**	1.224
	FWHM 35 kN [nm]	1.124	1.100	1.160	1.140	1.156	1.124	1.148	1.152	1.160	1.184	1.184	**1.188**	**1.180**	**1.212**	1.204
	Difference	-0.35%	0.73%	0.35%	0.35%	-0.69%	0.00%	-0.69%	2.13%	0.00%	0.00%	0.00%	**0.34%**	**0.68%**	**1.00%**	-1.63%
	Max Strain [$\mu\epsilon$]	98.04	104.54	-84.38	-32.53	-53.79	-31.50	-38.86	-28.83	-26.13	2.32	-0.18	**169.57**	**676.95**	**507.52**	66.95
Position 10	FWHM Initial [nm]	**1.132**	**1.096**	1.156	1.136	1.160	1.124	1.156	1.128	1.160	1.184	1.176	1.188	1.176	**1.200**	**1.224**
	FWHM 35 kN [nm]	**1.132**	**1.108**	1.156	1.136	1.172	1.120	1.144	1.148	1.156	1.176	1.184	1.192	1.168	**1.200**	**1.216**
	Difference	**0.00%**	**1.09%**	0.00%	0.00%	1.03%	-0.36%	-1.04%	1.77%	-0.34%	-0.68%	0.68%	0.34%	-0.68%	**0.00%**	**-0.65%**
	Max Strain [$\mu\epsilon$]	**519.43**	**547.53**	122.31	-50.34	-81.37	-48.60	-47.81	-35.94	-29.80	-2.46	0.48	6.90	8.87	**140.01**	**734.35**